Enhancing the Harrow-Hassidim-Lloyd (HHL) algorithm in systems with large condition numbers

Peniel Bertrand Tsemo,[1,2] Akshaya Jayashankar,[1] K. Sugisaki,[1,3,4,5] Nishanth Baskaran,[6] Sayan Chakraborty,[7,8] and V. S. Prasannaa[1,8,*]

[1]*Centre for Quantum Engineering, Research and Education, TCG CREST, Sector V, Salt Lake, Kolkata 700091, India*
[2]*Department of Physics, IIT Tirupati, Chindepalle, Andhra Pradesh 517619, India*
[3]*Graduate School of Science and Technology, Keio University, 7-1 Shinkawasaki, Saiwai-ku, Kawasaki, Kanagawa 212-0032, Japan*
[4]*Quantum Computing Center, Keio University, 3-14-1 Hiyoshi, Kohoku-ku, Yokohama, Kanagawa 223-8522, Japan*
[5]*Keio University Sustainable Quantum Artificial Intelligence Center (KSQAIC), Keio University, 2-15-45 Mita, Minato-ku, Tokyo 108-8345, Japan*
[6]*Department of Electrical and Computer Engineering, The University of British Columbia, Vancouver, British Columbia V6T 1Z4, Canada*
[7]*Institute for Advancing Intelligence, TCG CREST, Sector V, Salt Lake, Kolkata 700091, India*
[8]*Academy of Scientific and Innovative Research (AcSIR), Ghaziabad 201002, India*

(Received 9 October 2024; accepted 29 May 2025; published 17 June 2025)

Although the Harrow-Hassidim-Lloyd (HHL) algorithm offers an exponential speedup in system size for treating linear equations of the form $A\vec{x} = \vec{b}$ on quantum computers when compared to their traditional counterparts, it faces a challenge related to the condition number (κ) scaling of the A matrix. In this work, we address the issue by introducing the postselection-improved HHL (Psi-HHL) framework that operates on a simple yet effective premise: subtracting mixed and wrong signals to extract correct signals while providing the benefit of optimal scaling in the condition number of A (denoted as κ) for large κ scenarios. This approach, which leads to minimal increase in circuit depth, has the important practical implication of having to use substantially fewer shots relative to the traditional HHL algorithm. The term "signal" refers to a feature of $|x\rangle$. We design circuits for overlap and expectation value estimation in the Psi-HHL framework. We demonstrate performance of Psi-HHL via numerical simulations. We carry out two sets of computations, where we go up to 26-qubit calculations, to demonstrate the ability of Psi-HHL to handle situations involving large-κ matrices via (a) a set of toy matrices, for which we go up to size 64×64 and κ values of up to $\approx 1 \times 10^6$, and (b) application to quantum chemistry, where we consider matrices up to size 256×256 that reach κ of about 393. The molecular systems that we consider are Li_2, KH, RbH, and CsH.

DOI: 10.1103/msvx-1drx

I. INTRODUCTION

The Harrow-Hassidim-Lloyd (HHL) algorithm was proposed to solve equations of the form $A\vec{x} = \vec{b}$, where A is a known and sparse $2^N \times 2^N$ matrix and $\vec{b}$ is a $2^N \times 1$ vector, on quantum computers with a time complexity that is exponentially lower in system size than those of the best-known classical methods [1]. Further, via amplitude encoding $\vec{b}$, which is a $2^N \times 1$ vector, is encoded into a $\log_2 2^N$-qubit state (for brevity, we shall hereafter denote 2^N as n). Thus, when the HHL approach is applied to "killer applications" of quantum computing such as quantum chemistry, there is an exponential suppression in qubit number relative to the other known approaches such as the quantum phase estimation (QPE) and the variational quantum eigensolver (VQE) algorithms [2], thus opening new avenues to apply HHL for calculating properties of large molecules.

Despite possessing the aforementioned advantages, the HHL algorithm relies upon the probability of successfully postselecting 1 on the HHL ancilla qubit, that is, $P(1)$ [1]. It is known that there can be a substantial decrease in $P(1)$ with increase in the condition number of the problem matrix A, which we shall denote by κ. In other words, the fraction of usable shots in the HHL algorithm becomes very low when large-κ input matrices are involved. Unfortunately, it is not uncommon to encounter the issue while employing HHL for some interesting problems (for example, see Ref. [3] for application of the algorithm to hydrological systems), including quantum chemistry, which we shall discuss in detail in our Results section. Several works in literature have addressed the issue of handling large κ matrices either directly (where κ of the A matrix itself is altered via approaches such as preconditioning) or indirectly [3–9]. For a thorough survey, we direct the reader to Sec. 1.2 of Ref. [10].

In this work, we propose a framework to address the issue of handling A matrices with large condition numbers, by introducing the postselection-improved HHL (Psi-HHL) algorithm, which relies upon the intuition of extracting the correct signal by subtracting a wrong signal from a mixed

*Contact author: srinivasaprasannaa@gmail.com

Published by the American Physical Society under the terms of the Creative Commons Attribution 4.0 International license. Further distribution of this work must maintain attribution to the author(s) and the published article's title, journal citation, and DOI.

signal (that contains both the correct and wrong signals). A signal refers to a scalar that is a feature of $|x\rangle$. This is discussed in Sec. II B, after we introduce briefly the HHL algorithm in Sec. II A. A simple modification involving execution of two (three) HHL routines for overlap computation (expectation value calculation) enables one to carry out calculations for treating systems of linear equations involving large-κ matrices without having to contend with a large number of shots. In fact, we argue that the condition number scales linearly with system size with our approach for large-κ situations (see Sec. II C), while still staying in the realm of a typical HHL computation. This compares favorably with several other notable works in literature, including but not limited to the original HHL work: $\mathcal{O}(\kappa^3)$ and $\mathcal{O}(\kappa^2)$ without and with amplitude amplification, respectively [1], $\mathcal{O}(\kappa \log^3 \kappa)$ with variable time amplitude amplification [5], and works by Childs *et al.*: $\mathcal{O}[\kappa \text{polylog}(\kappa)]$ [11], Wossnig *et al.*: $\mathcal{O}(\kappa^2)$, and Costa *et al.*'s discrete quantum adiabatic approach based quantum linear solver algorithm [12]: $\mathcal{O}(\kappa)$. In particular, the last approach also achieves linear scaling in condition number, but we do so without invoking any additional algorithmic machinery beyond the scope of the traditional HHL algorithm. In order to provide a very qualitative perspective, we note that for condition number of about 1×10^6, $\kappa^3 : \kappa^2 : \kappa \log^3 \kappa : \kappa$ is $\sim 10^{18} : 10^{12} : 7.9 \times 10^9 : 10^6$. For completeness, we add that the best-known classical approach, conjugate gradient, scales as $\mathcal{O}(\sqrt{\kappa})$ [13], but its scaling with respect to system size is, of course, exponentially more expensive than that for HHL. We also address the ability of the Psi-HHL algorithm to handle instances where A is singular in Sec. II D.

For the purposes of this work, we pick the overlap $\mathfrak{o}_{x,b}$ between the input ($|b\rangle$) and output ($|x\rangle$) states of HHL (see Sec. II E 1). In the case of molecules, the quantity corresponds to molecular correlation energies (up to some normalization constants) E_c, as our signal. It is to be noted that Psi-HHL itself is applicable to other features such as expectation values (we explore this option in Sec. II E 2). We also explore a simple representative case where the Psi-HHL framework for overlap calculation can be made a primitive in a larger quantum circuit, in Sec. II F.

Section III presents our results for overlap calculations from numerical simulations for Psi-HHL applied to (a) suitably chosen sets of 4×4, 8×8, 16×16, 32×32, and 64×64 toy matrices, as well as for (b) molecular calculations (64×64 and 256×256 A matrix sizes) in the linearized coupled cluster (LCC) HHL and Psi-HHL frameworks. We conclude in Sec. IV.

II. THEORY AND METHODOLOGY

A. The HHL algorithm

We briefly sketch the relevant details of the HHL algorithm (we refer the readers to Refs. [14–17] for detailed descriptions of the algorithm) in Figs. 1(a) and 1(b), where an amplitude-encoded input $|b\rangle = \sum_i b_i |v_i\rangle$, such that $\sum_i |b_i|^2 = 1$ where $\{|v_i\rangle\}$ refers to the eigenbasis of A, is fed into the HHL algorithm along with n_r number of clock register qubits and one HHL ancillary qubit. The HHL algorithm itself involves QPE, followed by a nontrivial controlled-rotation module, and then a QPE† module. At the end of the circuit, we have the following state vector:

$$\sum_i b_i \left(\sqrt{1 - \frac{C^2}{\tilde{\lambda}_i^2}} |0\rangle + \frac{C}{\tilde{\lambda}_i} |1\rangle \right) \otimes |0^{n_r}\rangle \otimes |v_i\rangle \,. \tag{1}$$

In the above expression, $\{\tilde{\lambda}_i\}$ refers to the estimates of the actual eigenvalues of A ($1 \geqslant \tilde{\lambda}_i \geqslant 1/\kappa$) obtained via the QPE module of HHL. Typically, C is chosen to be the minimum eigenvalue of A, but it is worth noting that incurring the large classical overhead associated with computing it can always be circumvented via approaches such as AdaptHHL [2]. When one postselects the outcome "1" on the HHL ancilla qubit, one can think of it as choosing the "correct" signal.

The solution vector $|x\rangle \propto A^{-1}|b\rangle$, and the input vector $|b\rangle$ can be written as

$$|x\rangle = |x\rangle_{\text{un}} / \| |x\rangle_{\text{un}} \| \text{ and } |b\rangle = |b\rangle_{\text{un}} / \| |b\rangle_{\text{un}} \| \,, \tag{2}$$

respectively, where subscript "un" refers to *unnormalized* states; $|b\rangle_{\text{un}}$ is the unnormalized input state after amplitude encoding and $|x\rangle_{\text{un}} = \sum_i \frac{b_i C}{\tilde{\lambda}_i} |v_i\rangle$, with $\sum_i |b_i|^2 = 1$. The probability of successfully postselecting outcome "1" is given as $P(1) = \| |x\rangle_{\text{un}} \|^2$. Finally, when one wants to predict a feature of the solution vector, say, the overlap between $|x\rangle$ and $|b\rangle$, it can be done by appending an additional circuit (the Hong-Ou-Mandel module [18]), abbreviated as HOM in Fig. 1(b) that inputs the output $|x\rangle$ of the HHL algorithm and $|b\rangle$, to output the overlap between the two quantities. The overlap is then calculated as

$$\begin{aligned} \mathfrak{o}_{x,b}^{\text{HHL}} &= - \| |b\rangle_{\text{un}} \|^2 \, \| |x\rangle_{\text{un}} \| \; |\langle b|x\rangle| \\ &= - \| |b\rangle_{\text{un}} \|^2 \sum_i |b_i|^2 \frac{C}{\tilde{\lambda}_i}. \end{aligned} \tag{3}$$

For the sake of simplicity, we set this quantity hereafter as the feature of $|x\rangle$ that is of interest to us.

The number of trials needed to successfully postselect outcome 1 is $\mathcal{O}(\kappa^2)$. Thus, in the event of large κ, the success probability falls quickly, making it practically difficult to carry computations using large-κ matrices. In this work, we demonstrate a different approach, Psi-HHL, towards handling large-κ matrices by leveraging the probability of successfully postselecting the wrong outcome 0, $P(0)$, in HHL.

B. The Psi-HHL framework

In this section, we introduce the two essential ingredients, HHL_1 and HHL_2, which make up the Psi-HHL framework. For different features (signals) of $|x\rangle$ to be extracted, one employs slightly different sets of circuits that involve HHL_1 and HHL_2 modules. In the HHL_1 module, one executes the HHL circuit as it is, except that the "wrong" signal is postselected, that is, 0 is postselected. The HHL_2 entails the traditional HHL module appended with a mixing 2×2 unitary $[R_Y(2\alpha)]$ on the HHL ancillary qubit just before measurement, and postselecting 1 from the "mixed" signal. The role of this unitary is to mix the coefficients of $|0\rangle$ and $|1\rangle$ in the traditional HHL [see Eq. (1)], thereby outputting a mixed signal.

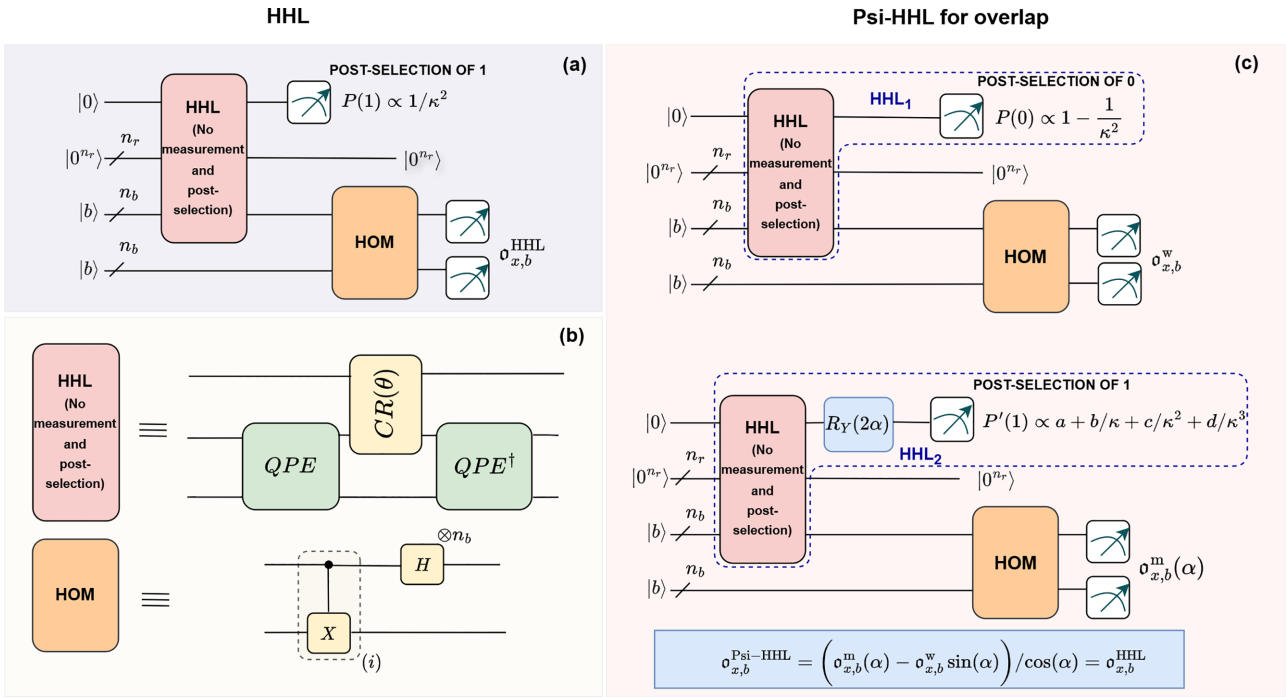


FIG. 1. (a) Schematic of the HHL algorithm, where 1 is postselected and for which $P(1)$ would be low for large κ. $|b\rangle$ is the input state register with n_b qubits, while n_r refers to the number of clock register qubits. The Hong-Ou-Mandel (HOM) module is a destructive version of the controlled-SWAP test without an additional ancilla qubit, and we use it to extract $|\langle b|x\rangle|$, using which we evaluate $\mathfrak{o}_{x,b}^{\mathrm{HHL}} = -\| |b\rangle_{\mathrm{un}} \|^2 \| |x\rangle_{\mathrm{un}} \| \ |\langle b|x\rangle|$ (interpreted as the correlation energy $E_{\mathrm{c}}^{\mathrm{HHL}}$, when HHL is applied to molecular calculations), which is the feature of $|x\rangle$ that we are interested in for our numerical simulations. The subscript "un" stands for unnormalized. (b) Provides a block-diagram description of the HHL and the HOM modules. QPE refers to the quantum phase estimation while CR(θ) refers to the controlled-rotation module that inverts the eigenvalues of A. The CR(θ) circuit is built out of uniformly controlled rotations involving a set of angles $\{\theta_i\}$, denoted compactly as just θ in the figure. The dashed cambered rectangle around the CNOT gate in the HOM circuit module, and which is accompanied by (i), indicates that the gate is controlled on the ith qubit of the $|b\rangle$ register. (c) Shows HHL_1 employed inside an overlap calculation circuit in the top panel, where $P(0)$ is postselected, and also shows HHL_2 used inside an overlap calculation circuit in the bottom panel. In HHL_2, the traditional HHL module is appended with an additional mixing unitary, $R_Y(2\alpha)$, and where $P'(1)$ is postselected. Psi-HHL relies on subtracting the *final* outcomes of these two circuits, and as the expression at the bottom of (c) indicates, we recover $\mathfrak{o}_{x,b}$ (or the correlation energy when applied to molecules) via the procedure to within a simple factor. In our notation, $\mathfrak{o}_{x,b}^{\mathrm{HHL}}$ and $\mathfrak{o}_{x,b}^{\mathrm{Psi\text{-}HHL}}$ are obtained from HHL and Psi-HHL respectively. Further, $a, b, c, d \in \mathbb{R}$ are constants.

1. HHL_1: Computing the wrong signal

The first HHL module, HHL_1, serves to postselect the wrong signal of the HHL ancilla qubit, that is, the state attached to $|0\rangle$ in Eq. (1). We rewrite the state $|\psi_{\mathrm{out}}\rangle$ at the output of all the registers except the clock qubits register, as follows:

$$|\psi_{\mathrm{out}}\rangle = \sum_i b_i \left(\sqrt{1 - \frac{C^2}{\tilde{\lambda}_i^2}} \, |0\rangle \otimes |\nu_i\rangle + \frac{C}{\tilde{\lambda}_i} |1\rangle \otimes |\nu_i\rangle \right) = (|0\rangle \otimes |x_{\mathrm{w}}\rangle + |1\rangle \otimes |x_{\mathrm{r}}\rangle). \tag{4}$$

Note that here $|x_{\mathrm{w}}\rangle$ and $|x_{\mathrm{r}}\rangle$ are the unnormalized vectors in the superposition. The subscripts w and r refer to wrong and correct, respectively, where for the latter, we use r since c is used already to denote correlation. The normalized solution vector $|x_0\rangle$ which appears at the output register after successfully postselecting outcome 0 is given by

$$|x_0\rangle = |x_{\mathrm{w}}\rangle / \| |x_{\mathrm{w}}\rangle \| = \sum_i b_i \sqrt{1 - \frac{C^2}{\tilde{\lambda}_i^2}} \, |\nu_i\rangle \, / \| |x_{\mathrm{w}}\rangle \|, \tag{5}$$

where

$$\| |x_{\mathrm{w}}\rangle \| = \sqrt{P(0)} = \left(\sum_i \left| b_i \sqrt{1 - \frac{C^2}{\tilde{\lambda}_i^2}} \right|^2 \right)^{1/2}. \tag{6}$$

Here, $P(0)$ is the probability of successfully postselecting outcome 0.

2. HHL_2: Computing the mixed signal

The second HHL execution involves attaching the rotation gate $R_Y(2\alpha)$ on the HHL ancillary qubit before the measurement as illustrated in the lower panel of Fig. 1(c). This seemingly trivial addition to the algorithm introduces a new degree of freedom via the angle α, enabling one to boost the probability of successful matrix inversion in the case of large κ. We recall that $R_Y(2\alpha)$ is a rotation about the Y axis on the Bloch sphere as given as

$$R_Y(2\alpha) = \begin{pmatrix} \cos(\alpha) & -\sin(\alpha) \\ \sin(\alpha) & \cos(\alpha) \end{pmatrix}. \tag{7}$$

The state vector at the output of HHL_2 module $|\psi'_{\mathrm{out}}\rangle$, ignoring the clock qubits register, after applying the unitary in Eq. (7) is given as

$$\begin{aligned}|\psi'_{\mathrm{out}}\rangle &= \sum_i b_i \left(\sqrt{1-\frac{C^2}{\tilde{\lambda}_i^2}}\cos(\alpha) - \frac{C}{\tilde{\lambda}_i}\sin(\alpha)\right)|0\rangle \otimes |v_i\rangle \\ &\quad + b_i\left(\sqrt{1-\frac{C^2}{\tilde{\lambda}_i^2}}\sin(\alpha) + \frac{C}{\tilde{\lambda}_i}\cos(\alpha)\right)|1\rangle \otimes |v_i\rangle \\ &= (|0\rangle \otimes |x_{\mathrm{m}}\rangle + |1\rangle \otimes |x'_{\mathrm{m}}\rangle). \end{aligned} \tag{8}$$

Note that in Eq. (8), $|x_{\mathrm{m}}\rangle$ and $|x'_{\mathrm{m}}\rangle$ are unnormalized vectors. The subscript "m" denotes mixed, and while the unprimed vector accompanies $|0\rangle$, the primed one accompanies $|1\rangle$. The solution vector at the output after successfully postselecting outcome 1 is given as

$$\begin{aligned}|x'\rangle &= \frac{|x'_{\mathrm{m}}\rangle}{\| |x'_{\mathrm{m}}\rangle \|} \\ &= \sum_i b_i \left(\sqrt{1-\frac{C^2}{\tilde{\lambda}_i^2}}\sin(\alpha) + \frac{C}{\tilde{\lambda}_i}\cos(\alpha)\right)|v_i\rangle / \| |x'_{\mathrm{m}}\rangle \|, \end{aligned}$$

where

$$\begin{aligned}\| |x'_{\mathrm{m}}\rangle \| &= \sqrt{P'(1)} \\ &= \left(\sum_i \left| b_i \left(\sqrt{1-\frac{C^2}{\tilde{\lambda}_i^2}}\sin(\alpha) + \frac{C}{\tilde{\lambda}_i}\cos(\alpha)\right)\right|^2\right)^{1/2}. \end{aligned} \tag{9}$$

Here, $P'(1)$ is the probability of successfully obtaining outcome 1 in HHL_2.

C. Complexity aspects

We now demonstrate the complexity (in κ) of the Psi-HHL algorithm. We proceed henceforth in this subsection by assuming the condition that the eigenvalues λ_i are precisely captured with adequate number of QPE clock register qubits n_r.

(a) Success probability of the postselection process in HHL_1: The probability of successfully postselecting the outcome 0, $P(0)$, in HHL_1 as given in Eq. (6) can be expanded as [19]

$$\begin{aligned}P(0) &= \sum_i \left| b_i \sqrt{1-\frac{C^2}{\lambda_i^2}}\right|^2 \\ &= \|\sqrt{(\mathbb{I} - C^2A^{-2})}|b\rangle\|^2, \end{aligned} \tag{10}$$

where $\mathbb{I}$ is the identity operator written in the eigenbasis of operator A, constant $C = \mathcal{O}(1/\kappa)$, where the condition number κ is taken as $\lambda_{\max}/\lambda_{\min}$ and $|b\rangle$ is the input to the HHL circuit. The set of values $\{\sqrt{1-\frac{C^2}{\lambda_i^2}}\}$ are the eigenvalues of the operator $\sqrt{\mathbb{I} - C^2A^{-2}}$, with the largest eigenvalue being $\sqrt{1-\frac{C^2}{\lambda_{\max}^2}}$, and therefore

$$\begin{aligned}P(0) &\leqslant \|\sqrt{(\mathbb{I} - C^2A^{-2})}\|_{\mathrm{op}}^2 \||b\rangle\|^2, \\ P(0) &\leqslant 1 - \frac{C^2}{\lambda_{\max}^2} \\ &\leqslant 1 - \frac{1}{\kappa^2}. \end{aligned} \tag{11}$$

The first line uses the property of submultiplicativity of matrix norms, that is, $\|AB\| \leqslant \|A\|\|B\|$. In Eq. (11), we recall that we set $C = \lambda_{\min}$, $\|\cdot\|_{\mathrm{op}}$ is the operator norm, and $\||b\rangle\| = 1$. Note that the smallest eigenvalue of this operator is $\sqrt{1-\frac{C^2}{\lambda_{\min}^2}} = 0$, and corresponds to $P(0) = 0$, which leads to expending a large number of shots in HHL_1. One could circumvent this issue by appropriately choosing a scaled $C = \gamma\lambda_{\min}$, where $\gamma \in (0, 1)$, leading to $P(0) \geqslant 1 - \gamma^2$. This idea has been illustrated via an example as shown in Fig. 2, where we choose the scaling $\gamma = 0.5$.

(b) Success probability of the postselection process in HHL_2: A similar expression for the probability of successful postselection in HHL_2, $P'(1)$, can be obtained by further expanding Eq. (9) as follows:

$$P'(1) = \|[\sqrt{(\mathbb{I} - C^2A^{-2})}\sin(\alpha) + (CA^{-1})\cos(\alpha)]|b\rangle\|^2. \tag{12}$$

The operator $B := \sqrt{\mathbb{I} - C^2A^{-2}}\sin(\alpha) + (CA^{-1})\cos(\alpha)$ in its eigenbasis $\{|v_i\rangle\}$ could be given in the diagonal form as

$$\begin{aligned}&\mathrm{diag}\big[\ldots, \sqrt{1 - C^2/\lambda_{\max}^2}\sin(\alpha) + (C/\lambda_{\max})\cos(\alpha), \ldots, \\ &\sqrt{1 - C^2/\lambda_{\min}^2}\sin(\alpha) + (C/\lambda_{\min})\cos(\alpha), \ldots\big], \end{aligned} \tag{13}$$

where the entries that occur in the parentheses after "diag" are the diagonal elements of the matrix. Note that the largest and smallest eigenvalues of the matrix given in Eq. (13) depend on the choice of α. When $\alpha = \pi/2$, the component of that eigenvalue attached to $\sin(\alpha)$ remains, and we do not extract the desired solution. However, when α is too small, say 0, the component attached to $\cos(\alpha)$ remains and we get the same complexity as the traditional HHL approach. Therefore, α is chosen to satisfy the following properties:

(1) The success probability $P'(1)$ is large enough.

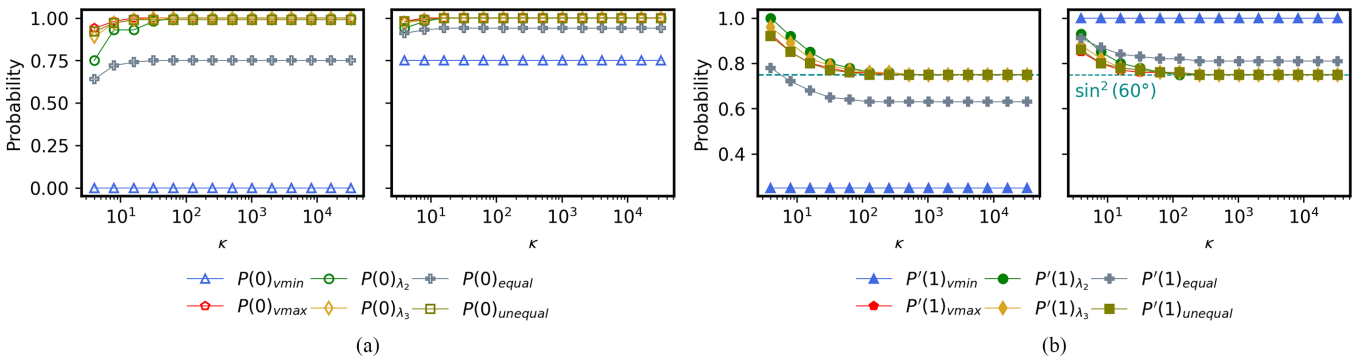
(2) The solution component that matters to us does not vanish in the superpositions that occur along the diagonal entries in Eq. (13).

We demonstrate the case where α is close to $\pi/2$ and $C = \lambda_{\min}$, in which case the operator in Eq. (13) could be written in the form where the largest eigenvalue is the first entry and the smallest eigenvalue is the last entry, as given below,

$$\mathrm{diag}[\ldots, \sqrt{1 - 1/\kappa^2}\sin(\alpha) + (1/\kappa)\cos(\alpha), \ldots, \cos(\alpha)]. \tag{14}$$

Using once again the submultiplicativity of matrix norms in Eq. (12), we can write

$$\begin{aligned}P'(1) \leqslant \|[&\sqrt{\mathbb{I} - \mathrm{C}^2\mathrm{A}^{-2}}\sin(\alpha) \\ &+ CA^{-1}\cos(\alpha)]\|_{\mathrm{op}}^2 \||b\rangle\|^2, \end{aligned} \tag{15}$$



(a) (b)

FIG. 2. Figure showing probabilities of postselecting various outcomes in Psi-HHL. (a), (b) Show the behavior of $P(0)$ and $P'(1)$, respectively, with κ, for A being a 4×4 diagonal matrix and with six different choices for the vector $\vec{b}$: $P(0)_{\text{vmin}}$ corresponds to the case where $\vec{b}$ is the eigenvector associated with the minimum eigenvalue of A, $P(0)_{\text{vmax}}$ is the case where $\vec{b}$ is the eigenvector associated with the maximum eigenvalue of A, $P(0)_{\lambda_2}$ and $P(0)_{\lambda_3}$ correspond to the situations where $\vec{b}$ is the eigenvector associated with two other eigenvalues of A, $P(0)_{\text{equal}}$ is the case where $\vec{b}$ is in equal superposition of all eigenstates of A, and finally $P(0)_{\text{unequal}}$ considers the scenario where $\vec{b}$ is in an arbitrary superposition of eigenstates of A. In the leftmost figure of (a), we choose the parameter C as $\lambda_{\min}$, that is, the minimum eigenvalue of A, whereas in rightmost figure of (a), $C = 0.5\lambda_{\min}$, that is, γ is set to 0.5. (b) Represents $P'(1)$ where the legend's labels have a similar interpretation to those of $P(0)$. The HHL and Psi-HHL calculations were done using 1×10^6 shots, and α was set to 60° for Psi-HHL.

where $\|\cdot\|_{\text{op}}$ is the operator norm yielding the largest eigenvalue of the operator, and $\||b\rangle\| = 1$. Then $P'(1)$ is bounded the following way:

$$\begin{aligned}\cos^2(\alpha) \leqslant P'(1) &\leqslant \left|\left[\left(\sqrt{1-\frac{1}{\kappa^2}}\right)\sin(\alpha)+\frac{1}{\kappa}\cos(\alpha)\right]\right|^2 \\ &= \left(1-\frac{1}{\kappa^2}\right)\sin^2(\alpha)+\frac{1}{\kappa^2}\cos^2(\alpha) \\ &\quad + 2\left(\sqrt{1-\frac{1}{\kappa^2}}\right)\frac{1}{\kappa}\sin(\alpha)\cos(\alpha) \\ &\leqslant \sin^2(\alpha)+\frac{1}{\kappa}\sin(2\alpha)+\frac{1}{\kappa^2}\cos(2\alpha) \\ &\quad -\frac{1}{\kappa^3}\sin(\alpha)\cos(\alpha). \end{aligned} \tag{16}$$

In this bound, the left-hand side is the square of the smallest eigenvalue of the matrix given in Eq. (14), while the right-hand side is the square of the largest eigenvalue of the matrix in Eq. (14).

We note that the scaling analysis discussed in this section is independent of the feature extraction module, and is focused on the ease or difficulty of postselection that happens before it. That is, as long as one can design circuits based on the HHL_1 and the HHL_2 modules such that mixed and wrong signals cancel to yield the correct signal, the linear scaling is preserved.

For the choice of $C = \gamma\lambda_{\min}$, where $\gamma \in (0, 1)$, one can push the lower bound for the choice of given α. This implies that fewer measurements are required to invert matrices with large condition numbers, as compared to the traditional HHL technique illustrated in Fig. 1(a). We obtain

$$\left|\left[\left(\sqrt{1-\frac{\gamma^2}{\kappa^2}}\right)\sin(\alpha)+\frac{\gamma}{\kappa}\cos(\alpha)\right]\right|^2 \leqslant P'(1) \leqslant \left|\left[(\sqrt{1-\gamma^2})\sin(\alpha)+\gamma\cos(\alpha)\right]\right|^2. \tag{17}$$

We show this in Fig. 2, where we pick $\alpha = 60^\circ$, the choice of A matrix is $A = \begin{pmatrix} 0.25 & 0.00 & 0.00 & 0.00 \\ 0.00 & 0.75 & 0.00 & 0.00 \\ 0.00 & 0.00 & 0.50 & 0.00 \\ 0.00 & 0.00 & 0.00 & 1.00 \end{pmatrix}$, and with six different choices of $\vec{b}$ (the eigenvector associated with the minimum eigenvalue of A, the eigenvector associated with the maximum eigenvalue of A, eigenvector associated with two other eigenvalues of A, equal superposition of all eigenstates of A, and an arbitrary superposition of eigenstates of A).

While the A and B matrices share the same basis $\{|v_i\rangle\}$, an eigenstate of B matrix that achieves the lower bound for $P'(1)$ may not often correspond to the largest or smallest eigenvalue of A matrix, for a given choice of angle α.

Note that for an arbitrary input $|b\rangle$ which is a nontrivial superposition of all the eigenvectors $\{|v_i\rangle\}$ of A, we have the following condition:

$$\begin{aligned} P'(1) &= \left(\sum_i \left| b_i \left(\sqrt{1-\frac{C^2}{\lambda_i^2}}\sin(\alpha)+\frac{C}{\lambda_i}\cos(\alpha)\right)\right|^2\right) \\ &= \left(\sum_i |\, b_i\,|^2\, \lambda_i'^2\right). \end{aligned} \tag{18}$$

Here, $\{\lambda_i'\}$ are the eigenvalues of the operator $\sqrt{\mathbb{I} - C^2A^{-2}}\ \sin(\alpha) + CA^{-1}\cos(\alpha)$. Equation (18) is a convex combination of the square of eigenvalues $\lambda_i'^2$,

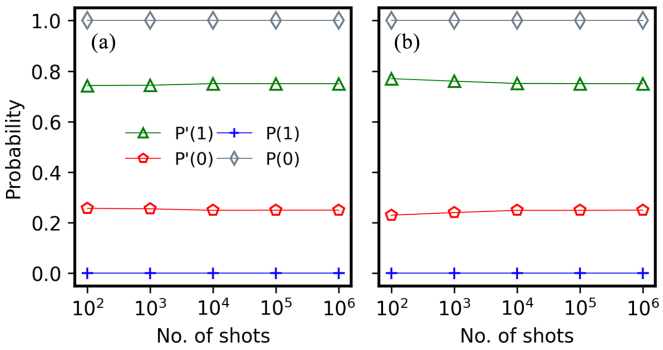


FIG. 3. Figure showing the performance of HHL and Psi-HHL for singular matrices of size 2×2 (a) and 4×4 (b).

therefore, an arbitrary input $|b\rangle$ will yield a $P'(1)$ satisfying the condition given in Eq. (16). We augment our findings with the simulations in the subsequent Sec. III.

D. Singular matrices

When the HHL algorithm is executed for a large system size for some target application, the user ideally should not possess knowledge of some crucial properties of A, including its condition number and invertibility. In the extreme event that A happens to be singular and its condition number is not known *a priori*, the algorithm always outputs 0, that is, $P(1) = 0$, and a user has to supply a rather large number of shots before perhaps drawing on the realization that the problem may not produce a 1. However, Psi-HHL, by construction, circumvents this issue that HHL suffers from. For illustration, we pick two small but extreme examples, as follows:

(1) A 2×2 matrix given by $A = \begin{pmatrix} 0.25 & 0.00 \\ 0.00 & 0.00 \end{pmatrix}$ and the $\vec{b}$ is $\begin{pmatrix} 0.00 \\ 1.00 \end{pmatrix}$,

(2) A 4×4 matrix $A = \begin{pmatrix} 1.00 & 2.00 & 0.00 & 0.00 \\ 2.00 & 4.00 & 0.00 & 0.00 \\ 0.00 & 0.00 & 0.00 & 0.00 \\ 0.00 & 0.00 & 0.00 & 2.00 \end{pmatrix}$ and with $\vec{b} = \begin{pmatrix} 0.00 \\ 0.00 \\ 1.00 \\ 0.00 \end{pmatrix}$.

In both the cases above $\vec{b} \in N(A)$, such that $N(A)$ is the null space of A matrix. We execute HHL as well as Psi-HHL for these two cases by setting $C/\lambda_i = 0$ whenever the eigenvalues of A are zero, that is, $\lambda_i = 0$. The traditional HHL algorithm would expend all the supplied shots without being able to postselect outcome 1, since $P(1) = 0$. The HHL_1 of Psi-HHL successfully postselects outcome 0 with probability $P(0) = 1$. On the other hand, the HHL_2 module of Psi-HHL postselects outcome 1 with probability $\sin^2(\alpha)$ [see Eq. (8)]. The data points presented in Fig. 3 demonstrate these probabilities for the two examples considered. Both these HHLs yield the solution $|x\rangle = |b\rangle$. The overlap $|\langle x|b\rangle|$ from the HOM module in HHL_1 and HHL_2 both yield a value of 1, with all of the additional $\sin(\alpha)$ factors canceling out (see Fig. 1). Subtracting the two overlap values results in 0, as expected. Thus, the Psi-HHL approach proves powerful when $P(0) \gg P(1)$. We now consider the case when $\vec{b}$ is an eigenvector of A. Here too, one could still get the same result via Psi-HHL by choosing the evolution time t, as a multiple of 2π, which could be incorrect. Therefore, in order to reliably calculate the outputs from both the cases using Psi-HHL, one chooses a nontrivial t in the QPE module, such that it is not an integral multiple of 2π, in order to avoid the possibility of obtaining $\lambda_i = 0$ for both the cases. Choosing a nontrivial t will resolve this issue, in the following way:

(1) In the case where $\vec{b}$ is an eigenvector of A, one obtains an eigenvalue $\lambda_i \neq 0$, yielding an associated nontrivial controlled-rotation angle θ_i.

(2) However, when $\vec{b}$ is a null-space vector, one would still obtain an eigenvalue $\lambda_i = 0$ leading to a controlled-rotation angle of 0.

It is worth adding that a striking feature of Psi-HHL is that the approach, unlike amplitude amplification, for example, needs no additional circuit elements or primitives, and thus the requirements on the properties of A to execute the HHL algorithm are the same those for Psi-HHL too. Psi-HHL additionally accommodates the possibility of handling singular matrices, but this comes about not due to requirements from the properties of A but rather the act of subtracting signals.

E. The Psi-HHL approach for extracting features of the solution vector

1. Overlap calculation using Psi-HHL

We recall that Fig. 1(c) shows how HHL_1 and HHL_2 are employed as subroutines in larger circuits to extract the overlap $\mathfrak{o}_{x,b}$. We subtract the $\mathfrak{o}_{x,b}$ values associated with these circuits involving HHL_1 and HHL_2, thus leaving us with the $\mathfrak{o}_{x,b}$ corresponding to the "correct" signal. The gain in taking this route is the efficiency that we achieve in the number of shots expended. We summarize this in the following proposition:

Proposition 1. Psi-HHL yields the same overlap value $\mathfrak{o}_{x,b}$ as traditional HHL through two implementations of HHL, but is more efficient in the number of shots than HHL, especially when dealing with A matrices with large condition numbers.

The overlap obtained from the circuit presented in the top panel of Fig. 1(c) is then given as

$$\mathfrak{o}^{\text{w}}_{x,b} = -\||b\rangle_{\text{un}}\|^2 \, \||x_{\text{w}}\rangle\| \, |\langle b|x_0\rangle|. \tag{19}$$

In the expression given above, $|b\rangle_{\text{un}}$ is the unnormalized input vector after amplitude encoding, and

$$|\langle b|x_0\rangle| = \frac{\sum_i |b_i|^2 \sqrt{1 - \frac{C^2}{\lambda_i^2}}}{\||x_{\text{w}}\rangle\|}. \tag{20}$$

On the other hand, the circuit presented in the bottom panel of Fig. 1(c) yields

$$\mathfrak{o}^{\text{m}}_{x,b} = -\||b\rangle_{\text{un}}\|^2 \, \||x'_{\text{m}}\rangle\| \, |\langle b|x'\rangle|, \tag{21}$$

where

$$|\langle b|x'\rangle| = \frac{\sum_i |b_i|^2 \left(\sqrt{1 - \frac{C^2}{\lambda_i^2}} \sin(\alpha) + \frac{C}{\lambda_i} \cos(\alpha)\right)}{\||x'_{\text{m}}\rangle\|}. \tag{22}$$

We choose α such that $\sin(\alpha)$ and $\cos(\alpha)$ are positive and $P'(1) \gg P'(0)$. $P'(0)$ refers to the probability of postselecting outcome 0 in HHL_2.

In order to obtain the correct overlap value, we subtract Eqs. (21) and (19), thus leading to

$$\mathfrak{o}_{x,b}^{\text{Psi-HHL}}\cot(\alpha) = \frac{\mathfrak{o}_{x,b}^{\text{m}}}{\sin(\alpha)} - \mathfrak{o}_{x,b}^{\text{w}} = -\| |b\rangle_{\text{un}} \|^2 \sum_i |b_i|^2 \frac{C}{\tilde{\lambda}_i}\cot(\alpha). \quad (23)$$

By comparing the right-hand sides of Eqs. (3) and (23), we see that the expressions for $\mathfrak{o}_{x,b}^{\text{HHL}}$ and $\mathfrak{o}_{x,b}^{\text{Psi-HHL}}$ are the same as shown below:

$$\mathfrak{o}_{x,b}^{\text{Psi-HHL}} = \frac{\mathfrak{o}_{x,b}^{\text{m}} - \mathfrak{o}_{x,b}^{\text{w}}\sin(\alpha)}{\cos(\alpha)} = \mathfrak{o}_{x,b}^{\text{HHL}}. \quad (24)$$

Although theoretically, we obtain the same overlap value from Psi-HHL, we observe that this technique is superior to traditional HHL in the way it handles large-κ matrices, due to the optimal probability of success that one achieves while postselecting, as we explain in the subsequent section. Therefore, $\mathfrak{o}_{x,b}^{\text{Psi-HHL}}$ can predict the true overlap value, $\mathfrak{o}_{x,b}$, to a reasonable level of precision with fewer shots even for values of κ where HHL procedure fails to do so, which we illustrate in the Results section with examples. We find through our examples that for up to fairly large values of κ that are well beyond those that HHL can handle, Psi-HHL predicts $\mathfrak{o}_{x,b}$ with fewer shots.

We also add that in problems where it is not immediately obvious *a priori* that the condition number is large, one cannot determine whether to employ HHL or Psi-HHL. However, this is not a problem as Psi-HHL intrinsically involves the regular HHL procedure and, hence, if $P(1)$ is significant, one can choose not to opt for the Psi-HHL procedure.

Overlap calculation along with sign information. It is important to note that the HOM module discussed in Sec. II E 1 gives the absolute value of the overlap. We discuss the Psi-HHL circuits required to obtain the overlap value without losing the sign information. Figures 4(a) and 4(b) present the relevant circuits [we see that in order to extract overlap values with sign information, we need to incur controlled versions of HHL_1 and HHL_2 (without measurement and post-selection under control)] for obtaining the wrong and mixed signals, respectively. The former gives $\langle b|x_{\text{w}}\rangle = [(2\mathcal{P}_R(0) - 1) + i(2\mathcal{P}_I(0) - 1)]\mathfrak{b}$ with $\mathfrak{b} = \frac{1}{2}(1 + \| |x_{\text{w}}\rangle \|^2)$. We note that $\| |x_{\text{w}}\rangle \|^2$ is obtained from the postselection step in Fig. 4(a). $\mathcal{P}$ is the probability obtained in the measurement step at the end of the circuit (as opposed to the usual P or P' that is used for denoting probability that occurs in the postselection step) and the subscripts "R" and "I" are to denote the circuits used to obtain real and imaginary parts of the quantity of interest. The latter gives $\langle b|x'_{\text{m}}\rangle = [(2\mathcal{P}'_R(0) - 1) + i(2\mathcal{P}'_I(0) - 1)]\beta$ with $\beta = \frac{1}{2}(1 + \| |x'_{\text{m}}\rangle \|^2)$. Here, $\| |x'_{\text{m}}\rangle \|^2$ is obtained from the postselection step in Fig. 4(b). Thus, knowing that $\langle b|x'_{\text{m}}\rangle = \sin(\alpha)\langle b|x_{\text{w}}\rangle + \cos(\alpha)\langle b|x_{\text{r}}\rangle$, we could compute the right signal as

$$\langle b|x_{\text{r}}\rangle = \frac{1}{\cos(\alpha)}(\langle b|x'_{\text{m}}\rangle - \sin(\alpha)\langle b|x_{\text{w}}\rangle). \quad (25)$$

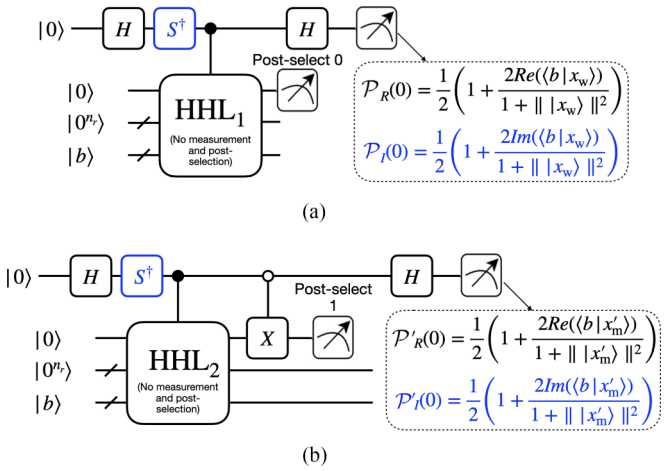


FIG. 4. Circuits for obtaining the overlap values in the Psi-HHL framework. The blue parts are relevant when one evaluates the imaginary part.

A step-by-step evaluation of the proposed circuits is discussed in Appendix A.

2. Expectation value calculation using Psi-HHL

In this subsection, we discuss the applicability of Psi-HHL to expectation value ($\langle x_{\text{r}}|\mathcal{U}|x_{\text{r}}\rangle$) calculations. It is critical to notice that Psi-HHL for overlap extraction works because of perfect cancellation between the mixed and wrong signals. However, when we extend the idea to expectation value evaluation via the Hadamard test module in place of the HOM module, as shown in Figs. 5(a) and 5(b), a cross term remains. This is because the circuit in Fig. 5(b) yields $\langle x'_{\text{m}}|\mathcal{U}|x'_{\text{m}}\rangle = \sin^2(\alpha)\langle x_{\text{w}}|\mathcal{U}|x_{\text{w}}\rangle + 2\sin(\alpha)\cos(\alpha)\text{Re}\langle x_{\text{w}}|\mathcal{U}|x_{\text{r}}\rangle + \cos^2(\alpha)\langle x_{\text{r}}|\mathcal{U}|x_{\text{r}}\rangle$. The issue of imperfect cancellation can be addressed by evaluating an additional circuit, as shown in Fig. 5(c). The probability of measuring 0 on the first qubit from the top is $\bar{P}(0) = \frac{1}{2}(1 + \frac{2\,\text{Re}(\langle x_{\text{w}}|\mathcal{U}|x'_{\text{m}}\rangle)}{\| |x_{\text{w}}\rangle \|^2 + \| |x'_{\text{m}}\rangle \|^2})$. Through this equation, we calculate the term $\text{Re}(\langle x_{\text{w}}|\mathcal{U}|x'_{\text{m}}\rangle)$. Thus, the cross term $\text{Re}(\langle x_{\text{w}}|\mathcal{U}|x_{\text{r}}\rangle) = \frac{\delta}{\cos(\alpha)}[2\bar{P}(0) - 1] - \frac{\sin(\alpha)}{\cos(\alpha)}[2\mathcal{P}_R(0) - 1]\| |x_{\text{w}}\rangle \|^2$, where $\delta = \frac{1}{2}(\| |x_{\text{w}}\rangle \|^2 + \| |x'_{\text{m}}\rangle \|^2)$. The final correct expectation value $\langle x_{\text{r}}|\mathcal{U}|x_{\text{r}}\rangle$ is obtained by subtracting the quantities $\langle x_{\text{w}}|\mathcal{U}|x_{\text{w}}\rangle = [(2\mathcal{P}_R(0) - 1) + i(2\mathcal{P}_I(0) - 1)]\| |x_{\text{w}}\rangle \|^2$ obtained from Fig. 5(a) and $\text{Re}(\langle x_{\text{w}}|\mathcal{U}|x_{\text{r}}\rangle)$ obtained from Fig. 5(c), via the term $\langle x'_{\text{m}}|\mathcal{U}|x'_{\text{m}}\rangle = [(2\mathcal{P}'_R(0) - 1) + i(2\mathcal{P}'_I(0) - 1)]\| |x'_{\text{m}}\rangle \|^2$. Its expression is

$$\langle x_{\text{r}}|\mathcal{U}|x_{\text{r}}\rangle = \frac{1}{\cos^2(\alpha)}[\langle x'_{\text{m}}|\mathcal{U}|x'_{\text{m}}\rangle - \sin^2(\alpha)\langle x_{\text{w}}|\mathcal{U}|x_{\text{w}}\rangle - 2\sin(\alpha)\cos(\alpha)\text{Re}\langle x_{\text{w}}|\mathcal{U}|x_{\text{r}}\rangle], \quad (26)$$

where the values of $\| |x_{\text{w}}\rangle \|^2$, $\| |x'_{\text{m}}\rangle \|^2$ and δ are, respectively, the probabilities of postselection in Figs. 5(a)–5(c). Thus, the idea of Psi-HHL works for expectation value evaluation too, with the need to introduce an additional circuit to facilitate cancellation of the mixed and wrong signals to obtain the correct signal. An outline of the protocol is presented in Appendix B.

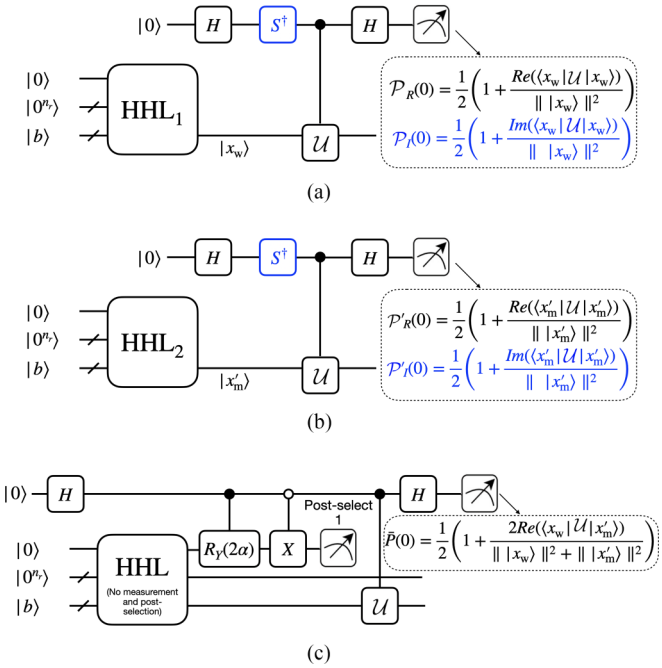


FIG. 5. Circuits for carrying out an expectation value calculation in the Psi-HHL framework. While HHL_1 yields the wrong signal (a), HHL_2 has not only the mixed signal but also cross terms (b). This necessitates employing an additional circuit to cancel the latter (c), thus recovering the correct signal, that is, the expectation value $\langle x_\mathrm{r}|\mathcal{U}|x_\mathrm{r}\rangle$. In (a) and (b), the blue parts are relevant when one evaluates the imaginary part.

3. *Transition matrix element* ($|\langle x_\mathrm{r}|W|\zeta\rangle|$) *calculation using Psi-HHL*

We now briefly comment on the extension of Psi-HHL framework for overlap calculation to transition matrix element ($|\langle x_\mathrm{r}|W|\zeta\rangle|$) calculation. Psi-HHL only requires $|x_\mathrm{w}\rangle$ and $|x'_\mathrm{m}\rangle$ as the outputs from the HHL_1 and the HHL_2 steps, respectively. We recall from Fig. 1 that these two states are inputted into their respective HOM modules. Since Psi-HHL does not place any restriction on the *second* state that is inputted to the HOM module, one can always consider an arbitrary state $|w\rangle = W|\zeta\rangle$ in the place of $|b\rangle$. This naturally extends the applicability of Psi-HHL to transition matrix elements.

F. Psi-HHL as an algorithmic primitive

When HHL is used as a primitive in larger algorithms, it can still be limited when κ is large. In such instances, Psi-HHL can become useful as a primitive. To showcase that the feature extraction still works as intended when Psi-HHL is a primitive in a larger algorithm, we pick a simple case of wanting to not extract a feature of $|x\rangle$, but rather a feature of a state of which $|x\rangle$ is a part. For that purpose, we pick a representative example where we evaluate the overlap $|\langle\Psi_{\mathrm{w/m}}|\Phi\rangle|$, where $|\Phi\rangle = V\,|\chi\rangle$ and $|\Psi_{\mathrm{w/m}}\rangle = \frac{1}{\sqrt{2}}(|x_{\mathrm{w/m}}y\rangle + |yx_{\mathrm{w/m}}\rangle)$, where the indices w and m, respectively, denote the wrong and the mixed signals' solutions. $|y\rangle = \sum_j y_j\,|v_j\rangle$ and $|\chi\rangle$ are states obtained as outputs from either HHL or other algorithm(s). For simplicity, our example is such that state $|y\rangle$ has the same dimension as the state $|x\rangle$. We also make another simplifying assumption

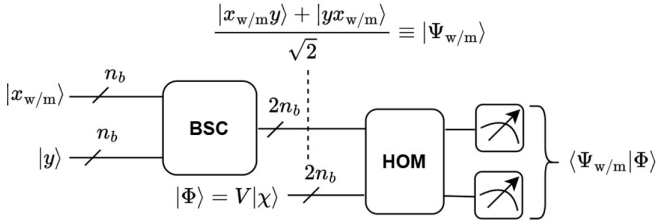


FIG. 6. A schematic of the scenario that we explore for the suitability of Psi-HHL. The feature of interest to us is an overlap $|\langle\Psi_{\mathrm{w/m}}|\Phi\rangle|$, where $|\Phi\rangle = V\,|\chi\rangle$. HOM refers to the Hong-Ou-Mandel circuit module while BSC refers to Bell-state circuit which helps to prepare $|\Psi_{\mathrm{w/m}}\rangle = \frac{1}{\sqrt{2}}(|x_{\mathrm{w/m}}y\rangle + |yx_{\mathrm{w/m}}\rangle)$ given the inputs $|x_{\mathrm{w/m}}\rangle$ and $|y\rangle$.

that the coefficients are real. We find that Psi-HHL indeed accommodates such scenarios, with no additional overheads.

Figure 6 presents the representative situation of interest to us. We define the quantities involved in the eigenbasis of A, the correct state vector:

$$|\Psi_\mathrm{r}\rangle = \frac{1}{\sqrt{2}}(|xy\rangle + |yx\rangle) \tag{27}$$

$$= \frac{1}{\sqrt{2}}\sum_{i,j}\frac{C}{\lambda_i}b_i y_j\,|\beta_{ij}\rangle\,/\||x_{\mathrm{un}}\rangle\|, \tag{28}$$

where $|\beta_{ij}\rangle = |v_i v_j\rangle + |v_j v_i\rangle$, and

$$|\Psi_\mathrm{w}\rangle = \frac{1}{\sqrt{2}}(|x_0 y\rangle + |yx_0\rangle) \tag{29}$$

$$= \frac{1}{\sqrt{2}}\sum_{i,j} b_i\sqrt{1-\frac{C^2}{\lambda_i^2}}\,y_j\,|\beta_{ij}\rangle\,/\||x_\mathrm{w}\rangle\|, \tag{30}$$

and the mixed signal is

$$|\Psi_\mathrm{m}\rangle = \frac{1}{\sqrt{2}}(|x'y\rangle + |yx'\rangle) \tag{31}$$

$$= \frac{1}{\sqrt{2}}\sum_{i,j} b_i\left(\sqrt{1-\frac{C^2}{\lambda_i^2}}\,\sin(\alpha) + \frac{C}{\lambda_i}\cos(\alpha)\right)y_j\,|\beta_{ij}\rangle\,/\||x'_\mathrm{m}\rangle\|. \tag{32}$$

The state $|\Phi\rangle$ is written as

$$|\Phi\rangle = \sum_{k,l} v_{kl}\,|v_k v_l\rangle\,. \tag{33}$$

Thus, the feature that we seek, that is, the correct signal, is given by

$$|\langle\Psi_\mathrm{r}|\Phi\rangle| = \frac{1}{\sqrt{2}}\sum_{i,j}\frac{C}{\lambda_i}b_i y_j(v_{ij}+v_{ji})/\||x_{\mathrm{un}}\rangle\|. \tag{34}$$

We now evaluate the expressions for the wrong and the mixed signals, given by

$$|\langle\Psi_\mathrm{w}|\Phi\rangle| = \frac{1}{\sqrt{2}}\sum_{i,j} b_i\sqrt{1-\frac{C^2}{\lambda_i^2}}\,y_j(v_{ij}+v_{ji})/\||x_\mathrm{w}\rangle\| \tag{35}$$

and

$$|\langle\Psi_{\rm m}|\Phi\rangle| = \frac{1}{\sqrt{2}}\left(\sum_{i,j} b_i\sqrt{1-\frac{C^2}{\lambda_i^2}}b_i y_j(v_{ij}+v_{ji})\sin(\alpha) + \frac{C}{\lambda_i}b_i y_j(v_{ij}+v_{ji})\cos(\alpha)\right)/\||x_{\rm m}\rangle\|, \quad (36)$$

respectively, and we can now make use of the relation $[\langle\Psi_{\rm m}|\Phi\rangle| \times \||x_{\rm m}\rangle\| - |\langle\Psi_{\rm w}|\Phi\rangle| \times \||x_{\rm w}\rangle\| \sin(\alpha)]/\cos(\alpha)$ to recover the correct signal as $|\langle\Psi_{\rm r}|\Phi\rangle| \times \||x_{\rm un}\rangle\| = \frac{1}{\sqrt{2}}\sum_{i,j}\frac{C}{\lambda_i}b_i y_j\,|\beta_{ij}\rangle$. The state $|\Phi\rangle$, as Fig. 6 shows, is constructed by starting with an input state $|\chi\rangle$ and acting it upon by a unitary V. Thus, the feature of interest to us can also be viewed as a transition matrix element.

III. RESULTS AND DISCUSSIONS

In this section, we consider two sets of examples to compare the performance of Psi-HHL with that of HHL:

Toy A matrices of sizes 4×4, 8×8, 16×16, 32×32, *and* 64×64. For practical reasons associated with (classical) computational resources, we do not choose matrices whose κ grows with the A matrix size. Instead, we generate a sequence of A matrices with systematically increasing condition numbers for every system size. For example, for 4×4 matrix size, we begin with a sparse and diagonally dominant matrix (the latter is not a requirement but simplifies matters for our illustrations) such that its smallest diagonal entry is $2^{-(n_r-1)}$ and the largest 1. Recall that n_r is the number of QPE clock register qubits. We generate the sequence by varying n_r from 2 to 20. In such a sequence, κ grows exponentially with n_r, thus enabling us to reach the failure point of HHL rather rapidly and with existing computational resources. We also note that changing the position of the minimum diagonal element of A along the diagonal does not affect our analysis.

Quantum chemistry. Since quantum chemistry is one of the main applications of interest with quantum computers, it is worth exploring this domain for our analysis [2]. However, since we no longer are considering toy examples, we begin by *qualitatively* assessing the applicability of HHL to the LCC problem by checking how the A matrices grow with system size (and along the way, defining the system size), thereby providing a handle on the classical hardness of the problem. We also check the growth of κ itself with what we set to be the system size. Following this analysis, we move to our main results for this problem domain.

We carry out the following analyses:

(1) For the toy matrices, we compare HHL and Psi-HHL, and demonstrate the ability of the latter in predicting $\mathfrak{o}_{x,b}$ across a range of condition number values. We quantify the quality of our results for the $\mathfrak{o}_{x,b}$ values through percentage fraction difference, abbreviated as PFD, given by $\frac{\mathfrak{o}_{x,b}-\mathfrak{o}_{x,b}^{\rm HHL}}{\mathfrak{o}_{x,b}}\times 100$ for HHL and $\frac{\mathfrak{o}_{x,b}-\mathfrak{o}_{x,b}^{\rm Psi\text{-}HHL}}{\mathfrak{o}_{x,b}}\times 100$ for Psi-HHL. We denote the overlap obtained using a suitable classical algorithm (we term it as "classical value" hereafter) by $\mathfrak{o}_{x,b}$, whereas $\mathfrak{o}_{x,b}^{\rm HHL}$ and $\mathfrak{o}_{x,b}^{\rm Psi\text{-}HHL}$ are the values for the quantity obtained from HHL and Psi-HHL, respectively. As we shall explain later in this section, we find that since κ grows polylogarithmically for the quantum chemistry case, it is not computationally feasible for us to simulate system sizes where HHL breaks down.

(2) For both the toy matrices as well as the quantum chemistry matrices, we study the PFDs of HHL and Psi-HHL approaches versus the number of shots.

(3) Additionally, for the chemistry case, we compare the performance of HHL and Psi-HHL across a limited range of geometries on a potential energy curve (PEC) for a suitably chosen molecule.

All of our simulations are developed and executed on the Qiskit software development kit [20].

A. Toy matrices: 4 × 4 through 64 × 64

We begin by discussing the details of our A matrices and $\vec{b}$ vectors. We pick our 4×4 matrix to be nondiagonal, and is given by

$$A = \begin{pmatrix} 2^{-(n_r-1)} & 0.00 & 0.00 & 0.00 \\ 0.00 & 0.75 & 0.10\times10^{-3} & 0.00 \\ 0.00 & 0.10\times10^{-3} & 0.50 & 0.00 \\ 0.00 & 0.00 & 0.00 & 1.00 \end{pmatrix},$$

and $\vec{b} = \begin{pmatrix} 0.10 \\ 0.01 \\ 0.20 \\ 1.00 \end{pmatrix}$. The sparsity s of A is defined as the number of nonzero entries in the row with the most number of nonzero elements, and is set to 2. Our choices for the other matrices, 8×8 through 64×64, can be found in Fig. 14 of the Appendix. We have set the following values for sparsity: 3 for 8×8, 4 for 16×16, 5 for 32×32, and 7 for 64×64 matrices. Throughout, we have ensured that the eigenvalues of the A matrix lie between $1/\kappa$ and 1. We provide more examples for the 4×4 matrix size in Appendix C.

Figures 7(a) through 7(e) provide our findings for 4×4 through the 64×64 examples considered. Each data point in the subfigures is the average result obtained over 10 repetitions, with each repetition involving 1×10^6 shots. For the Psi-HHL results, we set α to be 60°. Each subfigure provides two sets of data: one which compares the probabilities $P(0)$, $P(1)$, $P'(0)$, and $P'(1)$, obtained by executing HHL and Psi-HHL, and the other providing the PFDs for the two methods. We choose condition numbers all the way until about1×10^6. The figures show that our data fits for HHL align with the expected behavior of $P(1)\propto\kappa^{-2}$. We also find that $P'(1)$ scales as $\propto 1$ for large condition numbers (with the fit parameter $a_1 = 0.75$ matching with the Y-axis intercept for large condition number values). We also consider two more cases, where A is diagonal but $\vec{b}$ is in an equal superposition, and A diagonal and $\vec{b}$ in an unequal superposition. Furthermore, we also consider the situations where α is set to 70° and 80°. The data for all of these cases are presented in Figs. 15 and 16 of the Appendix, accompanied by Tables I through III. We also verify that the observed trends do not change with 50 repetitions, for which we pick the 4×4 matrix (with $\alpha = 60^\circ$ for the Psi-HHL calculations) from Fig. 7 as a representative example (see Figs. 17 and 18 of the Appendix). The corresponding data are given in Table IV of the Appendix. Results obtained using other choices of angles, 70° and 80°, are

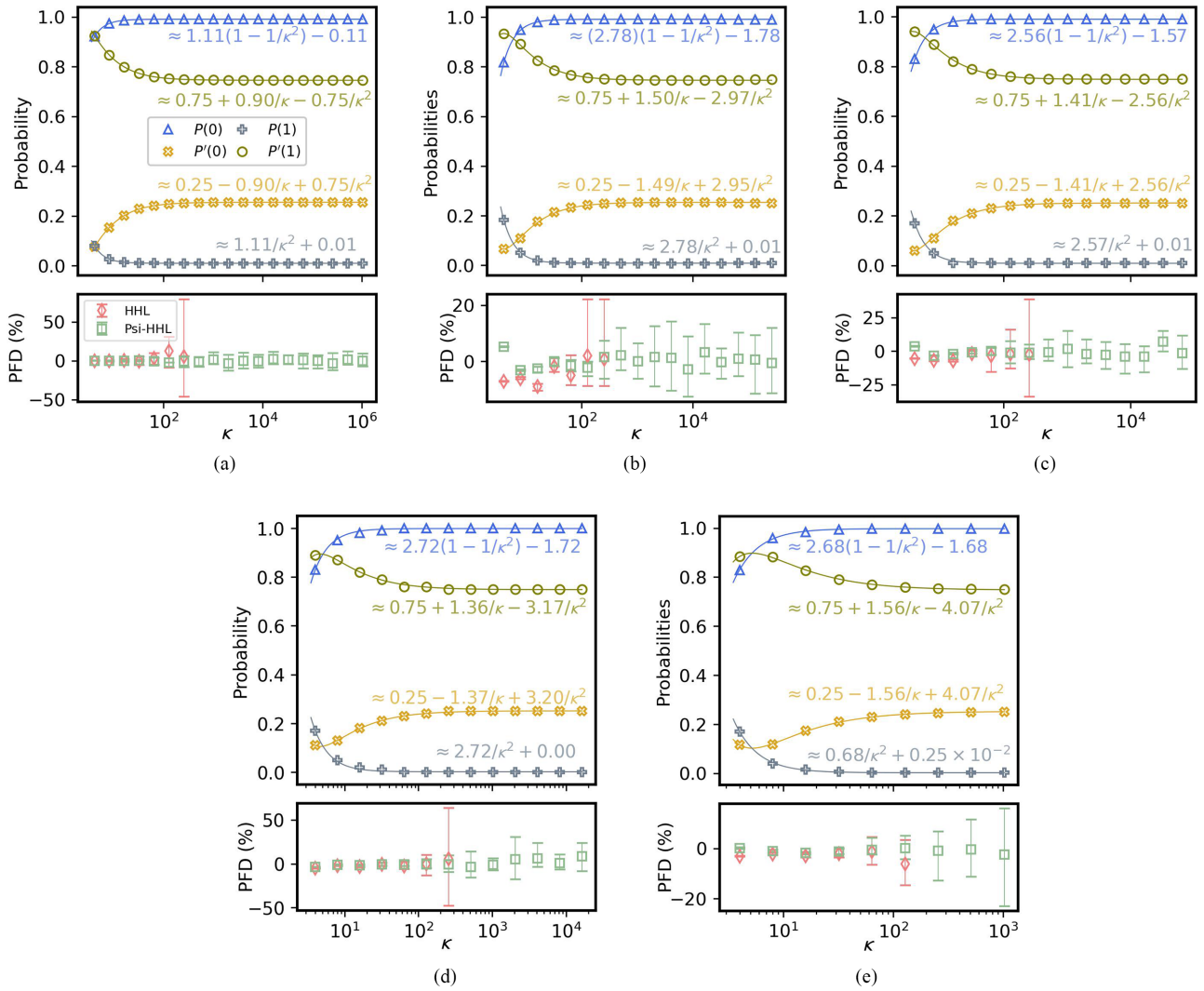


FIG. 7. Figure showing a comparison of the performance of HHL and Psi-HHL approaches for toy matrices. The top panels in each subfigure present the average probabilities of HHL and Psi-HHL with varying values of κ for different A matrix sizes: 4×4 (a), 8×8 (b), 16×16 (c), 32×32 (d), and 64×64 (e). The bottom panel of each subfigure represents the average percentage fraction differences (PFD) of the overlap E_c, calculated with HHL and Psi-HHL with respect to the classical value versus κ. Each data point results from 10 repeated runs of 10^6 shots. Also, all the computations have been carried out with A not diagonal and $\vec{b}$ in unequal superposition, as described in the main text. We also note here that the approximate equality is due to the fit coefficients in the figure being rounded off to two decimal places. For the Psi-HHL results, we set α to be 60°.

provided in Tables V and VI, respectively. For completeness, we also verify that the fit probabilities from Fig. 7 add to one (see Table VII of the Appendix).

We now comment on the observed PFDs from Fig. 7. We immediately see that HHL fails at some value of κ for the chosen number of shots (indicated by "nan" values in Tables I–VI of the Appendix). This is due to the fact that as $P(1)$ becomes very small, the fraction of the total number of shots that yield 1 upon measurement tend to very small values. Therefore, the number of shots available for the HOM module become too small to give any reasonable result beyond a certain value of κ. Our data also show that the error bars, in which the upper and lower points of the bars reflect the largest and the smallest PFD values obtained using HHL, increase as the condition number increases, until it reaches a critical value of κ, beyond which HHL fails. In contrast, we see that for Psi-HHL, even at $\kappa \approx 1 \times 10^6$, the length of the error bar is about 17%.

We finally comment on our results from Fig. 7 on the larger size matrices (8×8 through 64×64), where for Psi-HHL, we consider $\alpha = 60^\circ$. Figures 19–22 provide the data for 70° and 80° cases, with Fig. 19 also giving the information for 10^5 shots. Tables VIII–XI in the Appendix provide the accompanying data. We observe that, broadly, the trends are similar to what we find for the smaller 4×4 cases. Figure 23 of the Appendix summarizes the situations where HHL fails for all of the toy matrices considered, as a heat map. We find that for 1×10^6 shots, HHL starts returning nan values between κ of 2^8 and 2^{10}. In view of the computational cost involved, we did not go all the way up to a condition number of 2^{20} for matrices above 4×4 size, and we stopped much earlier for the 64×64 case.

We now turn our attention to Fig. 8, where we see that HHL does not fail upon increasing the number of shots, but the number requires to be about 1×10^9 in order to get a

TABLE I. Table presenting the data for HHL and Psi-HHL algorithms (with $\alpha = 60^\circ$) for 4×4 matrices, and in particular, for three cases: A diagonal and $\vec{b}$ in equal superposition (denoted in the table as "A diag, $\vec{b}$ equal"), A diagonal and $\vec{b}$ not in equal superposition (denoted in the table as "A diag, $\vec{b}$ unequal"), and A not diagonal and $\vec{b}$ in an unequal superposition (denoted in the table as "A not diag, $\vec{b}$ unequal"). The string "nan" refers to situations where we get the square root of a negative quantity for energy, which is unphysical, and hence is not a valid result. Each data point is generated by taking the average over 10 repetitions. "No. shots" refers to the number of shots, while "No. qubits" denotes the number of qubits.

			A diag, $\vec{b}$ equal		A diag, $\vec{b}$ unequal		A not diag, $\vec{b}$ unequal	
No. shots	$\approx \kappa$	No. qubits	PFD ($P(0)$, $P(1)$)	PFD ($P'(0)$, $P'(1)$)	PFD ($P(0)$, $P(1)$)	PFD ($P'(0)$, $P'(1)$)	PFD ($P(0)$, $P(1)$)	PFD ($P'(0)$, $P'(1)$)
	2^2	8	−0.04 (0.65, 0.35)	−0.22 (0.21, 0.79)	−0.25 (0.92, 0.08)	−0.10 (0.06, 0.94)	0.27 (0.92, 0.08)	−0.04 (0.08, 0.92)
	2^3	9	0.02 (0.72, 0.28)	−0.07 (0.27, 0.73)	0.27 (0.97, 0.03)	−0.32 (0.15, 0.85)	−0.32 (0.97, 0.03)	0.08 (0.15, 0.85)
	2^4	10	−0.19 (0.74, 0.26)	0.32 (0.32, 0.68)	0.37 (0.99, 0.01)	−0.69 (0.20, 0.80)	0.96 (0.99, 0.01)	0.26 (0.20, 0.80)
	2^5	11	−0.17 (0.75, 0.25)	−0.02 (0.35, 0.65)	−1.20 (0.99, 0.01)	2.85 (0.23, 0.77)	−3.65 (0.99, 0.01)	0.32 (0.22, 0.78)
	2^6	12	0.08 (0.75, 0.25)	0.05 (0.37, 0.63)	nan (0.99, 0.01)	1.66 (0.24, 0.76)	nan (0.99, 0.01)	−1.56 (0.24, 0.76)
	2^7	13	−0.05 (0.75, 0.25)	−0.45 (0.37, 0.63)	nan (0.99, 0.01)	1.91 (0.25, 0.75)	nan (0.99, 0.01)	−2.62 (0.25, 0.75)
	2^8	14	−0.85 (0.75, 0.25)	−0.01 (0.37, 0.63)	nan (0.99, 0.01)	−2.00 (0.25, 0.75)	nan (0.99, 0.01)	−3.87 (0.25, 0.75)
	2^9	15	−0.57 (0.75, 0.25)	−0.22 (0.37, 0.63)	nan (0.99, 0.01)	−7.50 (0.25, 0.75)	nan (0.99, 0.01)	8.02 (0.25, 0.75)
	2^{10}	16	0.28 (0.75, 0.25)	−0.26 (0.37, 0.63)	nan (0.99, 0.01)	−2.33 (0.25, 0.75)	nan (0.99, 0.01)	−7.77 (0.25, 0.75)
10^5	2^{11}	17	−0.20 (0.75, 0.25)	0.08 (0.37, 0.63)	nan (0.99, 0.01)	2.65 (0.25, 0.75)	nan (0.99, 0.01)	−0.55 (0.25, 0.75)
	2^{12}	18	0.24 (0.75, 0.25)	0.03 (0.37, 0.63)	nan (0.99, 0.01)	7.93 (0.25, 0.75)	nan (0.99, 0.01)	−2.41(0.25, 0.75)
	2^{13}	19	−0.08 (0.75, 0.25)	0.30 (0.38, 0.62)	nan (0.99, 0.01)	4.67 (0.25, 0.75)	nan (0.99, 0.01)	3.12 (0.25, 0.75)
	2^{14}	20	0.15 (0.75, 0.25)	0.41 (0.38, 0.62)	nan (0.99, 0.01)	9.11 (0.25, 0.75)	nan (0.99, 0.01)	−5.60 (0.25, 0.75)
	2^{15}	21	0.46 (0.75, 0.25)	0.13 (0.38, 0.62)	nan (0.99, 0.01)	9.42 (0.26, 0.74)	nan (0.99, 0.01)	−1.11 (0.25, 0.75)
	2^{16}	22	−0.17 (0.75, 0.25)	0.54 (0.38, 0.62)	nan (0.99, 0.01)	−0.25 (0.25, 0.75)	nan (0.99, 0.01)	2.43 (0.25, 0.75)
	2^{17}	23	0.83 (0.75, 0.25)	−0.03 (0.38, 0.62)	nan (0.99, 0.01)	−0.40 (0.26, 0.74)	nan (0.99, 0.01)	−7.87 (0.25, 0.75)
	2^{18}	24	−0.13 (0.75, 0.25)	0.26 (0.37, 0.63)	nan (0.99, 0.01)	−8.56 (0.26, 0.74)	nan (0.99, 0.01)	9.69 (0.26, 0.74)
	2^{19}	25	0.07 (0.75, 0.25)	0.19 (0.37, 0.63)	nan (0.99, 0.01)	6.91 (0.26, 0.74)	nan (0.99, 0.01)	1.06 (0.25, 0.75)
	2^{20}	26	0.02 (0.75, 0.25)	−0.58 (0.37, 0.63)	nan (0.99, 0.01)	0.30 (0.25, 0.75)	nan (0.99, 0.01)	6.15 (0.25, 0.75)
	2^2	8	−0.06 (0.65, 0.35)	0.00 (0.21, 0.79)	−0.02 (0.92, 0.08)	0.03 (0.08, 0.92)	0.00 (0.92, 0.08)	0.04 (0.08, 0.92)
	2^3	9	0.07 (0.72, 0.28)	−0.14 (0.27, 0.73)	−0.03 (0.97, 0.03)	−0.04 (0.15, 0.85)	−0.17 (0.97, 0.03)	0.00 (0.15, 0.85)
	2^4	10	−0.09 (0.74, 0.26)	−0.04 (0.31, 0.69)	0.23 (0.99, 0.01)	0.11 (0.20, 0.8)	0.49 (0.99, 0.01)	−0.15 (0.20, 0.80)
	2^5	11	0.13 (0.75, 0.25)	−0.06 (0.34, 0.66)	1.92 (0.99, 0.01)	0.16 (0.22, 0.78)	−0.74 (0.99, 0.01)	0.44 (0.22, 0.78)
	2^6	12	−0.03 (0.75, 0.25)	0.00 (0.36, 0.64)	0.61 (0.99, 0.01)	0.01 (0.24, 0.76)	3.28 (0.99, 0.01)	−0.70 (0.24, 0.76)
	2^7	13	−0.01 (0.75, 0.25)	0.20 (0.37, 0.63)	1.49 (0.99, 0.01)	−1.56 (0.25, 0.75)	12.53 (0.99, 0.01)	−0.11 (0.25, 0.75)
	2^8	14	−0.02 (0.75, 0.25)	−0.02 (0.37, 0.63)	23.43 (0.99, 0.01)	−0.04 (0.25, 0.75)	5.65 (0.99, 0.01)	−1.15 (0.25, 0.75)
	2^9	15	0.14 (0.75, 0.25)	0.06 (0.37, 0.63)	nan (0.99, 0.01)	2.82 (0.25, 0.75)	nan (0.99, 0.01)	2.26 (0.25, 0.75)
10^6	2^{10}	16	−0.14 (0.75, 0.25)	−0.04 (0.37, 0.63)	nan (0.99, 0.01)	−0.12 (0.25, 0.75)	nan (0.99, 0.01)	−0.59 (0.25, 0.75)
	2^{11}	17	−0.05 (0.75, 0.25)	−0.05 (0.37, 0.63)	nan (0.99, 0.01)	−1.49 (0.25, 0.75)	nan (0.99, 0.01)	1.41 (0.25, 0.75)
	2^{12}	18	0.05 (0.75, 0.25)	−0.20 (0.37, 0.63)	nan (0.99, 0.01)	0.11 (0.25, 0.75)	nan (0.99, 0.01)	1.26 (0.25, 0.75)
	2^{13}	19	−0.04 (0.75, 0.25)	0.01 (0.37, 0.63)	nan (0.99, 0.01)	0.13 (0.25, 0.75)	nan (0.99, 0.01)	−3.37 (0.25, 0.75)
	2^{14}	20	−0.04 (0.75, 0.25)	−0.00 (0.37, 0.63)	nan (0.99, 0.01)	−4.52 (0.25, 0.75)	nan (0.99, 0.01)	1.47 (0.25, 0.75)
	2^{15}	21	−0.02 (0.75, 0.25)	−0.05 (0.37, 0.63)	nan (0.99, 0.01)	−0.70 (0.25, 0.75)	nan (0.99, 0.01)	−0.79 (0.25, 0.75)
	2^{16}	22	−0.07 (0.75, 0.25)	0.12 (0.38, 0.63)	nan (0.99, 0.01)	1.57 (0.25, 0.75)	nan (0.99, 0.01)	0.84 (0.25, 0.75)
	2^{17}	23	0.06 (0.75, 0.25)	−0.15 (0.38, 0.63)	nan (0.99, 0.01)	−0.40 (0.25, 0.75)	nan (0.99, 0.01)	0.05 (0.25, 0.75)
	2^{18}	24	0.11 (0.25, 0.75)	0.00 (0.37, 0.63)	nan (0.99, 0.01)	−1.22 (0.25, 0.75)	nan (0.99, 0.01)	−3.58 (0.25, 0.75)
	2^{19}	25	0.09 (0.75, 0.25)	−0.03 (0.37, 0.63)	nan (0.99, 0.01)	0.78 (0.25, 0.75)	nan (0.99, 0.01)	1.41 (0.25, 0.75)
	2^{20}	26	0.16 (0.75, 0.25)	−0.19 (0.37, 0.63)	nan (0.99, 0.01)	−1.52 (0.25, 0.75)	nan (0.99, 0.01)	0.01 (0.25, 0.75)

comparable range of PFDs as Psi-HHL, while Psi-HHL only incurs 10×10^6 shots. In particular, HHL gives a maximum PFD of 1.51% and a minimum of −2.98% percent with 1×10^9 shots, whereas Psi-HHL gives a maximum and minimum PFD of 2.33% and −2.97%, respectively, with only 10×10^6 shots.

B. Quantum chemistry matrices

Quantum chemistry is regarded as one of the killer applications of quantum computing [21]. Therefore, it is interesting to consider the performance of Psi-HHL in this scenario. In particular, we consider quantum chemistry problems via the LCC approach [2].

We start with preliminary *qualitative* remarks on the suitability of HHL/Psi-HHL for carrying out LCC calculations, and to that end, discuss the growth of the A matrix dimension and κ with system size. This in turn requires us to define system size. Since our focus is to demonstrate the performance of Psi-HHL and not a deep dive into chemistry, we follow the following steps: (a) choosing a few simple diatomic closed-shell molecules in their ground state and in their equilibrium bond lengths, (b) picking a suitable single-particle basis, (c) deciding on the number of occupied orbitals, and (d)

TABLE II. Table providing the data for HHL and Psi-HHL algorithms (with $\alpha = 70^\circ$) for 4×4 matrices. The notations are the same as those used in Table I. Each data point is generated by taking the average over 10 repetitions.

			A diag, $\vec{b}$ equal		A diag, $\vec{b}$ unequal		A not diag, $\vec{b}$ unequal	
No. shots	$\approx \kappa$	No. qubits	PFD $(P(0), P(1))$	PFD $(P'(0), P'(1))$	PFD $(P(0), P(1))$	PFD $(P'(0), P'(1))$	PFD $(P(0), P(1))$	PFD $(P'(0), P'(1))$
	2^2	8	−0.04 (0.65, 0.35)	−0.24 (0.23, 0.77)	−0.25 (0.92, 0.08)	−0.03 (0.02, 0.98)	0.27 (0.92, 0.08)	0.58 (0.02, 0.98)
	2^3	9	0.02 (0.72, 0.28)	−0.28 (0.25, 0.75)	0.27 (0.97, 0.03)	0.14 (0.06, 0.94)	−0.32 (0.97, 0.03)	−0.41 (0.06, 0.94)
	2^4	10	−0.19 (0.74, 0.26)	0.51 (0.27, 0.73)	0.37 (0.99, 0.01)	−0.35 (0.12, 0.88)	0.96 (0.99, 0.01)	0.44 (0.09, 0.91)
	2^5	11	−0.17 (0.75, 0.25)	0.05 (0.29, 0.71)	−1.20 (0.99, 0.01)	−0.99 (0.10, 0.90)	−3.65 (0.99, 0.01)	1.17 (0.10, 0.90)
	2^6	12	0.08 (0.75, 0.25)	0.54 (0.30, 0.70)	nan (0.99, 0.01)	1.40 (0.12, 0.88)	nan (0.99, 0.01)	0.99 (0.11, 0.89)
	2^7	13	−0.05 (0.75, 0.25)	0.74 (0.30, 0.70)	nan (0.99, 0.01)	2.34 (0.12, 0.88)	nan (0.99, 0.01)	2.20 (0.02, 0.88)
	2^8	14	−0.85 (0.75, 0.25)	0.40 (0.30, 0.69)	nan (0.99, 0.01)	3.69 (0.12, 0.88)	nan (0.99, 0.01)	3.54 (0.02, 0.88)
	2^9	15	−0.57 (0.75, 0.25)	−0.31 (0.31, 0.69)	nan (0.99, 0.01)	−8.88 (0.12, 0.88)	nan (0.99, 0.01)	1.96 (0.02, 0.88)
	2^{10}	16	0.28 (0.75, 0.25)	0.02 (0.31, 0.69)	nan (0.99, 0.01)	7.45 (0.12, 0.88)	nan (0.99, 0.01)	4.93 (0.02, 0.88)
10^5	2^{11}	17	−0.20 (0.75, 0.25)	−0.30 (0.31, 0.69)	nan (0.99, 0.01)	4.81 (0.12, 0.88)	nan (0.99, 0.01)	−2.36 (0.02, 0.88)
	2^{12}	18	0.24 (0.75, 0.25)	0.48 (0.31, 0.69)	nan (0.99, 0.01)	−2.98 (0.12, 0.88)	nan (0.99, 0.01)	0.81 (0.02, 0.88)
	2^{13}	19	−0.08 (0.75, 0.25)	0.38 (0.31, 0.69)	nan (0.99, 0.01)	5.64 (0.12, 0.88)	nan (0.99, 0.01)	−2.22 (0.02, 0.88)
	2^{14}	20	0.15 (0.75, 0.25)	0.15 (0.31, 0.69)	nan (0.99, 0.01)	10.48 (0.12, 0.88)	nan (0.99, 0.01)	0.33 (0.02, 0.88)
	2^{15}	21	0.46 (0.75, 0.25)	1.26 (0.31, 0.69)	nan (0.99, 0.01)	9.59 (0.12, 0.88)	nan (0.99, 0.01)	6.98 (0.02, 0.88)
	2^{16}	22	−0.17 (0.75, 0.25)	−0.34 (0.31, 0.69)	nan (0.99, 0.01)	5.62 (0.12, 0.88)	nan (0.99, 0.01)	−17.07 (0.02, 0.88)
	2^{17}	23	0.83 (0.75, 0.25)	1.31 (0.31, 0.69)	nan (0.99, 0.01)	5.56 (0.12, 0.88)	nan (0.99, 0.01)	2.02 (0.02, 0.88)
	2^{18}	24	−0.13 (0.75, 0.25)	0.00 (0.69, 0.31)	nan (0.99, 0.01)	0.00 (0.12, 0.88)	nan (0.99, 0.01)	18.88 (0.13, 0.87)
	2^{19}	25	0.07 (0.75, 0.25)	0.33 (0.31, 0.69)	nan (0.99, 0.01)	0.33 (0.12, 0.88)	nan (0.99, 0.01)	6.42 (0.12, 0.88)
	2^{20}	26	0.02 (0.75, 0.25)	−0.27 (0.31, 0.69)	nan (0.99, 0.01)	−6.81 (0.12, 0.88)	nan (0.99, 0.01)	6.75 (0.12, 0.88)
	2^2	8	−0.06 (0.64, 0.36)	−0.01 (0.23, 0.77)	−0.02 (0.92, 0.08)	−0.02 (0.02, 0.98)	0.00 (0.92, 0.08)	−0.01 (0.02, 0.98)
	2^3	9	−0.07 (0.72, 0.28)	−0.16 (0.22, 0.76)	−0.03 (0.97, 0.03)	0.04 (0.06, 0.94)	−0.17 (0.97, 0.03)	0.00 (0.06, 0.94)
	2^4	10	−0.09 (0.74, 0.26)	−0.05 (0.27, 0.73)	0.23 (0.99, 0.01)	−0.26 (0.09, 0.91)	0.49 (0.99, 0.01)	−0.27 (0.09, 0.91)
	2^5	11	0.13 (0.75, 0.25)	−0.08 (0.29, 0.71)	1.92 (0.99, 0.01)	−0.26 (0.10, 0.90)	−0.74 (0.99, 0.01)	0.50 (0.11, 0.89)
	2^6	12	−0.03 (0.75, 0.25)	0.02 (0.30, 0.70)	0.61 (0.99, 0.01)	1.32 (0.11, 0.89)	3.28 (0.99, 0.01)	−0.27 (0.12, 0.88)
	2^7	13	−0.01 (0.75, 0.25)	−0.07 (0.31, 0.69)	1.49 (0.99, 0.01)	−0.24 (0.12, 0.88)	12.53 (0.99, 0.01)	0.40 (0.12, 0.88)
	2^8	14	−0.02 (0.75, 0.25)	0.12 (0.31, 0.69)	23.43 (0.99, 0.01)	0.43 (0.12, 0.88)	5.65 (0.99, 0.01)	1.91 (0.12, 0.88)
	2^9	15	0.14 (0.75, 0.25)	0.19 (0.31, 0.69)	nan (0.99, 0.01)	−1.81 (0.12, 0.88)	nan (0.99, 0.01)	1.12 (0.12, 0.88)
	2^{10}	16	−0.14 (0.75, 0.25)	−0.26 (0.31, 0.69)	nan (0.99, 0.01)	1.19 (0.12, 0.88)	nan (0.99, 0.01)	−2.59 (0.12, 0.88)
10^6	2^{11}	17	−0.05 (0.75, 0.25)	0.04 (0.31, 0.69)	nan (0.99, 0.01)	−1.68 (0.12, 0.88)	nan (0.99, 0.01)	−0.85 (0.12, 0.88)
	2^{12}	18	0.05 (0.75, 0.25)	−0.44 (0.31, 0.69)	nan (0.99, 0.01)	2.36 (0.12, 0.88)	nan (0.99, 0.01)	−5.96 (0.12, 0.88)
	2^{13}	19	−0.03 (0.75, 0.25)	0.15 (0.31, 0.69)	nan (0.99, 0.01)	5.19 (0.12, 0.88)	nan (0.99, 0.01)	1.52 (0.12, 0.88)
	2^{14}	20	−0.03 (0.75, 0.25)	0.25 (0.31, 0.69)	nan (0.99, 0.01)	2.50 (0.12, 0.88)	nan (0.99, 0.01)	−1.89 (0.12, 0.88)
	2^{15}	21	−0.02 (0.75, 0.25)	−0.33 (0.31, 0.69)	nan (0.99, 0.01)	0.41 (0.12, 0.88)	nan (0.99, 0.01)	−3.65 (0.12, 0.88)
	2^{16}	22	−0.07 (0.75, 0.25)	−0.01 (0.31, 0.69)	nan (0.99, 0.01)	−3.09 (0.12, 0.88)	nan (0.99, 0.01)	−1.88 (0.12, 0.88)
	2^{17}	23	0.06 (0.75, 0.25)	−0.07 (0.31, 0.69)	nan (0.99, 0.01)	2.54 (0.12, 0.88)	nan (0.99, 0.01)	−0.92 (0.12, 0.88)
	2^{18}	24	0.11 (0.75, 0.25)	0.07 (0.31, 0.69)	nan (0.99, 0.01)	−0.47 (0.88, 0.12)	nan (0.99, 0.01)	−0.46 (0.88, 0.12)
	2^{19}	25	0.08 (0.75, 0.25)	0.09 (0.31, 0.69)	nan (0.99, 0.01)	1.81 (0.12, 0.88)	nan (0.99, 0.01)	−0.89 (0.12, 0.88)
	2^{20}	26	0.16 (0.75, 0.25)	−0.02 (0.31, 0.69)	nan (0.99, 0.01)	−2.00 (0.12, 0.88)	nan (0.99, 0.01)	3.65 (0.12, 0.88)

systematically increasing the number of unoccupied orbitals (virtuals) for system size. We choose four representative molecules: the light Li_2, the moderately heavy KH and RbH, and the heavy CsH, all in their equilibrium bond lengths (Li_2: 5.0600 bohrs, KH: 4.2300 bohrs, RbH: 4.4726 bohrs, and CsH: 4.7135 bohrs) [22,23]. The adjectives "light" and "heavy" refer to the atomic number of the heavier atom in a diatomic molecule. We pick the Sapporo double-zeta basis sets for KH, RbH, and CsH (K, Rb, and Cs: Sapporo-DKH3-DZP-2012, and H: Sapporo-DZP) [24], while for Li_2, we choose the STO-6G basis [25]. We employ the C_{2v} point-group symmetry for KH, RbH, and CsH computations, while for the case of Li_2, we pick the D_{2h} symmetry. We do not include relativistic effects as our aim is to only compare HHL and Psi-HHL and not account for as many relevant physical effects as possible. We now proceed to discuss the dimension of the A matrix and the condition number scaling in LCC for these chosen molecules.

1. Dimension of the A matrix

Since the LCC matrix is not guaranteed to be of dimension $2^N \times 2^N \equiv n \times n$, we make a distinction between the dimension of the LCC matrix, A_{mol}, which is $m \times m$, and the dimension of the associated A matrix, $n \times n$. We go from A_{mol} to A via padding, which we explain in Appendix D. We note that m, which we shall hereafter think of as the system size, is the number of particle-hole excitations that one considers for an LCC calculation, which in turn is decided by choice of single-particle basis and active space size. We denote the number of occupied orbitals as n_o and virtuals by n_v. The number of rows (or columns) of the A_{mol} matrix grows as $\sim n_o^{\mathcal{E}} n_v^{\mathcal{E}}$

TABLE III. Table providing the data for HHL and Psi-HHL algorithms (with $\alpha = 80^\circ$) for 4×4 matrices. The notations are the same as those used in Tables I and II. Each data point is generated by taking the average over 10 repetitions.

			A diag, $\vec{b}$ equal		A diag, $\vec{b}$ unequal		A not diag, $\vec{b}$ unequal	
No. shots	$\approx \kappa$	No. qubits	PFD ($P(0)$, $P(1)$)	PFD ($P'(0)$, $P'(1)$)	PFD ($P(0)$, $P(1)$)	PFD ($P'(0)$, $P'(1)$)	PFD ($P(0)$, $P(1)$)	PFD ($P'(0)$, $P'(1)$)
	2^2	8	−0.04 (0.65, 0.35)	0.43 (0.21, 0.79)	−0.25 (0.92, 0.08)	0.06 (0.01, 0.99)	0.27 (0.92, 0.08)	0.31 (0.02, 0.98)
	2^3	9	0.02 (0.72, 0.28)	0.29 (0.27, 0.73)	0.27 (0.97, 0.03)	−0.59 (0.02, 0.98)	−0.32 (0.97, 0.03)	−0.92 (0.02, 0.98)
	2^4	10	−0.19 (0.74, 0.26)	2.47 (0.32, 0.68)	0.37 (0.99, 0.01)	2.59 (0.02, 0.98)	0.96 (0.99, 0.01)	1.55 (0.02, 0.98)
	2^5	11	−0.17 (0.75, 0.25)	0.67 (0.35, 0.65)	−1.20 (0.99, 0.01)	1.63 (0.03, 0.97)	−3.65 (0.99, 0.01)	1.89 (0.03, 0.97)
	2^6	12	0.08 (0.75, 0.25)	−0.17 (0.36, 0.64)	nan (0.99, 0.01)	5.34 (0.04, 0.96)	nan (0.99, 0.01)	−4.59 (0.03, 0.97)
	2^7	13	−0.05 (0.75, 0.25)	−0.30 (0.37, 0.63)	nan (0.99, 0.01)	0.55 (0.04, 0.96)	nan (0.99, 0.01)	0.37 (0.04, 0.96)
	2^8	14	−0.85 (0.75, 0.25)	−2.17 (0.37, 0.63)	nan (0.99, 0.01)	6.89 (0.04, 0.96)	nan (0.99, 0.01)	0.46 (0.04, 0.96)
	2^9	15	−0.57 (0.75, 0.25)	0.04 (0.37, 0.63)	nan (0.99, 0.01)	−2.64 (0.04, 0.96)	nan (0.99, 0.01)	4.65 (0.04, 0.96)
	2^{10}	16	0.28 (0.75, 0.25)	1.01 (0.37, 0.63)	nan (0.99, 0.01)	3.21 (0.04, 0.96)	nan (0.99, 0.01)	−4.06 (0.04, 0.96)
10^5	2^{11}	17	−0.20 (0.75, 0.25)	−0.20 (0.37, 0.63)	nan (0.99, 0.01)	−5.46 (0.04, 0.96)	nan (0.99, 0.01)	−0.93 (0.04, 0.96)
	2^{12}	18	0.24 (0.75, 0.25)	−0.55 (0.37, 0.63)	nan (0.99, 0.01)	−4.80 (0.04, 0.96)	nan (0.99, 0.01)	9.42 (0.04, 0.96)
	2^{13}	19	−0.08 (0.75, 0.25)	−0.17 (0.37, 0.63)	nan (0.99, 0.01)	2.18 (0.04, 0.96)	nan (0.99, 0.01)	7.83 (0.04, 0.96)
	2^{14}	20	0.15 (0.75, 0.25)	0.56 (0.37, 0.63)	nan (0.99, 0.01)	5.32 (0.04, 0.96)	nan (0.99, 0.01)	−0.86 (0.04, 0.96)
	2^{15}	21	0.46 (0.75, 0.25)	−0.11 (0.37, 0.63)	nan (0.99, 0.01)	5.89 (0.04, 0.96)	nan (0.99, 0.01)	3.92 (0.04, 0.96)
	2^{16}	22	−0.17 (0.75, 0.25)	0.24 (0.37, 0.63)	nan (0.99, 0.01)	−12.26 (0.04, 0.96)	nan (0.99, 0.01)	9.60 (0.04, 0.96)
	2^{17}	23	0.83 (0.75, 0.25)	−0.94 (0.37, 0.63)	nan (0.99, 0.01)	−2.94 (0.04, 0.96)	nan (0.99, 0.01)	−5.61 (0.04, 0.96)
	2^{18}	24	−0.13 (0.75, 0.25)	−1.64 (0.26, 0.74)	nan (0.99, 0.01)	−0.60 (0.04, 0.96)	nan (0.99, 0.01)	5.92 (0.04, 0.96)
	2^{19}	25	0.07 (0.75, 0.25)	1.47 (0.27, 0.73)	nan (0.99, 0.01)	−0.60 (0.04, 0.96)	nan (0.99, 0.01)	−4.92 (0.04, 0.96)
	2^{20}	26	0.02 (0.75, 0.25)	−1.70 (0.26, 0.74)	nan (0.99, 0.01)	−17.20 (0.04, 0.96)	nan (0.99, 0.01)	5.03 (0.04, 0.96)
	2^2	8	−0.06 (0.64, 0.36)	−0.13 (0.28, 0.72)	−0.02 (0.92, 0.08)	0.00 (0.02, 0.98)	0.00 (0.92, 0.08)	0.03 (0.02, 0.98)
	2^3	9	−0.07 (0.72, 0.28)	0.14 (0.24, 0.76)	−0.03 (0.97, 0.03)	−0.19 (0.01, 0.99)	−0.17 (0.97, 0.03)	−0.06 (0.01, 0.99)
	2^4	10	−0.09 (0.74, 0.26)	−0.03 (0.25, 0.75)	0.23 (0.99, 0.01)	−0.22 (0.02, 0.98)	0.49 (0.99, 0.01)	−0.02 (0.02, 0.98)
	2^5	11	0.13 (0.75, 0.25)	0.64 (0.26, 0.74)	1.92 (0.99, 0.01)	0.03 (0.03, 0.97)	−0.74 (0.99, 0.01)	1.11 (0.03, 0.97)
	2^6	12	−0.04 (0.75, 0.25)	−0.05 (0.26, 0.74)	0.61 (0.99, 0.01)	1.21 (0.04, 0.96)	3.28 (0.99, 0.01)	0.68 (0.03, 0.97)
	2^7	13	−0.01 (0.75, 0.25)	0.17 (0.26, 0.74)	1.49 (0.99, 0.01)	−1.22 (0.04, 0.96)	12.53 (0.99, 0.01)	0.24 (0.03, 0.97)
	2^8	14	−0.02 (0.75, 0.25)	−0.17 (0.26, 0.74)	23.43 (0.99, 0.01)	−3.19 (0.04, 0.96)	5.65 (0.99, 0.01)	0.32 (0.04, 0.96)
	2^9	15	0.14 (0.75, 0.25)	−0.50 (0.26, 0.74)	nan (0.99, 0.01)	−2.13 (0.04, 0.96)	nan (0.99, 0.01)	−2.48 (0.04, 0.96)
10^6	2^{10}	16	−0.14 (0.75, 0.25)	−0.30 (0.26, 0.74)	nan (0.99, 0.01)	−0.59 (0.04, 0.96)	nan (0.99, 0.01)	−0.24 (0.04, 0.96)
	2^{11}	17	−0.05 (0.75, 0.25)	0.47 (0.26, 0.74)	nan (0.99, 0.01)	−2.93 (0.04, 0.96)	nan (0.99, 0.01)	0.05 (0.04, 0.96)
	2^{12}	18	0.06 (0.75, 0.25)	0.40 (0.26, 0.74)	nan (0.99, 0.01)	0.62 (0.04, 0.96)	nan (0.99, 0.01)	−2.73 (0.04, 0.96)
	2^{13}	19	−0.03 (0.75, 0.25)	0.14 (0.26, 0.74)	nan (0.99, 0.01)	0.12 (0.04, 0.96)	nan (0.99, 0.01)	6.03 (0.04, 0.96)
	2^{14}	20	−0.03 (0.75, 0.25)	0.62 (0.26, 0.74)	nan (0.99, 0.01)	2.52 (0.04, 0.96)	nan (0.99, 0.01)	0.28 (0.04, 0.96)
	2^{15}	21	−0.02 (0.75, 0.25)	−0.34 (0.26, 0.74)	nan (0.99, 0.01)	1.03 (0.04, 0.96)	nan (0.99, 0.01)	−6.30 (0.04, 0.96)
	2^{16}	22	−0.07 (0.75, 0.25)	−0.59 (0.26, 0.74)	nan (0.99, 0.01)	−3.21 (0.04, 0.96)	nan (0.99, 0.01)	−2.40 (0.04, 0.96)
	2^{17}	23	0.06 (0.75, 0.25)	0.49 (0.26, 0.74)	nan (0.99, 0.01)	0.45 (0.04, 0.96)	nan (0.99, 0.01)	2.72 (0.04, 0.96)
	2^{18}	24	0.11 (0.75, 0.25)	0.14 (0.27, 0.73)	nan (0.99, 0.01)	−2.46 (0.04, 0.96)	nan (0.99, 0.01)	−1.52 (0.04, 0.96)
	2^{19}	25	0.08 (0.75, 0.25)	0.01 (0.27, 0.73)	nan (0.99, 0.01)	−1.95 (0.04, 0.96)	nan (0.99, 0.01)	−0.72 (0.04, 0.96)
	2^{20}	26	0.16 (0.75, 0.25)	−0.33 (0.27, 0.73)	nan (0.99, 0.01)	−2.07 (0.04, 0.96)	nan (0.99, 0.01)	−2.46 (0.04, 0.96)

(the number of orbitals are kept fixed), which is exponential. $\mathcal{E}$ refers to the excitation rank. For example, $\mathcal{E} = 2$ is the LCCSD approximation, where S stands for single excitations and D for double excitations. For a given $\mathcal{E}$, as we increase the number of orbitals, the system size m grows *further* polynomially (for example, see Fig. 24 in the Appendix). For the purposes of this work, we fix n_o and increase n_v for a given molecule, all within the LCCSD approximation. The technical details involved in the generation of A matrix as well as the $\vec{b}$ vector for our computations are discussed in Appendix A 2.

2. Condition number scaling in LCC

Although HHL offers an exponential advantage in terms of system size, it is important to check if for the LCCSD problem, the condition number itself scales favorably with system size m for the molecules that we consider. We point out towards the end of Appendix A 2 that it is sufficient to analyze κ versus m; this curve upper bounds κ versus n. We increase the size of the active space (via n_v), and thus m in a systematic manner, by carrying out an orbital character analysis whose details we explain in Appendix A 2 and also accompanying Table XII. Furthermore, for this analysis, we consider KH, RbH, and CsH, but not Li_2, as the system is too small (in the STO-6G basis) to carry out a κ versus m analysis. We start with (n_o, n_v) of (6, 6), (8, 8), and (10, 10) for all the three molecules, and for each of these cases, we systematically increase n_v. Figure 9 presents our results. We see that the condition number varies as a polylogarithmic function of system size. This behavior is also consistent with

TABLE IV. Table presenting the data for HHL and Psi-HHL algorithms (with $\alpha = 60^\circ$) for 4×4 matrices, and in particular, for three cases: A diagonal and $\vec{b}$ in equal superposition (denoted in the table as "A diag, $\vec{b}$ equal"), A diagonal and $\vec{b}$ not in equal superposition (denoted in the table as "A diag, $\vec{b}$ unequal"), and A not diagonal and $\vec{b}$ in an unequal superposition (denoted in the table as "A not diag, $\vec{b}$ unequal"). The string "nan" refers to situations where we get the square root of a negative quantity for energy, which is unphysical, and hence is not a valid result. Each data point is generated by taking the average over 50 repetitions.

			A diag $\vec{b}$ equal		A diag $\vec{b}$ unequal		A not diag $\vec{b}$ unequal	
No. shots	$\approx \kappa$	No. qubits	PFD ($P(0)$, $P(1)$)	PFD ($P'(0)$, $P'(1)$)	PFD ($P(0)$, $P(1)$)	PFD ($P'(0)$, $P'(1)$)	PFD ($P(0)$, $P(1)$)	PFD ($P'(0)$, $P'(1)$)
	2^2	8	−0.08 (0.64, 0.36)	0.01 (0.21, 0.79)	0.03 (0.92, 0.08)	−0.11 (0.08, 0.92)	0.07 (0.92, 0.08)	0.01 (0.08, 0.92)
	2^3	9	0.01 (0.72, 0.28)	−0.17 (0.27, 0.73)	−0.05 (0.97, 0.03)	−0.09 (0.15, 0.85)	−0.02 (0.97, 0.03)	−0.05 (0.15, 0.85)
	2^4	10	−0.01 (0.74, 0.26)	0.06 (0.32, 0.68)	0.31 (0.99, 0.01)	0.47 (0.20, 0.80)	0.48 (0.99, 0.01)	0.39 (0.20, 0.80)
	2^5	11	−0.06 (0.75, 0.25)	−0.14 (0.35, 0.65)	1.85 (0.99, 0.01)	−0.04 (0.23, 0.77)	−0.10 (0.99, 0.01)	−0.15 (0.22, 0.78)
	2^6	12	0.08 (0.75, 0.25)	−0.38 (0.37, 0.63)	nan (0.99, 0.01)	−1.41 (0.24, 0.76)	nan (0.99, 0.01)	−1.75 (0.24, 0.76)
	2^7	13	0.00 (0.75, 0.25)	0.10 (0.37, 0.63)	nan (0.99, 0.01)	1.39 (0.25, 0.75)	nan (0.99, 0.01)	1.85 (0.25, 0.75)
	2^8	14	0.14 (0.75, 0.25)	−0.10 (0.37, 0.63)	nan (0.99, 0.01)	0.42 (0.25, 0.75)	nan (0.99, 0.01)	1.92 (0.25, 0.75)
	2^9	15	0.12 (0.75, 0.25)	0.14 (0.37, 0.63)	nan (0.99, 0.01)	3.21 (0.25, 0.75)	nan (0.99, 0.01)	−1.05 (0.25, 0.75)
10^5	2^{10}	16	−0.01 (0.75, 0.25)	−0.08 (0.37, 0.63)	nan (0.99, 0.01)	0.87 (0.25, 0.75)	nan (0.99, 0.01)	1.00 (0.25, 0.75)
	2^{11}	17	−0.05 (0.75, 0.25)	−0.28 (0.37, 0.63)	nan (0.99, 0.01)	−0.23 (0.25, 0.75)	nan (0.99, 0.01)	2.19 (0.25, 0.75)
	2^{12}	18	0.02 (0.75, 0.25)	−0.03 (0.37, 0.63)	nan (0.99, 0.01)	1.38 (0.25, 0.75)	nan (0.99, 0.01)	0.96 (0.25, 0.75)
	2^{13}	19	0.09 (0.75, 0.25)	−0.38 (0.38, 0.62)	nan (0.99, 0.01)	−0.59 (0.25, 0.75)	nan (0.99, 0.01)	−2.71 (0.25, 0.75)
	2^{14}	20	0.27 (0.75, 0.25)	0.03 (0.38, 0.62)	nan (0.99, 0.01)	2.97 (0.25, 0.75)	nan (0.99, 0.01)	−0.36 (0.25, 0.75)
	2^{15}	21	0.21 (0.75, 0.25)	−0.09 (0.38, 0.62)	nan (0.99, 0.01)	−3.51 (0.26, 0.74)	nan (0.99, 0.01)	2.68 (0.25, 0.75)
	2^{16}	22	−0.11 (0.75, 0.25)	0.05 (0.38, 0.62)	nan (0.99, 0.01)	−1.74 (0.25, 0.75)	nan (0.99, 0.01)	1.15 (0.25, 0.75)
	2^{17}	23	0.29 (0.75, 0.25)	0.05 (0.38, 0.62)	nan (0.99, 0.01)	3.06 (0.26, 0.74)	nan (0.99, 0.01)	2.17 (0.25, 0.75)
	2^2	8	0.00 (0.64, 0.36)	0.05 (0.21, 0.79)	0.03 (0.92, 0.08)	0.02 (0.08, 0.92)	0.05 (0.92, 0.08)	−0.03 (0.08, 0.92)
	2^3	9	0.00 (0.72, 0.28)	−0.05 (0.27, 0.73)	0.02 (0.97, 0.03)	0.00 (0.15, 0.85)	−0.08 (0.97, 0.03)	0.01 (0.15, 0.85)
	2^4	10	0.00 (0.74, 0.26)	0.04 (0.27, 0.73)	−0.07 (0.99, 0.01)	−0.10 (0.20, 0.8)	0.12 (0.99, 0.01)	0.14 (0.20, 0.80)
	2^5	11	0.06 (0.75, 0.25)	−0.02 (0.31, 0.69)	0.12 (0.99, 0.01)	0.07 (0.22, 0.78)	0.16 (0.99, 0.01)	0.37 (0.22, 0.78)
	2^6	12	0.06 (0.75, 0.25)	0.05 (0.34, 0.66)	0.99 (0.99, 0.01)	0.29 (0.24, 0.76)	0.02 (0.99, 0.01)	−0.03 (0.24, 0.76)
	2^7	13	0.10 (0.75, 0.25)	−0.03 (0.36, 0.64)	1.36 (0.99, 0.01)	0.17 (0.25, 0.75)	2.19 (0.99, 0.01)	0.50 (0.25, 0.75)
	2^8	14	−0.07 (0.75, 0.25)	0.07 (0.37, 0.63)	8.58 (0.99, 0.01)	−0.03 (0.25, 0.75)	3.63 (0.99, 0.01)	−1.34 (0.25, 0.75)
10^6	2^9	15	0.04 (0.75, 0.25)	0.04 (0.37, 0.63)	nan (0.99, 0.01)	−0.05 (0.25, 0.75)	nan (0.99, 0.01)	0.25 (0.25, 0.75)
	2^{10}	16	−0.14 (0.75, 0.25)	0.05 (0.37, 0.63)	nan (0.99, 0.01)	−0.25 (0.25, 0.75)	nan (0.99, 0.01)	0.71 (0.25, 0.75)
	2^{11}	17	−0.09 (0.75, 0.25)	0.10 (0.37, 0.63)	nan (0.99, 0.01)	−0.03 (0.25, 0.75)	nan (0.99, 0.01)	−0.31 (0.25, 0.75)
	2^{12}	18	−0.03 (0.75, 0.25)	0.06 (0.37, 0.63)	nan (0.99, 0.01)	0.78 (0.25, 0.75)	nan (0.99, 0.01)	−0.82 (0.25, 0.75)
	2^{13}	19	0.04 (0.75, 0.25)	−0.02 (0.37, 0.63)	nan (0.99, 0.01)	0.75 (0.25, 0.75)	nan (0.99, 0.01)	−0.87 (0.25, 0.75)
	2^{14}	20	−0.12 (0.75, 0.25)	0.09 (0.37, 0.63)	nan (0.99, 0.01)	0.07 (0.25, 0.75)	nan (0.99, 0.01)	−0.05 (0.25, 0.75)
	2^{15}	21	0.02 (0.75, 0.25)	−0.01 (0.37, 0.63)	nan (0.99, 0.01)	1.00 (0.25, 0.75)	nan (0.99, 0.01)	0.14 (0.25, 0.75)
	2^{16}	22	0.09 (0.75, 0.25)	0.02 (0.37, 0.63)	nan (0.99, 0.01)	−0.09 (0.25, 0.75)	nan (0.99, 0.01)	0.21 (0.25, 0.75)
	2^{17}	23	0.02 (0.75, 0.25)	−0.01 (0.37, 0.63)	nan (0.99, 0.01)	−0.66 (0.25, 0.75)	nan (0.99, 0.01)	0.45 (0.25, 0.75)

what one may expect from chemistry intuition: we begin by referring the reader to Table XIII of the Appendix, where we list the largest and smallest eigenvalues of the A matrix for each value of m, for KH, RbH, and CsH. The data show that the increase in κ as we add virtual orbitals is driven by the decrease of the lowest eigenvalue of the A matrix. We note that every matrix element of the A matrix can be expressed as $\langle \Phi_p | H | \Phi_q \rangle$, where H is the Hamiltonian and $|\Phi_p\rangle$ and $|\Phi_q\rangle$ are the excited determinants built from particle-hole excitations arising from the Hartree-Fock (HF) configuration. The smallest eigenvalue of the sparse and diagonally dominant A matrix, which we saw as being important in determining the growth of κ, can be qualitatively thought of as corresponding to the energy of the first excited state (assuming that the wave function of the first excited state has small contribution from the HF configuration). Thus, we expect that the decrease in the lowest eigenvalue of A saturates as we keep adding virtual orbitals and, eventually, the lowest eigenvalue of the A matrix will converge to a certain value. Thus, the increase of κ saturates too, thus leading one to expect that the condition number would vary as a polylogarithmic function of system size.

We also observe in each subfigure (that is, for a fixed number of occupied orbitals) that for large m, the condition number of KH is the largest, followed by RbH, and then CsH. This trend can be explained qualitatively using chemical intuition, by looking at the considered orbitals for the (6, 6) case as a representative example. Recalling that each eigenvalue of A can be thought of as an excited state energy, the highest excited state arises from electron excitations from the lowest occupied orbitals, which are $2p$ and $3d$ for KH and RbH cases, respectively. It is clear that $2p$ of K has much lower orbital energy than the $3d$ orbital of Rb. Thus, we can expect that the $2p \longrightarrow$ virtual excitation in KH has a higher excitation energy associated with it than the 3d $\longrightarrow$ virtual excitation in RbH. Similarly, we can expect that the $4d \longrightarrow$ virtual excited state of CsH is lower in energy than the $3d \longrightarrow$ virtual excited state of RbH. In summary, we can expect that

TABLE V. Table providing the data for HHL and Psi-HHL algorithms (with $\alpha = 70^\circ$) for 4×4 matrices. The notations are the same as those used in Table IV. Each data point is generated by taking the average over 50 repetitions.

			A diag $\vec{b}$ equal		A diag $\vec{b}$ unequal		A not diag $\vec{b}$ unequal	
No. shots	$\approx \kappa$	No. qubits	PFD $(P(0), P(1))$	PFD $(P'(0), P'(1))$	PFD $(P(0), P(1))$	PFD $(P'(0), P'(1))$	PFD $(P(0), P(1))$	PFD $(P'(0), P'(1))$
	2^2	8	−0.08 (0.64, 0.36)	−0.03 (0.23, 0.77)	0.03 (0.92, 0.08)	−0.09 (0.02, 0.98)	0.07 (0.92, 0.08)	−0.05 (0.02, 0.98)
	2^3	9	0.01 (0.72, 0.28)	−0.17 (0.24, 0.76)	−0.05 (0.97, 0.03)	0.12 (0.06, 0.94)	−0.02 (0.97, 0.03)	−0.22 (0.06, 0.94)
	2^4	10	−0.02 (0.74, 0.26)	−0.26 (0.27, 0.73)	0.31 (0.99, 0.01)	−0.48 (0.12, 0.88)	0.48 (0.99, 0.01)	−0.17 (0.09, 0.91)
	2^5	11	−0.06 (0.75, 0.25)	0.07 (0.29, 0.71)	1.85 (0.99, 0.01)	0.70 (0.10, 0.90)	−0.10 (0.99, 0.01)	−0.68 (0.10, 0.90)
	2^6	12	0.09 (0.75, 0.25)	0.23 (0.30, 0.70)	nan (0.99, 0.01)	−0.55 (0.12, 0.88)	nan (0.99, 0.01)	0.18 (0.11, 0.89)
	2^7	13	−0.01 (0.75, 0.25)	0.28 (0.30, 0.70)	nan (0.99, 0.01)	0.74 (0.12, 0.88)	nan (0.99, 0.01)	1.88 (0.11, 0.88)
	2^8	14	0.15 (0.75, 0.25)	−0.09 (0.30, 0.69)	nan (0.99, 0.01)	2.95 (0.12, 0.88)	nan (0.99, 0.01)	−1.04 (0.12, 0.88)
10^5	2^9	15	0.12 (0.75, 0.25)	0.57 (0.31, 0.69)	nan (0.99, 0.01)	0.33 (0.12, 0.88)	nan (0.99, 0.01)	2.59 (0.12, 0.88)
	2^{10}	16	−0.01 (0.75, 0.25)	−0.03 (0.31, 0.69)	nan (0.99, 0.01)	−0.69 (0.12, 0.88)	nan (0.99, 0.01)	1.22 (0.12, 0.88)
	2^{11}	17	−0.05 (0.75, 0.25)	−0.51 (0.31, 0.69)	nan (0.99, 0.01)	1.78 (0.12, 0.88)	nan (0.99, 0.01)	−1.75 (0.12, 0.88)
	2^{12}	18	0.02 (0.75, 0.25)	0.06 (0.31, 0.69)	nan (0.99, 0.01)	4.37 (0.12, 0.88)	nan (0.99, 0.01)	−0.00 (0.12, 0.88)
	2^{13}	19	0.10 (0.75, 0.25)	−0.38 (0.31, 0.69)	nan (0.99, 0.01)	−2.56 (0.12, 0.88)	nan (0.99, 0.01)	−0.03 (0.12, 0.88)
	2^{14}	20	0.28 (0.75, 0.25)	0.14 (0.31, 0.69)	nan (0.99, 0.01)	2.95 (0.12, 0.88)	nan (0.99, 0.01)	−3.04 (0.12, 0.88)
	2^{15}	21	0.21 (0.75, 0.25)	−0.26 (0.31, 0.69)	nan (0.99, 0.01)	−0.37 (0.12, 0.88)	nan (0.99, 0.01)	3.27 (0.12, 0.88)
	2^{16}	22	−0.11 (0.75, 0.25)	−0.24 (0.31, 0.69)	nan (0.99, 0.01)	−1.35 (0.12, 0.88)	nan (0.99, 0.01)	2.36 (0.12, 0.88)
	2^{17}	23	0.29 (0.75, 0.25)	−0.36 (0.31, 0.69)	nan (0.99, 0.01)	0.15 (0.12, 0.88)	nan (0.99, 0.01)	2.02 (0.12, 0.88)
	2^2	8	−0.01 (0.64, 0.36)	−0.01 (0.23, 0.77)	0.03 (0.92, 0.08)	0.00 (0.02, 0.98)	0.05 (0.92, 0.08)	−0.02 (0.02, 0.98)
	2^3	9	0.00 (0.72, 0.28)	0.07 (0.24, 0.76)	0.02 (0.97, 0.03)	0.01 (0.06, 0.94)	−0.07 (0.97, 0.03)	0.01 (0.06, 0.94)
	2^4	10	0.00 (0.74, 0.26)	0.02 (0.27, 0.73)	−0.07 (0.99, 0.01)	−0.06 (0.09, 0.91)	0.12 (0.99, 0.01)	0.14 (0.09, 0.91)
	2^5	11	0.05 (0.74, 0.26)	−0.03 (0.29, 0.71)	0.13 (0.99, 0.01)	0.03 (0.10, 0.90)	0.16 (0.99, 0.01)	0.37 (0.11, 0.89)
	2^6	12	0.07 (0.75, 0.25)	0.01 (0.30, 0.70)	0.99 (0.99, 0.01)	0.68 (0.11, 0.89)	0.03 (0.99, 0.01)	−0.03 (0.12, 0.88)
	2^7	13	0.10 (0.75, 0.25)	−0.09 (0.30, 0.70)	1.36 (0.99, 0.01)	−0.07 (0.12, 0.88)	2.18 (0.99, 0.01)	0.51 (0.12, 0.88)
10^6	2^8	14	−0.07 (0.75, 0.25)	0.00 (0.31, 0.69)	8.58 (0.99, 0.01)	−0.12 (0.12, 0.88)	3.63 (0.99, 0.01)	−1.34 (0.12, 0.88)
	2^9	15	0.05 (0.75, 0.25)	−0.08 (0.31, 0.69)	nan (0.99, 0.01)	0.23 (0.12, 0.88)	nan (0.99, 0.01)	0.25 (0.12, 0.88)
	2^{10}	16	−0.14 (0.75, 0.25)	−0.12 (0.31, 0.69)	nan (0.99, 0.01)	−0.31 (0.12, 0.88)	nan (0.99, 0.01)	0.71 (0.12, 0.88)
	2^{11}	17	−0.09 (0.75, 0.25)	0.03 (0.31, 0.69)	nan (0.99, 0.01)	0.88 (0.12, 0.88)	nan (0.99, 0.01)	−0.31 (0.12, 0.88)
	2^{12}	18	−0.04 (0.75, 0.25)	−0.11 (0.31, 0.69)	nan (0.99, 0.01)	−0.32 (0.12, 0.88)	nan (0.99, 0.01)	−0.82 (0.12, 0.88)
	2^{13}	19	0.04 (0.75, 0.25)	0.00 (0.31, 0.69)	nan (0.99, 0.01)	0.33 (0.12, 0.88)	nan (0.99, 0.01)	−0.86 (0.12, 0.88)
	2^{14}	20	−0.12 (0.75, 0.25)	−0.07 (0.31, 0.69)	nan (0.99, 0.01)	0.84 (0.12, 0.88)	nan (0.99, 0.01)	−0.06 (0.12, 0.88)
	2^{15}	21	0.02 (0.75, 0.25)	0.01 (0.31, 0.69)	nan (0.99, 0.01)	0.07 (0.12, 0.88)	nan (0.99, 0.01)	0.14 (0.12, 0.88)
	2^{16}	22	0.09 (0.75, 0.25)	−0.05 (0.31, 0.69)	nan (0.99, 0.01)	0.75 (0.12, 0.88)	nan (0.99, 0.01)	0.21 (0.12, 0.88)
	2^{17}	23	0.03 (0.75, 0.25)	0.06 (0.31, 0.69)	nan (0.99, 0.01)	1.02 (0.12, 0.88)	nan (0.99, 0.01)	0.45 (0.12, 0.88)

the excitation energies decrease monotonically as we go from KH to CsH. We combine this observation with our data from Table XIII where the maximum eigenvalue grows much faster than the decrease in minimum eigenvalue from KH to RbH to CsH for a given choice of n_o and n_v, to infer that κ decreases monotonically from KH to CsH.

Furthermore, in Fig. 9(c), KH's condition number reaches a staggering 4000 with all the virtuals considered, whereas in Figs. 9(a) and 9(b), κ is substantially lower. This is not surprising, as for Fig. 9(c), we consider 10 occupied orbitals. Since KH has only 10 occupied orbitals, the active space contains the $1s$ orbital of K. We can invoke the fact that the orbital energy gap is larger between the inner s orbitals, for example, and the density of orbitals becomes higher in the vicinity of highest occupied molecular orbital and the lowest unoccupied molecular orbital. Thus, if we include inner core orbitals in our active space, we expect the excitation energy of the highest state, namely, the largest eigenvalue of the A matrix, to be larger. In contrast, for the 6, 8, and the 10 occupied orbitals' cases, RbH and CsH have comparable condition numbers. This can be attributed to the fact that the lowest orbital is always the $3d$ of Rb in all three cases. Since the orbital character of the lowest orbital is the same among the three active spaces, they yield very similar condition numbers.

We add at this juncture that while considering only three molecules does not allow any quantitative inference on the behavior of condition number with system size, it gives a qualitative indication that quantum chemistry using HHL-LCCSD may be a reasonable direction to consider. However, further analysis would be required to assess what one would expect for $\kappa(m)$ in general for an HHL-LCC computation.

3. HHL and Psi-HHL results

We now discuss our results for the performance of the HHL and Psi-HHL algorithms for the molecules considered in this work.

We begin by noting that it is not practical to carry out an analysis similar to that in Fig. 7 since, unlike the toy matrices case, the condition number grows much slower and the computations become too expensive too soon. We thus move to Fig. 10 (with the accompanying data given in Table XIV of the Appendix), where we carry out a study on the same lines as Fig. 8. We vary the number of shots and compare the

TABLE VI. Table providing the data for HHL and Psi-HHL algorithms (with $\alpha = 80^\circ$) for 4×4 matrices. The notations are the same as those used in Tables IV and V. Each data point is generated by taking the average over 50 repetitions.

			A diag $\vec{b}$ equal		A diag $\vec{b}$ unequal		A not diag $\vec{b}$ unequal	
No. shots	$\approx \kappa$	No. qubits	PFD ($P(0)$, $P(1)$)	PFD ($P'(0)$, $P'(1)$)	PFD ($P(0)$, $P(1)$)	PFD ($P'(0)$, $P'(1)$)	PFD ($P(0)$, $P(1)$)	PFD ($P'(0)$, $P'(1)$)
	2^2	8	−0.08 (0.64, 0.36)	−0.08 (0.28, 0.72)	0.04 (0.92, 0.08)	0.27 (0.02, 0.98)	0.07 (0.92, 0.08)	0.26 (0.02, 0.98)
	2^3	9	0.01 (0.72, 0.28)	−0.14 (0.24, 0.76)	−0.06 (0.97, 0.03)	0.14 (0.01, 0.99)	−0.02 (0.97, 0.03)	0.05 (0.02, 0.98)
	2^4	10	−0.01 (0.74, 0.26)	0.13 (0.24, 0.76)	0.31 (0.99, 0.01)	0.14 (0.02, 0.98)	0.48 (0.99, 0.01)	−0.37 (0.02, 0.98)
	2^5	11	−0.06 (0.75, 0.25)	−0.41 (0.26, 0.74)	1.85 (0.99, 0.01)	0.27 (0.03, 0.97)	−0.10 (0.99, 0.01)	−0.33 (0.03, 0.97)
	2^6	12	0.08 (0.75, 0.25)	−0.62 (0.26, 0.74)	nan (0.99, 0.01)	−0.48 (0.04, 0.96)	nan (0.99, 0.01)	−0.28 (0.03, 0.97)
	2^7	13	−0.01 (0.75, 0.25)	0.76 (0.26, 0.74)	nan (0.99, 0.01)	−1.63 (0.04, 0.96)	nan (0.99, 0.01)	1.86 (0.04, 0.96)
10^5	2^8	14	0.15 (0.75, 0.25)	0.18 (0.26, 0.74)	nan (0.99, 0.01)	−1.02 (0.04, 0.96)	nan (0.99, 0.01)	1.42 (0.04, 0.96)
	2^9	15	0.12 (0.75, 0.25)	0.20 (0.27, 0.73)	nan (0.99, 0.01)	5.05 (0.04, 0.96)	nan (0.99, 0.01)	4.95 (0.04, 0.96)
	2^{10}	16	−0.01 (0.75, 0.25)	0.25 (0.26, 0.74)	nan (0.99, 0.01)	2.12 (0.04, 0.96)	nan (0.99, 0.01)	−3.28 (0.04, 0.96)
	2^{11}	17	−0.05 (0.75, 0.25)	0.85 (0.26, 0.74)	nan (0.99, 0.01)	0.70 (0.04, 0.96)	nan (0.99, 0.01)	0.53 (0.04, 0.96)
	2^{12}	18	0.02 (0.75, 0.25)	−0.29 (0.26, 0.74)	nan (0.99, 0.01)	6.62 (0.04, 0.96)	nan (0.99, 0.01)	2.93 (0.04, 0.96)
	2^{13}	19	0.10 (0.75, 0.25)	1.14 (0.27, 0.73)	nan (0.99, 0.01)	5.23 (0.04, 0.96)	nan (0.99, 0.01)	0.42 (0.04, 0.96)
	2^{14}	20	0.27 (0.75, 0.25)	−0.46 (0.26, 0.74)	nan (0.99, 0.01)	6.99 (0.04, 0.96)	nan (0.99, 0.01)	2.82 (0.04, 0.96)
	2^{15}	21	0.21 (0.75, 0.25)	0.50 (0.26, 0.74)	nan (0.99, 0.01)	1.87 (0.04, 0.96)	nan (0.99, 0.01)	1.49 (0.04, 0.96)
	2^{16}	22	−0.11 (0.75, 0.25)	−0.46 (0.27, 0.73)	nan (0.99, 0.01)	−1.35 (0.04, 0.96)	nan (0.99, 0.01)	0.76 (0.04, 0.96)
	2^{17}	23	0.30 (0.75, 0.25)	−0.36 (0.26, 0.74)	nan (0.99, 0.01)	0.16 (0.04, 0.96)	nan (0.99, 0.01)	1.32 (0.04, 0.96)
	2^2	8	−0.01 (0.64, 0.36)	0.08 (0.28, 0.72)	0.03 (0.92, 0.08)	0.00 (0.02, 0.98)	0.05 (0.92, 0.08)	−0.02 (0.02, 0.98)
	2^3	9	0.00 (0.72, 0.28)	−0.21 (0.24, 0.76)	0.02 (0.97, 0.03)	−0.02 (0.01, 0.99)	−0.07 (0.97, 0.03)	−0.11 (0.01, 0.99)
	2^4	10	0.00 (0.74, 0.26)	−0.20 (0.25, 0.75)	−0.07 (0.99, 0.01)	−0.01 (0.02, 0.98)	0.12 (0.99, 0.01)	0.05 (0.02, 0.98)
	2^5	11	0.06 (0.75, 0.25)	0.19 (0.26, 0.74)	0.12 (0.99, 0.01)	0.49 (0.03, 0.97)	0.16 (0.99, 0.01)	0.17 (0.03, 0.97)
	2^6	12	0.07 (0.75, 0.25)	−0.40 (0.26, 0.74)	0.99 (0.99, 0.01)	0.25 (0.04, 0.96)	0.03 (0.99, 0.01)	0.23 (0.03, 0.97)
	2^7	13	0.10 (0.75, 0.25)	0.01 (0.26, 0.74)	1.36 (0.99, 0.01)	0.18 (0.04, 0.96)	2.18 (0.99, 0.01)	0.18 (0.03, 0.97)
	2^8	14	−0.07 (0.75, 0.25)	−0.08 (0.26, 0.74)	8.58 (0.99, 0.01)	−0.09 (0.04, 0.96)	3.63 (0.99, 0.01)	−0.61 (0.04, 0.96)
10^6	2^9	15	0.05 (0.75, 0.25)	0.24 (0.26, 0.74)	nan (0.99, 0.01)	0.84 (0.04, 0.96)	nan (0.99, 0.01)	0.01 (0.04, 0.96)
	2^{10}	16	−0.14 (0.75, 0.25)	−0.21 (0.26, 0.74)	nan (0.99, 0.01)	−0.93 (0.04, 0.96)	nan (0.99, 0.01)	0.63 (0.04, 0.96)
	2^{11}	17	−0.09 (0.75, 0.25)	0.00 (0.26, 0.74)	nan (0.99, 0.01)	1.95 (0.04, 0.96)	nan (0.99, 0.01)	−0.37 (0.04, 0.96)
	2^{12}	18	−0.04 (0.75, 0.25)	−0.14 (0.26, 0.74)	nan (0.99, 0.01)	0.54 (0.04, 0.96)	nan (0.99, 0.01)	2.01 (0.04, 0.96)
	2^{13}	19	0.04 (0.75, 0.25)	0.15 (0.26, 0.74)	nan (0.99, 0.01)	−0.75 (0.04, 0.96)	nan (0.99, 0.01)	−1.04 (0.04, 0.96)
	2^{14}	20	−0.12 (0.75, 0.25)	0.13 (0.26, 0.74)	nan (0.99, 0.01)	0.32 (0.04, 0.96)	nan (0.99, 0.01)	0.21 (0.04, 0.96)
	2^{15}	21	0.02 (0.75, 0.25)	0.01 (0.26, 0.74)	nan (0.99, 0.01)	−0.66 (0.04, 0.96)	nan (0.99, 0.01)	−0.37 (0.04, 0.96)
	2^{16}	22	0.08 (0.75, 0.25)	0.13 (0.26, 0.74)	nan (0.99, 0.01)	0.65 (0.04, 0.96)	nan (0.99, 0.01)	0.45 (0.04, 0.96)
	2^{17}	23	0.02 (0.75, 0.25)	−0.24 (0.26, 0.74)	nan (0.99, 0.01)	−2.53 (0.04, 0.96)	nan (0.99, 0.01)	0.52 (0.04, 0.96)

TABLE VII. Summary of the fitted probabilities obtained from HHL and Psi-HHL for the 4×4 case of A not diagonal and $\vec{b}$ in an unequal superposition, for $\alpha = 60^\circ, 70^\circ, 80^\circ$. The number of shots is fixed to 10^6.

α	$\approx \kappa$	$P_{\text{Fit}}(0)$	$P_{\text{Fit}}(1)$	$P_{\text{Fit}}(0) + P_{\text{Fit}}(1)$	$P'_{\text{Fit}}(0)$	$P'_{\text{Fit}}(1)$	$P'_{\text{Fit}}(0) + P'_{\text{Fit}}(1)$
60°	4	0.92	0.08	1.00	0.08	0.92	1.00
	32	0.99	0.01	1.00	0.22	0.78	1.00
	64	0.99	0.01	1.00	0.24	0.76	1.00
	1024	0.99	0.01	1.00	0.25	0.75	1.00
	2048	0.99	0.01	1.00	0.25	0.75	1.00
70°	4	0.92	0.08	1.00	0.02	0.98	1.00
	32	0.99	0.01	1.00	0.10	0.90	1.00
	128	0.99	0.01	1.00	0.11	0.89	1.00
	1024	0.99	0.01	1.00	0.12	0.88	1.00
	2048	0.99	0.01	1.00	0.12	0.88	1.00
80°	4	0.92	0.08	1.00	0.02	0.98	1.00
	32	0.99	0.01	1.00	0.03	0.97	1.00
	128	0.99	0.01	1.00	0.03	0.97	1.00
	1024	0.99	0.01	1.00	0.04	0.96	1.00
	2048	0.99	0.01	1.00	0.04	0.96	1.00

TABLE VIII. Table providing the data for HHL and Psi-HHL algorithms (with $\alpha = 60^\circ, 70^\circ, 80^\circ$) for 8×8 matrices. A is a nondiagonal matrix and $\vec{b}$ is an unequal superposition. Each data point is an average over 10 repetitions.

			HHL	Psi-HHL		
				$\alpha = 60^\circ$	$\alpha = 70^\circ$	$\alpha = 80^\circ$
No. shots	$\approx \kappa$	No. qubits	PFD ($P(0)$, $P(1)$)	PFD ($P'(0)$, $P'(1)$)	PFD ($P'(0)$, $P'(1)$)	PFD ($P'(0)$, $P'(1)$)
	2^2	10	−7.05 (0.82, 0.18)	4.90 (0.07, 0.93)	5.99 (0.05, 0.95)	6.97 (0.10, 0.90)
	2^3	11	−6.18 (0.95, 0.05)	−3.11 (0.11, 0.89)	−2.93 (0.03, 0.97)	−2.93 (0.01, 0.99)
	2^4	12	−8.78 (0.98, 0.02)	−2.75 (0.18, 0.82)	−2.48 (0.07, 0.93)	−2.54 (0.02, 0.98)
	2^5	13	0.42 (0.99, 0.01)	1.60 (0.21, 0.79)	−0.90 (0.10, 0.90)	−0.09 (0.02, 0.98)
	2^6	14	0.12 (0.99, 0.01)	−5.01 (0.23, 0.77)	−1.21 (0.11, 0.89)	−4.35 (0.03, 0.97)
	2^7	15	0.09 (0.99, 0.01)	0.09 (0.24, 0.76)	−3.83 (0.12, 0.88)	0.40 (0.03, 0.97)
10^5	2^8	16	nan (0.99, 0.01)	−0.33 (0.25, 0.75)	−1.74 (0.12, 0.88)	−4.53 (0.03, 0.97)
	2^9	17	nan (0.99, 0.01)	−13.83 (0.25, 0.75)	−3.82 (0.12, 0.88)	10.35 (0.04, 0.96)
	2^{10}	18	nan (0.99, 0.01)	−1.66 (0.25, 0.75)	0.94 (0.12, 0.88)	−7.44(0.04, 0.96)
	2^{11}	19	nan (0.99, 0.01)	−0.82 (0.25, 0.75)	4.90 (0.12, 0.88)	3.13 (0.04, 0.96)
	2^{12}	20	nan (0.99, 0.01)	−0.91 (0.25, 0.75)	−7.52 (0.12, 0.88)	10.89 (0.04, 0.96)
	2^{13}	21	nan (0.99, 0.01)	2.62 (0.25, 0.75)	8.41 (0.12, 0.88)	−0.26 (0.04, 0.96)
	2^{14}	22	nan (0.99, 0.01)	−3.20 (0.25, 0.75)	7.12 (0.12, 0.88)	8.53 (0.04, 0.96)
	2^{15}	23	nan (0.99, 0.01)	5.74 (0.25, 0.75)	−7.34 (0.12, 0.88)	−7.60 (0.04, 0.96)
	2^{16}	24	nan (0.99, 0.01)	−5.89 (0.25, 0.75)	−4.65 (0.12, 0.88)	−13.89 (0.04, 0.96)
	2^{17}	25	nan (0.99, 0.01)	−6.58 (0.25, 0.75)	−10.10 (0.12, 0.88)	2.78 (0.04, 0.96)
	2^2	10	−7.10 (0.82, 0.18)	5.23 (0.10, 0.99)	6.13 (0.05, 0.95)	7.15 (0.10, 0.90)
	2^3	11	−6.10 (0.95, 0.05)	−3.14 (0.10, 0.90)	−3.02 (0.03, 0.97)	−2.83 (0.01, 0.99)
	2^4	12	−8.97 (0.98, 0.02)	−2.60 (0.18, 0.82)	−2.58 (0.07, 0.93)	−2.71 (0.02, 0.98)
	2^5	13	−1.76 (0.99, 0.01)	0.04 (0.21, 0.79)	0.03 (0.09, 0.91)	−0.04 (0.02, 0.98)
	2^6	14	−5.00 (0.99, 0.01)	−1.49 (0.23, 0.77)	−0.73 (0.11, 0.89)	−1.09 (0.03, 0.97)
	2^7	15	1.96 (0.99, 0.01)	−2.18 (0.24, 0.76)	1.16 (0.12, 0.88)	0.36 (0.03, 0.97)
10^6	2^8	16	0.78 (0.99, 0.01)	1.51 (0.25, 0.75)	−1.35 (0.12, 0.88)	−1.61 (0.04, 0.96)
	2^9	17	nan (0.99, 0.01)	2.19 (0.25, 0.75)	1.34 (0.12, 0.88)	−1.99 (0.04, 0.96)
	2^{10}	18	nan (0.99, 0.01)	0.08 (0.25, 0.75)	−3.98 (0.12, 0.88)	0.33 (0.04, 0.96)
	2^{11}	19	nan (0.99, 0.01)	1.51 (0.25, 0.75)	−4.00 (0.12, 0.88)	−1.72 (0.04, 0.96)
	2^{12}	20	nan (0.99, 0.01)	1.34 (0.25, 0.75)	0.28 (0.12, 0.88)	0.00 (0.04, 0.96)
	2^{13}	21	nan (0.99, 0.01)	−2.83 (0.25, 0.75)	1.03 (0.12, 0.88)	1.99 (0.04, 0.96)
	2^{14}	22	nan (0.99, 0.01)	3.20 (0.25, 0.75)	−4.70 (0.12, 0.88)	1.75 (0.04, 0.96)
	2^{15}	23	nan (0.99, 0.01)	−0.19 (0.25, 0.75)	−4.56 (0.12, 0.88)	−0.58 (0.04, 0.96)
	2^{16}	24	nan (0.99, 0.01)	0.97 (0.25, 0.75)	0.14 (0.12, 0.88)	−0.11 (0.04, 0.96)
	2^{17}	25	nan (0.99, 0.01)	0.62 (0.25, 0.75)	3.21 (0.12, 0.88)	3.19 (0.04, 0.96)

TABLE IX. Table providing the data for HHL and Psi-HHL algorithms (with $\alpha = 60^\circ, 70^\circ, 80^\circ$) for 16×16 matrices. A is a nondiagonal matrix and $\vec{b}$ is an unequal superposition. Each data point is an average over 10 repetitions.

			HHL	Psi-HHL		
				60°	70°	80°
No. shots	$\approx \kappa$	No. qubits	PFD ($P(0)$, $P(1)$)	PFD ($P'(0)$, $P'(1)$)	PFD ($P'(0)$, $P'(1)$)	PFD ($P'(0)$, $P'(1)$)
	2^2	12	−5.50 (0.83, 0.17)	3.60 (0.06, 0.94)	4.29 (0.04, 0.96)	5.11 (0.08, 0.92)
	2^3	13	−7.02 (0.95, 0.05)	−3.42 (0.11, 0.89)	−3.26 (0.03, 0.97)	−3.19 (0.01, 0.99)
	2^4	14	7.05 (0.98, 0.02)	−2.09 (0.18, 0.82)	−2.17 (0.07, 0.93)	−1.76 (0.01, 0.99)
	2^5	15	−1.70 (0.99, 0.01)	−0.75 (0.21, 0.79)	−0.53 (0.10, 0.91)	0.92 (0.02, 0.98)
	2^6	16	−3.51 (0.99, 0.01)	0.10 (0.23, 0.77)	0.60 (0.11, 0.89)	−0.06 (0.03, 0.97)
	2^7	17	−1.95 (0.99, 0.01)	−1.22 (0.24, 0.76)	−1.18 (0.11, 0.89)	−2.15 (0.03, 0.97)
10^6	2^8	18	−2.30 (0.99, 0.01)	−1.30 (0.25, 0.75)	0.47 (0.12, 0.88)	2.68 (0.03, 0.97)
	2^9	19	nan (0.99, 0.01)	−0.85 (0.25, 0.75)	3.64 (0.12, 0.88)	−0.04 (0.04, 0.97)
	2^{10}	20	nan (0.99, 0.01)	1.75 (0.25, 0.75)	−0.11 (0.12, 0.88)	−5.97 (0.04, 0.96)
	2^{11}	21	nan (0.99, 0.01)	−2.02 (0.25, 0.75)	−2.59 (0.12, 0.88)	3.26 (0.04, 0.96)
	2^{12}	22	nan (0.99, 0.01)	−2.75 (0.25, 0.75)	−4.15 (0.12, 0.88)	−7.93 (0.04, 0.96)
	2^{13}	23	nan (0.99, 0.01)	−4.07 (0.25, 0.75)	0.29 (0.12, 0.88)	1.88 (0.04, 0.96)
	2^{14}	24	nan (0.99, 0.01)	−3.97 (0.25, 0.75)	−0.83 (0.12, 0.88)	1.30 (0.04, 0.96)
	2^{15}	25	nan (0.99, 0.01)	7.01 (0.25, 0.75)	−1.46 (0.12, 0.88)	2.07 (0.04, 0.96)
	2^{16}	26	nan (0.99, 0.01)	−1.31 (0.25, 0.75)	−5.10 (0.12, 0.88)	−11.71 (0.04, 0.96)

TABLE X. Table providing the data for HHL and Psi-HHL algorithms (with $\alpha = 60^\circ, 70^\circ, 80^\circ$) for 32×32 matrices. A is a nondiagonal matrix and $\vec{b}$ is an unequal superposition. Each data point is an average over 10 repetitions.

			HHL	Psi-HHL		
				60°	70°	80°
No. shots	$\approx \kappa$	No. qubits	PFD ($P(0)$, $P(1)$)	PFD ($P'(0)$, $P'(1)$)	PFD ($P'(0)$, $P'(1)$)	PFD ($P'(0)$, $P'(1)$)
	2^2	14	−5.23 (0.17, 0.83)	−3.73 (0.11, 0.89)	−3.56 (0.08, 0.92)	−3.42 (0.10, 0.90)
	2^3	15	−2.27 (0.05, 0.95)	−1.28 (0.13, 0.87)	−1.16 (0.04, 0.96)	−1.09 (0.02, 0.98)
	2^4	16	−3.27 (0.02, 0.98)	−1.90 (0.18, 0.82)	−1.70 (0.07, 0.93)	−1.47 (0.02, 0.98)
	2^5	17	−0.87 (0.01, 0.99)	−0.95 (0.21, 0.79)	−0.45 (0.10, 0.90)	−0.49 (0.02, 0.98)
10^6	2^6	18	−2.71 (0.00,1.00)	−0.56 (0.23, 0.77)	−0.80 (0.11, 0.89)	0.49 (0.03, 0.97)
	2^7	19	−0.10 (0.00, 1.00)	−0.93 (0.24, 0.76)	−0.05 (0.11,0.89)	−0.61 (0.03, 0.97)
	2^8	20	5.48 (0.00, 1.00)	−0.91 (0.25, 0.75)	1.97 (0.12, 0.88)	−4.47 (0.03, 0.97)
	2^9	21	nan (0.00, 1.00)	−3.74 (0.25, 0.75)	2.07 (0.12, 0.88)	−2.92 (0.03, 0.97)
	2^{10}	22	nan (0.00, 1.00)	−1.17 (0.25, 0.75)	2.07 (0.12, 0.88)	−0.50 (0.03, 0.97)
	2^{11}	23	nan (0.00, 1.00)	4.90 (0.25, 0.75)	7.32 (0.12, 0.88)	−3.07 (0.03, 0.97)
	2^{12}	24	nan (0.00, 1.00)	6.11 (0.25, 0.75)	−1.09 (0.12, 0.88)	8.85 (0.03, 0.97)
	2^{13}	25	nan (0.00, 1.00)	0.76 (0.25, 0.75)	−4.61 (0.12, 0.88)	−0.63 (0.03, 0.97)
	2^{14}	26	nan (0.00, 1.00)	8.74 (0.25, 0.75)	7.76 (0.12, 0.88)	1.40 (0.03, 0.97)

performance of HHL and Psi-HHL in predicting the PFD, as well as the range across which the PFDs are spread, across 30 repetitions. For this analysis, we consider Li_2 and KH. The details are as follows:

(1) Li_2: 21-qubit circuit with an A matrix size of 64×64 (built out of single and double excitations arising from 3 occupied and 7 virtual orbitals) in the STO-6G basis, with $\kappa = 64.07$.

(2) KH: 26-qubit circuit with an A matrix size of 256×256 (built out of single and double excitations arising from 6 occupied and 6 virtual orbitals) in the Sapporo double-zeta basis, with $\kappa = 365.40$.

We pick these two systems, since in one case, κ is less than 100, and in the other much larger at over 300. Repeating the calculations for RbH and CsH may not give any new insights, and hence we restrict the results only to Li_2 and KH. For Li_2, the condition number is very small, and hence we only study the performance of HHL and Psi-HHL between 500 and 10 000 shots. The data clearly show that for Li_2, the Psi-HHL approach always has a smaller spread in PFDs when compared to HHL. For KH, we observe that at 1000 shots, HHL fails, while Psi-HHL does not, but comes with large error bars. As we increase the number of shots, the error bars for both HHL and Psi-HHL are seen to become much smaller, but Psi-HHL consistently has smaller error bars than HHL.

We now move to our next set of results, namely, the PEC for the KH molecule. Since it is computationally not feasible to pick the larger system sizes from Fig. 9, we choose the 6 occupied and 6 virtual orbitals case. This choice corresponds to a 26-qubit calculation with an A matrix size of 256×256. We consider geometries in the neighbourhood of the equilibrium bond length (3 geometries in steps of 0.47 bohrs on either side of the equilibrium bond length). With such a choice, the correlation energies required to be captured ranges from about 0.3 mHa (milli-Hartree) for 5.65-bohrs geometry to 3 mHa for the 2.82-bohrs geometry (the two extreme points in the 7 geometries considered), thus allowing us to check the performance of HHL and Psi-HHL across a range of correlation energy values. Calculating energies across a range of bond lengths further allows us to check across a (limited) range of condition numbers (the smallest being 365.40 and the largest 393.21) the behavior of HHL and Psi-HHL. Each

TABLE XI. Table providing the data for HHL and Psi-HHL algorithms (with $\alpha = 60^\circ, 70^\circ, 80^\circ$) for 64×64 matrices. A is a nondiagonal matrix and $\vec{b}$ is an unequal superposition. Each data point is an average over 10 repetitions.

			HHL	Psi-HHL		
				60°	70°	80°
No. shots	$\approx \kappa$	No. qubits	PFD ($P(0)$, $P(1)$)	PFD ($P'(0)$, $P'(1)$)	PFD ($P'(0)$, $P'(1)$)	PFD ($P'(0)$, $P'(1)$)
	2^2	16	−3.13 (0.82, 0.17)	0.01 (0.12, 0.88)	0.21 (0.09, 0.91)	0.82 (0.10, 0.90)
	2^3	17	−2.26 (0.94, 0.05)	−1.06 (0.01, 0.88)	−0.95 (0.04, 0.96)	−1.01 (0.02, 0.98)
	2^4	18	−2.91 (0.98, 0.02)	−1.82 (0.17, 0.83)	1.47 (0.03, 0.97)	−1.56 (0.02, 0.98)
10^6	2^5	19	−2.16 (0.99, 0.01)	−1.27 (0.21, 0.79)	−1.57 (0.10, 0.91)	−0.86 (0.02, 0.98)
	2^6	20	−1.28 (1.00, 0.00)	−0.55 (0.23, 0.77)	−1.26 (0.10, 0.90)	−1.06 (0.02, 0.98)
	2^7	21	−6.18 (1.00, 0.00)	0.16 (0.24, 0.76)	−0.10 (0.11, 0.89)	−0.10 (0.03, 0.97)
	2^8	22	nan (1.00, 0.00)	−0.86 (0.25, 0.75)	−0.45 (0.11, 0.89)	0.18 (0.03, 0.97)
	2^9	23	nan (1.00, 0.00)	−0.40 (0.25, 0.75)	0.05 (0.12, 0.88)	−2.46 (0.03, 0.97)
	2^{10}	24	nan (1.00, 0.00)	1.47 (0.25, 0.75)	1.47 (0.12, 0.88)	2.09 (0.03, 0.97)

TABLE XII. Table providing the data for condition number (κ) of the $m \times m$ A_{mol} matrix versus system size (m), for KH, RbH, and CsH molecules, where we vary the virtual orbitals to increase m. In the table, n_o is the number of active spin orbitals, and n_v is the number of unoccupied spin orbitals. The column labeled "Reordered virtual MOs" represents the atomic orbitals reordered according to the ones that contribute dominantly to the virtual molecular orbital. The column labeled "MO energies" gives the virtual molecular orbital energies in units of milli-Hartree.

Molecule	Reordered virtual MOs	MO energies	$n_o = 6$		$n_o = 8$		$n_o = 10$	
			m	κ (n_o, n_v)	m	κ (n_o, n_v)	m	κ (n_o, n_v)
	K $4s$	1151.70	202	233.65 (6, 6)	580	41.03 (8, 8)	1484	2195.80 (10, 10)
	K $4p_y$	3609.70	274	234.44 (6, 7)	745	41.57 (8, 9)	1761	2206.59 (10, 11)
	K $4p_x$	3609.70	337	235.12 (6, 8)	932	236.57 (8, 10)	2046	2217.42 (10, 12)
	K $4p_z$	3663.70	432	236.80 (6, 9)	1110	237.74 (8, 11)	2451	2323.69 (10, 13)
	K $3d_{xy}$	743.00	541	238.28 (6, 10)	1296	238.90 (8, 12)	2900	2849.98 (10, 14)
	K $3dy^2$	743.00	655	244.66 (6, 11)	1540	250.34 (8, 13)	3393	2904.40 (10, 15)
	K $3d_{yz}$	747.40	748	250.45 (6, 12)	1808	307.03 (8, 14)	3794	2933.74 (10, 16)
	K $3d_{xz}$	747.40	889	265.31 (6, 13)	2100	312.83 (8, 15)	4203	2964.04 (10, 17)
	K $3dz^2$	755.30	1043	340.59 (6, 14)	2358	316.09 (8, 16)	4788	3610.73 (10, 18)
	K $6s$	3.70	1213	348.68 (6, 15)	2624	319.44 (8, 17)	5265	3629.57 (10, 19)
	K $6p_y$	72.70	1381	371.54 (6, 16)	2972	389.11 (8, 18)	5750	3648.68 (10, 20)
KH	K $6p_x$	72.70	1510	374.07 (6, 17)	3278	391.14 (8, 19)	6427	3674.83 (10, 21)
	K $6p_z$	82.80	1711	380.25 (6, 18)	3592	393.20 (8, 20)		
	K $5s$	147.20	1909	385.51 (6, 19)	3996	395.77 (8, 21)		
	K $5p_z$	692.70	2062	386.30 (6, 20)				
	K $5p_y$	702.90	2295	389.76 (6, 21)				
	K $5p_x$	702.90						
	H $2s$	934.00						
	H $2p_y$	1668.70						
	H $2p_x$	1668.70						
	H $2p_z$	1914.10						
	Rb $5s - 5p_z$ hybrid	940.00	209	102.73 (6, 6)	632	104.88 (8, 8)	1401	108.16 (10, 10)
	Rb $5s$	925.80	279	103.00 (6, 7)	744	105.81 (8, 9)	1673	111.85 (10, 11)
	Rb $5p_x$	2283.00	370	103.74 (6, 8)	932	106.63 (8, 10)	1963	115.27 (10, 12)
	Rb $5p_y$	2283.00	432	104.65 (6, 9)	1110	110.27 (8, 11)	2321	125.33 (10, 13)
	Rb $5p_z$	2305.80	541	105.46 (6, 10)	1296	113.64 (8, 12)	2713	156.32 (10, 14)
	Rb $4d_{xy}$	635.40	630	109.05 (6, 11)	1540	123.51 (8, 13)	3141	182.23 (10, 15)
	Rb $4dx^2$	635.40	748	112.38 (6, 12)	1808	154.29 (8, 14)	3537	206.22 (10, 16)
	Rb $4d_{xz}$	641.20	889	122.12 (6, 13)	2100	179.90 (8, 15)	3951	207.93 (10, 17)
	Rb $4d_{yz}$	641.20	1044	152.70 (6, 14)	2358	203.86 (8, 16)	4460	213.88 (10, 18)
RbH	Rb $4dz^2$	666.90	1213	178.09 (6, 15)	2624	205.55 (8, 17)	4932	214.42 (10, 19)
	Rb $7s$	3.20	1381	202.02 (6, 16)	2972	211.53 (8, 18)	5422	214.96 (10, 20)
	Rb $7p_x$	64.20	1510	203.70 (6, 17)	3278	212.06 (8, 19)	6013	216.27 (10, 21)
	Rb $7p_y$	64.20	1711	209.67 (6, 18)	3592	212.60 (8, 20)		
	Rb $6s$	78.40	1860	210.19 (6, 19)	3996	213.87 (8, 21)		
	Rb $6s$	130.80	2062	210.72 (6, 20)				
	Rb $6p_x$	477.70	2295	211.94 (6, 21)				
	Rb $6p_y$	477.70						
	Rb $6p_z$	487.50						
	H $2p_x$	1678.20						
	H$2p_y$	1678.20						
	H$2p_z$	1903.50						
	Cs $6p_x$	364.80	209	77.05 (6, 6)	632	81.29 (8, 8)	1484	94.54 (10, 10)
	Cs $6p_y$	364.80	279	77.18 (6, 7)	812	92.18 (8, 9)	1711	95.68 (10, 11)
	Cs $6p_z$	382.00	370	80.54 (6, 8)	1016	93.40 (8, 10)	2007	100.02 (10, 12)
	Cs $6s$	1455.30	475	91.32 (6, 9)	1044	94.51 (8, 11)	2321	104.14 (10, 13)
	Cs $8s$	172.00	595	92.54 (6, 10)	1339	98.79 (8, 12)	2714	114.07 (10, 14)
	Cs$7p_y$	25.50	664	93.63 (6, 11)	1540	102.85 (8, 13)	3141	157.90 (10, 15)
	Cs $7p_x$	25.50	759	97.83 (6, 12)	1808	112.65 (8, 14)	3537	184.86 (10, 16)
	Cs $7s - 7p_y$ hybrid	75.60	890	101.83 (6, 13)	2100	156.01 (8, 15)	3951	186.03 (10, 17)
	Cs $7s$	85.50	1044	111.49 (6, 14)	2358	182.96 (8, 16)	4461	192.15 (10, 18)

TABLE XII. (*Continued.*)

Molecule	Reordered virtual MOs	MO energies	$n_o = 6$		$n_o = 8$		$n_o = 10$	
			m	κ (n_o, n_v)	m	κ (n_o, n_v)	m	κ (n_o, n_v)
CsH	Cs $5dy^2$	307.30	1213	154.45 (6, 15)	2624	184.12 (8, 17)		
	Cs $5d_{xy}$	307.30	1338	181.34 (6, 16)	2973	190.17 (8, 18)		
	Cs $5d_{xz}$	309.70	1510	182.49 (6, 17)				
	Cs $5d_{yz}$	309.70	1711	188.52 (6, 18)				
	Cs $5dz^2$	310.90						
	H $2s$	882.50						
	H $2p_x$	1716.80						
	H $2p_y$	1716.80						
	H $2p_z$	1716.80						

calculation involves 50 000 shots and our reported results are averaged over 30 repetitions. For our Psi-HHL computations, we pick α of 60°. Figure 11(a) (and the accompanying Table XV of the Appendix) shows the results for ΔE, which is the difference between HHL (Psi-HHL) total energy and and the classical LCC value for the considered geometries. We find that Psi-HHL performs better than HHL in predicting correlation energies, especially on the extreme ends of our PEC when κ values are relatively larger than for those points around the equilibrium geometry. When we examine Fig. 11(b), we see that Psi-HHL performs consistently better than HHL. Furthermore, the spread in results across 30 repetitions follows a trend globally: it increases from 2.82- through 5.65-bohrs calculations. We recall that the correlation energies themselves decrease monotonically and by as much as an order of magnitude as we move from 2.82- to 5.65-bohrs geometries. Thus, although the condition numbers are comparable (for example, 374.93 and 371.38 for the 3.29- and the 4.71-bohrs cases, respectively), since the quantity to be captured (the correlation energy) itself is much smaller for the latter, we need to supply more shots to restrict the spread in PFD across repeats. However, since we keep the number of shots fixed throughout the PEC, we observe a larger spread in PFDs.

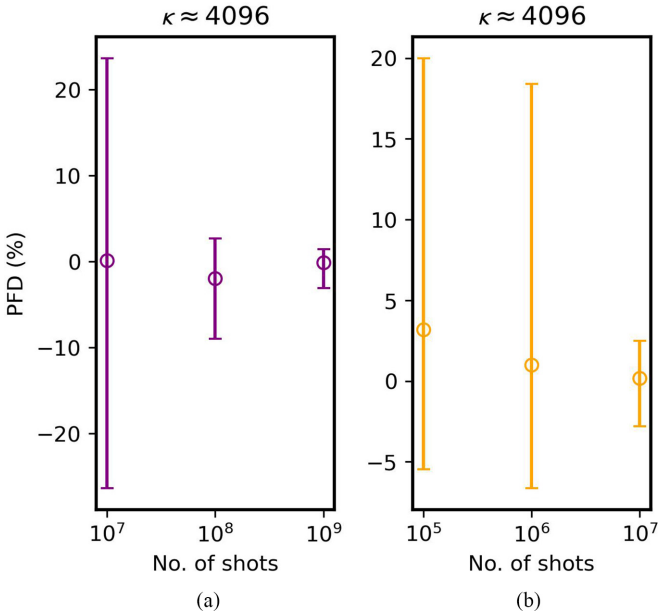


FIG. 8. Figure showing a comparison of the spread in PFDs as well as the average PFD (over 10 repetitions), obtained using HHL (a) and Psi-HHL (b), against a range of three different numbers of shots and for the case where A is of size 4×4, and for which $\kappa \approx 2^{12} = 4096$.

C. Scope of Psi-HHL

We begin by recalling the salient features of Psi-HHL:

(1) Superior performance in the large-κ regime, as discussed in Sec. II C, and its ability to yield accurate predictions, as indicated by our results from numerical simulations on toy matrices whose sizes range from 4×4 through 64×64.

(2) The approach works for extracting overlaps and expectation values (Sec. II E 2) involving $|x\rangle$. Psi-HHL also works for extracting features of a state of which $|x\rangle$ is a part, as expounded in Sec. II F with a representative example.

A feature of $|x\rangle$ relies on the properties of A and $|b\rangle$ since $|x\rangle$ is $A^{-1}|b\rangle$. This translates to the feature being affected by the norm of $||\,|x\rangle_{\text{un}}\,||$ (which in turn is impacted by the measurement probabilities on the HHL ancillary qubit) and the condition number of A. Thus, if the condition number of A is large, Psi-HHL fares substantially better in extracting this quantity (in fact, HHL in its traditional form does not even allow extracting a feature of $|x\rangle$ when κ is large, since obtaining $|x\rangle$ itself is problematic), whereas in low condition number regimes, HHL is superior.

We now comment on the scope of Psi-HHL in four parts: Requirements on A, the role of $\vec{b}$ in HHL and Psi-HHL results, the limitation versus usefulness of Psi-HHL in the low and large condition number regimes, respectively, and the role of the magnitude of the overlap itself in the feature to be extracted.

1. Requirements on A

We first address the requirements on A from Psi-HHL in particular. Then, we mention those requirements on A that Psi-HHL and HHL need in common.

We begin with a requirement specific to Psi-HHL: Psi-HHL proposes to efficiently capture a feature of the solution vector when the maximum and minimum eigenvalues of A are

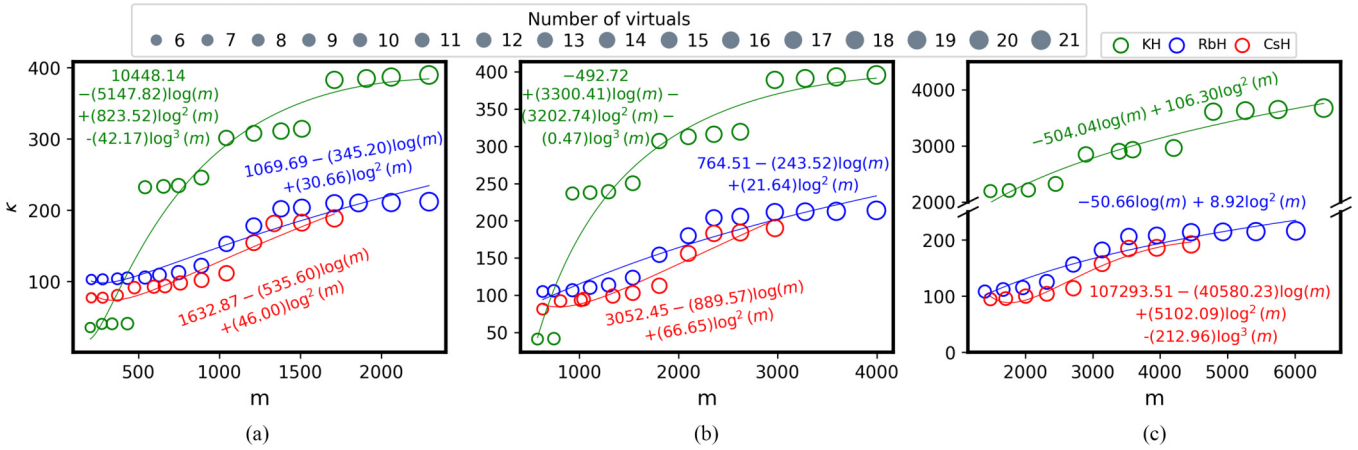


FIG. 9. Plots showing the increase in κ with A_{mol} matrix size, denoted as m, for the case of 6 (a), 8 (b), and 10 (c) fixed occupied orbitals in the Sapporo-DKH3-DZP-2012 basis set. The legend to the left at the top of the figure shows solid circles whose areas increase proportionally to the number of virtual orbitals considered.

well separated. This is because the approach is designed to leverage the fact that a low probability of obtaining outcome 1 on the ancilla qubit means that the probability of obtaining outcome 0 is large. Thus, an additional requirement on A from Psi-HHL is that its condition number be large for the approach to be useful. In such cases, Psi-HHL can efficiently (in the number of shots supplied for an experiment) extract a feature of $\vec{x}$.

We now move to requirements common to Psi-HHL and HHL: The Psi-HHL approach is built on the subtle notion of carrying out two HHL calculations and subtracting the resultant output signals to extract the correct signal, and thus requirements on A such as κ and s of the matrix having to scale polylogarithmically in system size (in order for an application to be useful via an HHL calculation) carries over from HHL to Psi-HHL. That is, although the HHL and the Psi-HHL approaches accommodate a wide range of applications in principle, the aforementioned constraints on A limit the range of problems to apply the HHL and Psi-HHL algorithms to.

2. The role of $\vec{b}$ on HHL and Psi-HHL results

While the numerical examples from earlier sections showed the efficacy of Psi-HHL, it is worth noting that the choice of $\vec{b}$ affects the quality of results via $P(0)$ in Eq. (10). To illustrate this point, we pick an example of a 2×2 matrix of the form $A = \begin{pmatrix} 2^{-10} & 0 \\ 0 & 1 \end{pmatrix}$ with κ thus set to 1024, and $\vec{b}$ being an extreme case at $\begin{pmatrix} 0 \\ 1 \end{pmatrix}$. Our results are presented in Fig. 12(a). We find that Psi-HHL does better than HHL always in terms of the spread in the PFD across 10 repetitions. However, when we consider the other extreme case, that is, $\vec{b} = \begin{pmatrix} 1 \\ 0 \end{pmatrix}$, $P(1) = 1$ always, and thus HHL gives excellent results while Psi-HHL performs marginally worse [we note that the y axis is between -0.6% and 0.4% for Fig. 12(b) as opposed to -200% to 100% for Fig.12(a)], as Fig. 12(b) shows.

3. Analysis of limitation of Psi-HHL in low-κ regime versus its usefulness in large-κ regime

We now comment on the limitation of Psi-HHL when κ is low, and contrast it with its usefulness when κ is large. For this purpose, we pick two representative examples: a simple toy matrix of size 2×2, where $A = \begin{pmatrix} 0.25 & 0.00 \\ 0.00 & 0.250025 \end{pmatrix}$ (thus, κ is 1.0001) and $\vec{b}$ is $\begin{pmatrix} 0.10 \\ 0.20 \end{pmatrix}$ for the low-κ example, and our 16×16 toy matrix from earlier sections with a condition number of 64.94 for the large-κ scenario. We set the number of required clock register qubits to 11 and 7 for the $\kappa = 1.0001$ and 64.94 cases, respectively. In the following paragraphs, we will discuss the results from our calculations, and then provide the rationale for the observed trends.

Figures 12(c) and 12(d) present the results for $\kappa = 1.0001$ and 64.94 cases, respectively. The minimum number of shots is set to 10^3 for Fig.12(c) and 10^4 for Fig. 12(d), since below that value, we sometimes run into the nan problem. It is immediately clear from the data points that as the number of shots increase, the spread in the average PFD across 10 repetitions decreases. This is unsurprising, and is consistent with results from earlier simulations. However, we observe that while the choice of α does not influence the average PFDs themselves for large κ case [Fig. 12(d)], it has a significant impact when $\kappa = 1.0001$ [Fig. 12(c)]. We verify that the observation is a result of insufficient number of shots by carrying out calculations while assuming that we are in the infinite shot limit. We find that in such a case, the PFDs are consistent with 0 for all $0^\circ < \alpha < 90^\circ$. This leads us to expect that in the $\kappa \to 1$ limit, both the PFD and the spread can depend on the mixing angle, α.

We now explain the reasoning behind the observations made in Figs. 12(c) and 12(d). We specifically focus on two aspects by scrutinizing the observed and theoretical probabilities: the PFD values themselves, which involve data that we average over 10 repetitions, and the spread in PFDs, for which we examine the range in the data from 10 repetitions. Examining the probabilities matter for analyzing the quality of

TABLE XIII. Table providing the minimum and maximum eigenvalues of the matrix A_{mol} of size $m \times m$, denoted in the table as $\lambda_{\text{min}}^{A_{\text{mol}}}$ and $\lambda_{\text{max}}^{A_{\text{mol}}}$, respectively, for KH, RbH, and CsH systems. n_o and n_v denote the number of occupied and virtual orbitals, respectively. $\lambda_{\text{min}}^{A_{\text{mol}}}$ and $\lambda_{\text{max}}^{A_{\text{mol}}}$ are in units of milli-Hartree.

Molecule	$n_o = 6$				$n_o = 8$				$n_o = 10$			
	m	n_v	$\lambda_{\text{min}}^{A_{\text{mol}}}$	$\lambda_{\text{max}}^{A_{\text{mol}}}$	m	n_v	$\lambda_{\text{min}}^{A_{\text{mol}}}$	$\lambda_{\text{max}}^{A_{\text{mol}}}$	m	n_v	$\lambda_{\text{min}}^{A_{\text{mol}}}$	$\lambda_{\text{max}}^{A_{\text{mol}}}$
	202	6	733.73	25918.07	580	8	730.05	29960.23	1484	10	127.91	280908.57
	274	7	731.91	29570.15	745	9	728.20	30271.74	1761	11	127.29	280909.73
	337	8	730.17	29604.25	932	10	127.95	30272.05	2046	12	126.64	280910.95
	432	9	728.35	29727.55	1110	11	127.33	30272.33	2451	13	120.90	280914.12
	541	10	128.01	29729.71	1296	12	126.71	30272.59	2900	14	98.56	280914.37
	655	11	127.38	29730.03	1540	13	120.92	30272.79	3393	15	96.78	281150.00
	748	12	126.76	29730.35	1808	14	98.59	30272.81	3794	16	95.80	281161.10
KH	889	13	120.98	29731.63	2100	15	96.83	30293.88	4203	17	94.84	281171.57
	1043	14	98.65	29731.69	2358	16	95.87	30304.25	4788	18	77.86	281200.60
	1213	15	96.89	29830.59	2624	17	94.89	30314.00	5265	19	77.45	281200.93
	1381	16	95.93	29834.52	2972	18	77.91	30317.70	5750	20	76.99	281201.42
	1510	17	94.96	29839.08	3278	19	77.50	30317.87	6427	21	76.56	281469.15
	1711	18	77.98	29854.11	3592	20	77.10	30318.05				
	1909	19	77.57	29854.20	3996	21	76.62	30328.12				
	2062	20	77.17	29854.30								
	2295	21	76.69	29894.66								
	209	6	108.95	11193.43	632	8	108.02	11330.03	1401	10	106.22	11489.85
	279	7	108.73	11200.46	744	9	107.07	11330.11	1673	11	102.72	11490.43
	370	8	108.02	11206.98	932	10	106.25	11330.19	1963	12	99.68	11491.02
	432	9	107.08	11207.05	1110	11	102.75	11330.84	2321	13	91.77	11503.07
	541	10	106.26	11207.13	1296	12	99.70	11331.49	2713	14	81.20	12694.32
	630	11	102.77	11207.95	1540	13	91.80	11339.56	3141	15	72.02	13125.74
	748	12	99.73	11208.41	1808	14	81.23	12533.58	3537	16	71.65	14777.36
	889	13	91.84	11216.40	2100	15	72.05	12963.58	3951	17	71.28	14822.69
RbH	1044	14	81.27	12410.75	2358	16	71.68	14614.13	4460	18	70.82	15148.61
	1213	15	72.10	12840.73	2624	17	71.31	14659.47	4932	19	70.64	15148.86
	1381	16	71.72	14490.85	2972	18	70.85	14988.70	5422	20	70.46	15149.12
	1510	17	71.35	14536.14	3278	19	70.67	14988.95	6013	21	70.05	15151.35
	1711	18	70.90	14865.97	3592	20	70.50	14989.21				
	1860	19	70.72	14866.22	3996	21	70.09	14991.44				
	2062	20	70.55	14866.47								
	2295	21	70.15	14868.69								
	209	6	119.60	9216.72	632	8	114.40	9306.70	1484	10	99.94	9447.99
	279	7	119.41	9216.73	812	9	101.30	9338.37	1711	11	98.74	9448.39
	370	8	114.52	9224.27	1016	10	99.97	9338.71	2007	12	94.46	9448.85
	475	9	101.35	9255.84	1044	11	98.81	9339.05	2321	13	90.73	9449.29
	595	10	100.02	9256.34	1339	12	94.53	9339.23	2714	14	82.84	9449.94
	664	11	98.86	9256.39	1540	13	90.80	9339.41	3141	15	63.54	10033.15
	759	12	94.61	9256.47	1808	14	82.91	9340.27	3537	16	63.38	11718.57
CsH	890	13	90.89	9256.59	2100	15	63.60	9923.04	3951	17	63.23	11763.91
	1044	14	83.03	9257.34	2358	16	63.44	11609.02	4461	18	62.86	12079.72
	1213	15	63.71	9840.84	2624	17	63.29	11654.36				
	1338	16	63.56	11526.12	2973	18	62.92	11966.65				
	1510	17	63.40	11571.52								
	1711	18	63.04	11884.73								

results because for HHL, the relevant probabilities impact the results via $||\,|x\rangle_{\text{un}}\,||$ [which is $\sqrt{P(1)}$] when we extract the feature, which we recall is given by $-\|\,|b\rangle_{\text{un}}\,\|^2\,\|\,|x\rangle_{\text{un}}\,\|\;\;|\langle b|x\rangle|$. On the other hand, for Psi-HHL, the quantity that decides the result is $\|\,|x'_m\rangle\,\|$ [which is $\sqrt{P'(1)}$].

We begin with the PFD values obtained from HHL and Psi-HHL calculations in Fig. 12(d), that is, the $\kappa = 64.94$ case. The incorrect PFD values predicted by HHL even at 1×10^9 shots can be backtracked to the discrepancy in the obtained $P(1)$ value of 0.007 upon averaging over 10 repetitions, as opposed to the theoretical value of 0.01 (obtained by using the relevant expression from Sec. II A). This means that one needs to supply more shots to be able to recover the correct $P(1)$. This is in stark contrast to the obtained $P'(1)$ of 0.7668 from HHL_2 (the HHL_1 module always has adequate shots in the large-κ regime, and thus we only need to focus on HHL_2)

TABLE XIV. Average PFDs and range of PFDs of HHL and Psi-HHL for Li_2 and KH molecules, both in Sapporo-DKH3-DZP-2012 basis set. The average PFDs are calculated over a range of 30 repetitions.

	Li_2		KH	
No. shots	HHL (PFD, range)	Psi-HHL (PFD, range)	HHL (PFD, range)	Psi-HHL (PFD, range)
5×10^2	(−7.68, 40.22)	(−2.79, 29.58)		
10^3	(−4.08, 19.80)	(−1.46, 8.34)	(nan, nan)	(−11.98, 106.87)
5×10^3	(−2.94, 8.89)	(−2.11, 7.56)		
10^4	(−0.58, 6.00)	(1.07, 4.47)	(0.34, 68.36)	(1.29, 44.70)
5×10^4			(0.73, 32.51)	(0.68, 16.78)
10^5			(0.73, 17.00)	(0.72, 9.02)
5×10^5			(2.65, 10.59)	(1.11, 5.65)
10^6			(3.99, 5.09)	(0.22, 4.05)

that is comparable to the theoretical value of 0.7674. In fact, the observed (calculated using simulation) and the theoretical $P'(1)$ values are the very same at 0.7668 and 0.7674, respectively, even with 10^7 shots.

Next, we discuss the spread in the PFD values across 10 repetitions observed in Fig. 12(d). For this case, we see that the spread in $P(1)$ is very low, and is between 0.0070511 and 0.0070574, and that for $P'(1)$ is between 0.76676 and 0.76678. Thus, the PFDs also show minimal spread in the plots.

We now move to the PFD values obtained from HHL and Psi-HHL computations for the $\kappa = 1.0001$ case, with the results presented in Fig. 12(c). Here, the theoretical value of $P(0)$ is 0.00015 whereas $P(0)$ from our simulation is 0.0171 even at 10^7 shots. On the other hand, $P(1)$ is 0.999 and 0.982 for theoretical and simulated values, respectively.

We check the spread in the PFD values across 10 repetitions for the data pertaining to Fig. 12(c), for 10^7 shots case. Here too, the $P(0)$ values lie in a narrow range (between 0.001137 and 0.001166), as do the $P'(1)$ values (between 0.99883 and 0.99886), hence giving the low spread in PFDs.

Although the considerations above place a limitation on Psi-HHL in the low condition number regimes, this is unlikely to be a limiting factor to the scope of problems that one can apply the algorithm to in practice. This is because for sufficiently large system sizes where classical computers struggle and where Psi-HHL is expected to become useful, it is very unlikely that κ would be small. Furthermore, one could always begin with HHL and check the output histograms for both 0 and 1, and opt for HHL_2 if the former is sufficiently small (with "sufficiently" being decided by the application of interest) or go ahead with the HHL computation if the former is sufficiently large.

For completeness, we discuss the $\kappa = 1$ extreme case since $C/\lambda_i = 1 \; \forall \; i$, it is easy to verify that the wrong signal described in Eq. (20) as well as the wrong part of the mixed signal from Eq. (22) are zero, thus leaving behind only the correct signal. The additional cosine term in the correct part of the mixed signal is canceled out due to the sine and the cotangent present in Eq. (23).

4. The role of the magnitude of the overlap to be extracted

We discussed the roles of $\vec{b}$ and the role of the normalization factor associated with the solution vector on the quality of our results when we extract a feature. We finally move to the case of the overlap value itself being small. This analysis is common for HHL and Psi-HHL. For this purpose, we consider a simple toy calculation, where we evaluate the overlap $|\langle 0|(a|0\rangle + b|1\rangle)|$ using the HOM circuit, with 1000 shots and average each of our results over 20 repetitions. a is varied from 0.26 to 0.99 (below 0.26, we run into the nan issue discussed earlier). This exercise also verifies the trend in Fig. 11(b) (see Fig. 13). We conclude from the analysis that if the value of the overlap itself is small, a user needs to supply more shots to extract the feature even if the other aforementioned aspects such as $\vec{b}$ and κ are conducive.

TABLE XV. Table providing the details on the condition numbers (κ), the average total energy, the energy difference (ΔE) between the total HHL (Psi-HHL) energy and classical value of the LCCSD total energy and the average PFDs over 30 repetitions with respect to the bond length of KH molecule. All the energies are in units of milli-Hartree. "Eq" denotes the equilibrium geometry.

Bond length (bohrs)	κ	HHL			Psi-HHL		
		Total energy	ΔE	PFD	Total energy	ΔE	PFD
2.82	393.21	−598878.025	−0.124	−3.92	−598877.968	−0.068	−2.48
3.29	374.93	−598940.871	−0.086	−3.84	−598940.844	−0.059	2.31
3.76	367.32	−598967.447	−0.003	−1.96	−598967.447	−0.004	−0.26
4.23 (Eq)	365.40	−598975.800	0.007	1.46	−598975.802	0.004	0.34
4.71	371.38	−598974.517	−0.010	−10.00	−598974.509	−0.007	1.39
5.18	385.16	−598968.421	−0.001	−0.44	−598968.419	0.000	−0.08
5.65	373.56	−598960.199	−0.001	−0.41	−598960.196	0.000	0.26

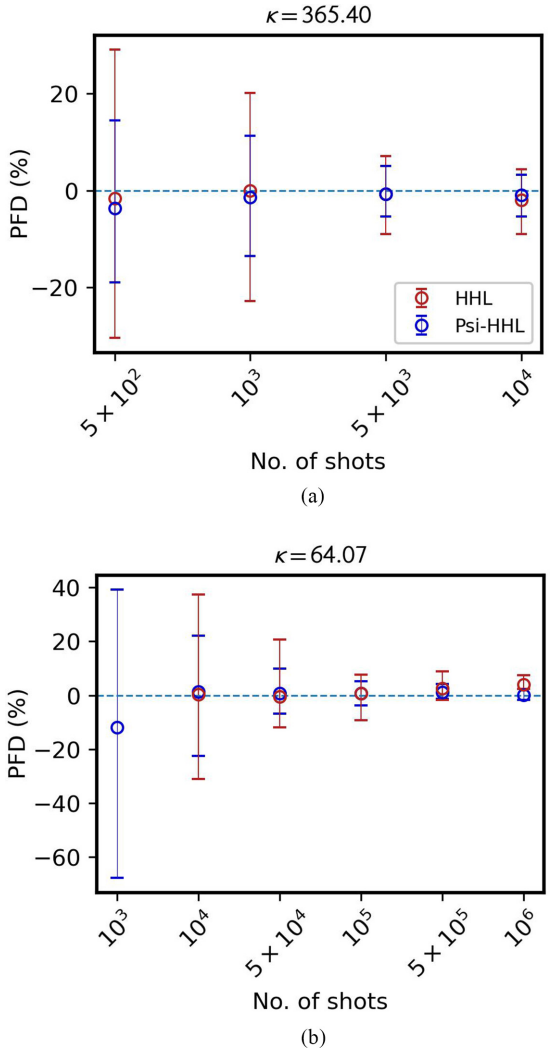


FIG. 10. Figure showing a comparison of the performance of HHL and Psi-HHL approaches, via PFDs versus number of shots (denoted in the figure as "No. of shots"), for two representative molecules, Li_2 (a) and KH (b). The center of each unfilled circle represents the average PFD over a range of 30 repetitions. Each Li_2 calculation involves evaluating a 21-qubit circuit, with the A matrix size being 64×64 (κ of 64.07), while for KH, we evaluate a 26-qubit circuit involving an A matrix size of 256×256 (κ of 365.40). The zero PFD value is marked with a horizontal line for ease of visualization.

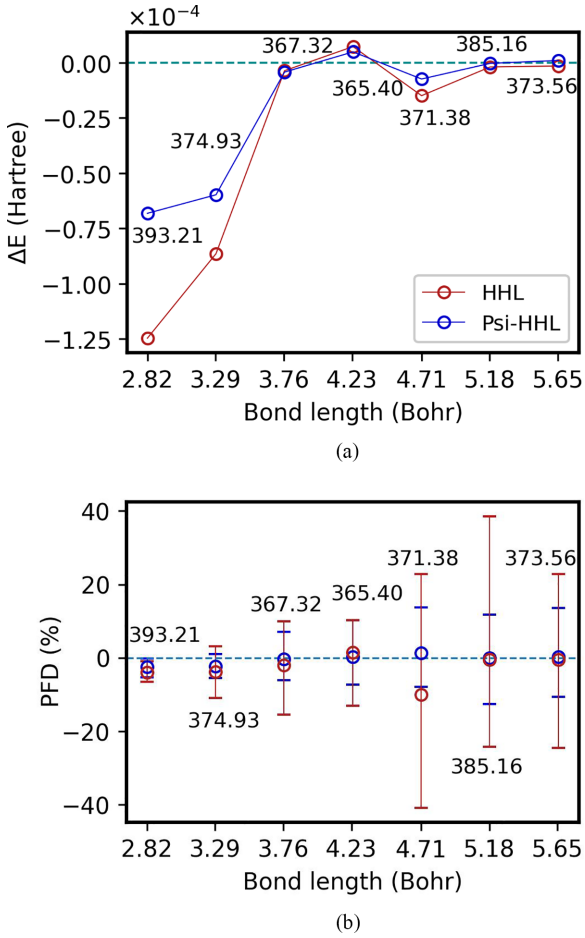


FIG. 11. Figure illustrating the energy difference (ΔE) between the total HHL/Psi-HHL energy and the classical value of the LCCSD total energy (a) and PFDs versus bond lengths (b) of the KH molecule obtained from HHL and Psi-HHL methods (26-qubit calculations involving A matrix size of 256×256; red and blue circles indicate HHL and Psi-HHL calculations, respectively, averaged over 30 repetitions and with 50 000 shots). The associated value of κ is shown above or below each data point.

IV. CONCLUSION

We propose the Psi-HHL algorithm to efficiently handle problems involving A matrices with large condition numbers (κ). The approach involves postselecting 0 in HHL (the "wrong signal"), followed by postselecting 1 from an HHL-like circuit that contains an additional mixing 2×2 unitary (the "mixed signal"), and taking the difference between the wrong and the mixed signals to extract the correct signal.

We present arguments to show that the complexity of Psi-HHL is optimal in condition number for large κ regimes; the complexity of the algorithm scales as $\mathcal{O}(\kappa)$. This is an improvement over earlier approaches in the literature, such as HHL with amplitude amplification (scales quadratically, and incurs several additional gates due to its iterative nature; Psi-HHL practically involves executing two circuits of almost the same depth as HHL) and HHL with variable time amplitude amplification (scales as $\kappa \log^3 \kappa$). It is also important to note that while the optimal κ behavior can be recovered using a discrete quantum adiabatic approach based quantum linear solver algorithm [12], we achieve the same result using Psi-HHL, which is a simple modification to the HHL algorithm. We also discuss the case of applying Psi-HHL to singular matrices.

We apply our method to different toy matrices, where we systematically vary the condition number all the way to about 1×10^6 and keeping the number of shots fixed to 1×10^6 for each of the computations, and show that while HHL fails beyond a certain value of κ, Psi-HHL continues to predict good results that we quantify via percentage fraction difference (PFD) relative to the classical value as well as via spread in the PFD across many repetitions. We also demonstrate the performance of our proposed Psi-HHL approach for quantum chemistry examples with up to 26-qubit computations, and

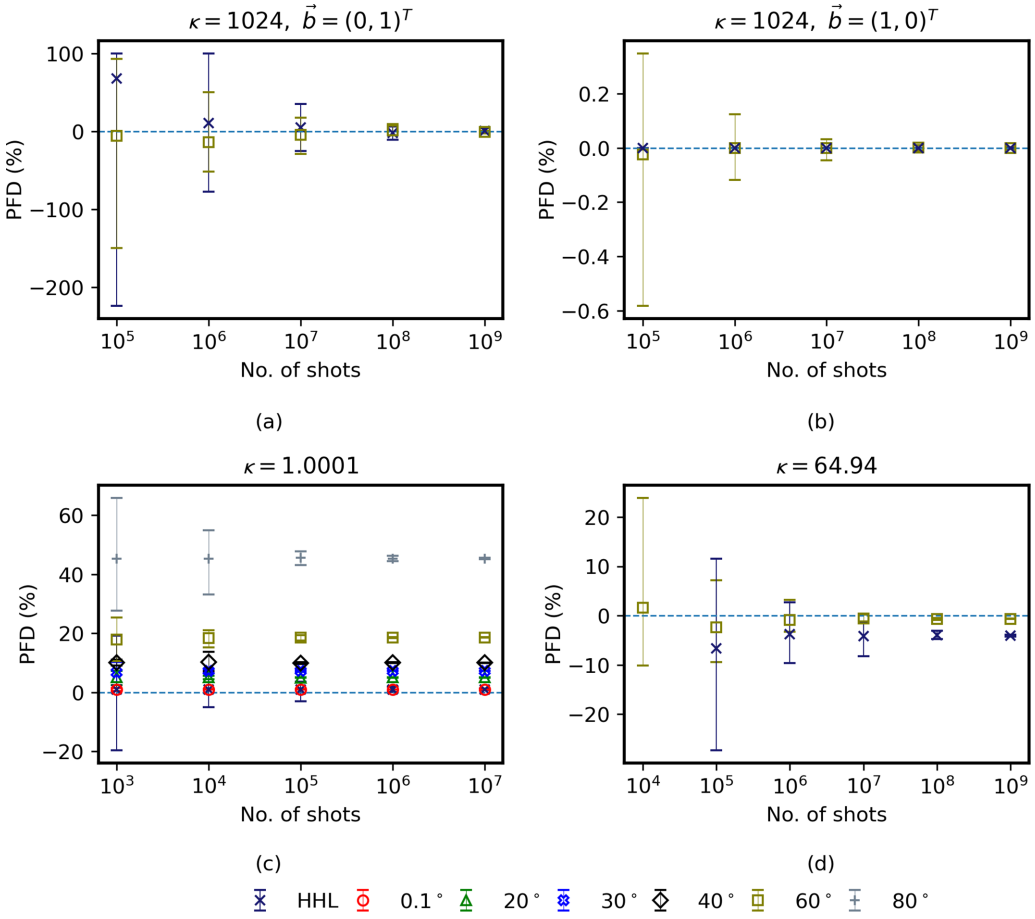


FIG. 12. Figures presenting our results for (a) a 2×2 matrix with $\vec{b} = \binom{0}{1}$, while (b) considers the other extreme case of $\vec{b} = \binom{1}{0}$. (c) Presents HHL and Psi-HHL results for a 2×2 matrix whose $\kappa = 1.0001$, whereas (d) gives results for Psi-HHL calculations on a 16×16 matrix whose κ is 64. (a), (b) Illustrate the role of $\vec{b}$ in influencing a result, whereas the third indicates the limitation in low-κ regime. The last subfigure is an example of the opposite of the third, where HHL yields incorrect PFDs with low spread. In all the subfigures, each data point is an average over 10 repetitions.

we once again find that Psi-HHL yields better quality results in much fewer number of shots. En route, we also carry out a qualitative analysis to check suitability of treating LCC equations using the HHL algorithm.

We anticipate that our work will pave the way for development of efficient quantum algorithms with Psi-HHL integrated into it as an algorithmic primitive.

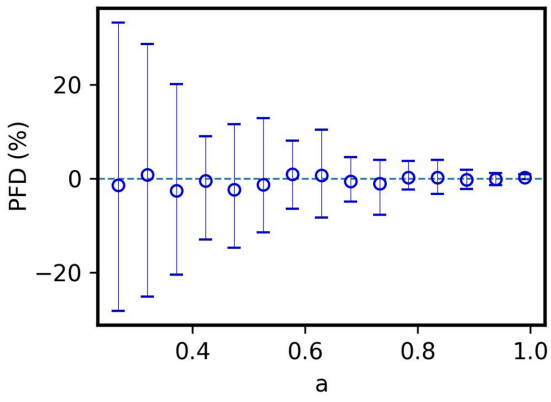


FIG. 13. Figure showing average PFDs and range of PFDs (over 20 repetitions) for different values of a for the overlap $|\langle 0|(a|0\rangle + b|1\rangle)|$. We fix the number of shots to 1000 for generating all of the data.

ACKNOWLEDGMENTS

We acknowledge National Supercomputing Mission (NSM) for providing computing resources of 'PARAM Siddhi-AI', under National PARAM Supercomputing Facility (NPSF), C-DAC, Pune, and supported by the Ministry of Electronics and Information Technology (MeitY) and Department of Science and Technology (DST), Government of India. V.S.P. thanks Prof. A. Harrow for a very fruitful discussion on HHL as well as HHL-LCC. V.S.P. and A.J. thank Dr. S. Roy for nice discussions on complexity. P.B.T. thanks Prof. D. Mukherjee for useful discussions on the quantum chemical sections of the work. V.S.P. and P.B.T. thank their group members for carefully reading the manuscript. K.S. acknowledges support from Quantum Leap Flagship Program (Grant No. JPMXS0120319794) from Ministry of Education, Culture, Sports, Science and Technology (MEXT), Japan;

Center of Innovations for Sustainable Quantum AI (Grant No. JPMJPF2221) from Japan Science and Technology Agency (JST), Japan; and Grants-in-Aid for Scientific Research C (Grant No. 21K03407) and for Transformative Research Area B (Grant No. 23H03819) from Japan Society for the Promotion of Sciences (JSPS), Japan.

APPENDIX A: PSI-HHL FOR OVERLAP CALCULATION WITH SIGN INFORMATION

1. Extracting the wrong signal

We briefly outline our protocol for the circuit given in Figs. 4(a) and 4(b) below. We assume here and in the subsequent subsections with no loss of generality that the eigenvalues λ_i are precisely captured with adequate number of QPE clock register qubits n_r. We start with Fig. 4(a) which helps to calculate $\mathrm{Re}(\langle b|x_{\mathrm{w}}\rangle)$ and $\mathrm{Im}(\langle b|x_{\mathrm{w}}\rangle)$.

(1) We begin with $|0\rangle \otimes |0\rangle \otimes |0^{n_r}\rangle \otimes |b\rangle$, and upon applying $H \otimes I^{\otimes(1+n_r+n_b)}$, we get $\frac{1}{\sqrt{2}}(|0\rangle + |1\rangle) \otimes |0\rangle \otimes |0^{n_r}\rangle \otimes |b\rangle$.

(2) This is followed by the operation $|0\rangle\langle 0| \otimes I + |1\rangle\langle 1| \otimes \mathrm{HHL}_1$(no measurement and postselection), which results in

$$\frac{1}{\sqrt{2}}|0\rangle \otimes |0\rangle \otimes |0^{n_r}\rangle \otimes |b\rangle + \frac{1}{\sqrt{2}}|1\rangle \otimes \left(\sum_i b_i \sqrt{1-\frac{C^2}{\lambda_i^2}}\,|0\rangle + b_i \frac{C}{\lambda_i}|1\rangle\right) \otimes |0^{n_r}\rangle \otimes |v_i\rangle\,.$$

(3) Measuring the second qubit from the top and postselecting the outcome 0, we get the state vector

$$\frac{1}{\sqrt{2\mathfrak{d}}}|0\rangle \otimes |0\rangle \otimes |0^{n_r}\rangle \otimes |b\rangle + \frac{1}{\sqrt{2\mathfrak{d}}}|1\rangle \otimes |0\rangle \otimes |0^{n_r}\rangle \otimes |x_{\mathrm{w}}\rangle\,,$$

where $1/\sqrt{\mathfrak{d}}$ is the normalization factor after measurement and $\mathfrak{d} = \frac{1}{2}(\| |b\rangle \|^2 + \| |x_{\mathrm{w}}\rangle \|^2) = \frac{1}{2}(1 + \| |x_{\mathrm{w}}\rangle \|^2)$.

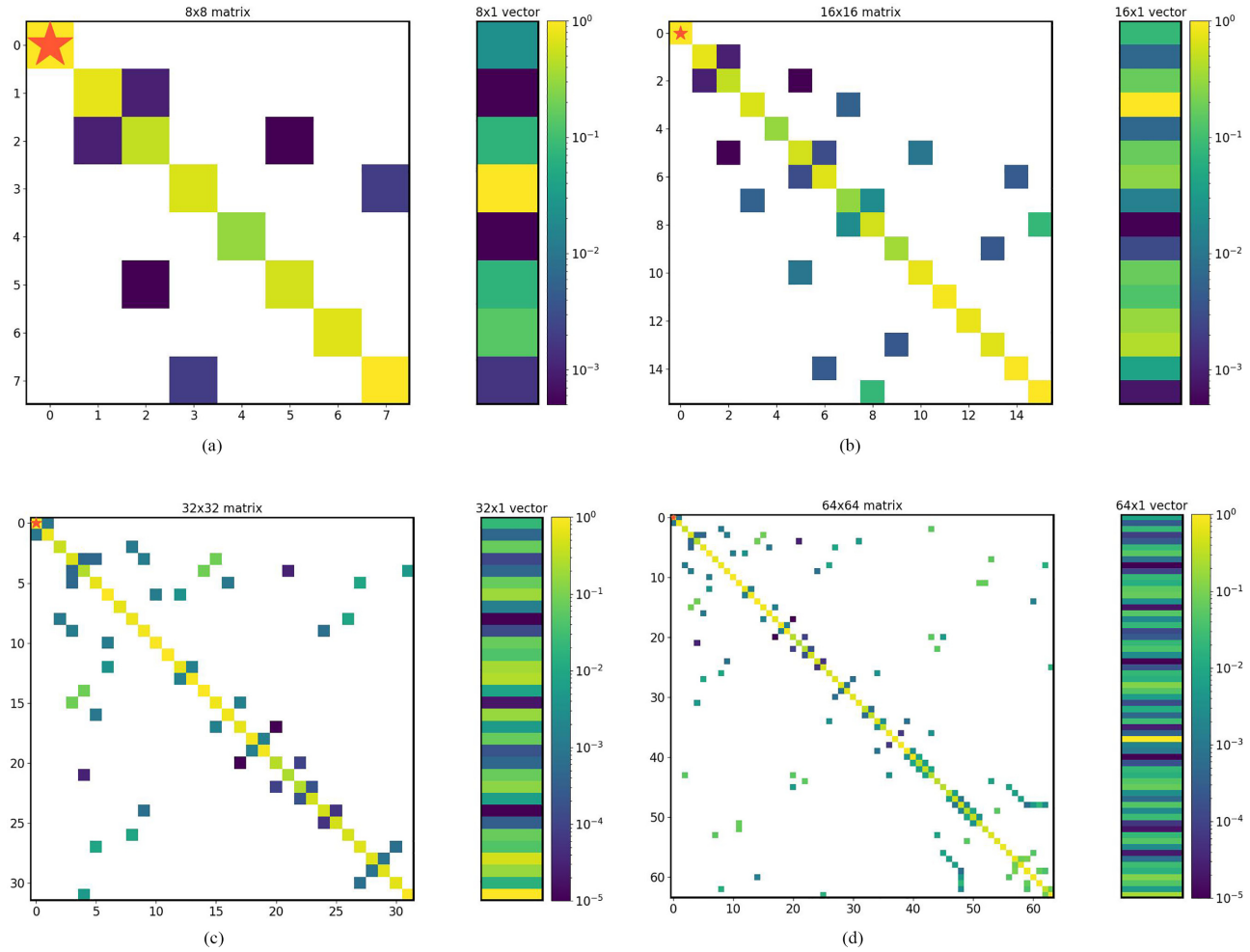
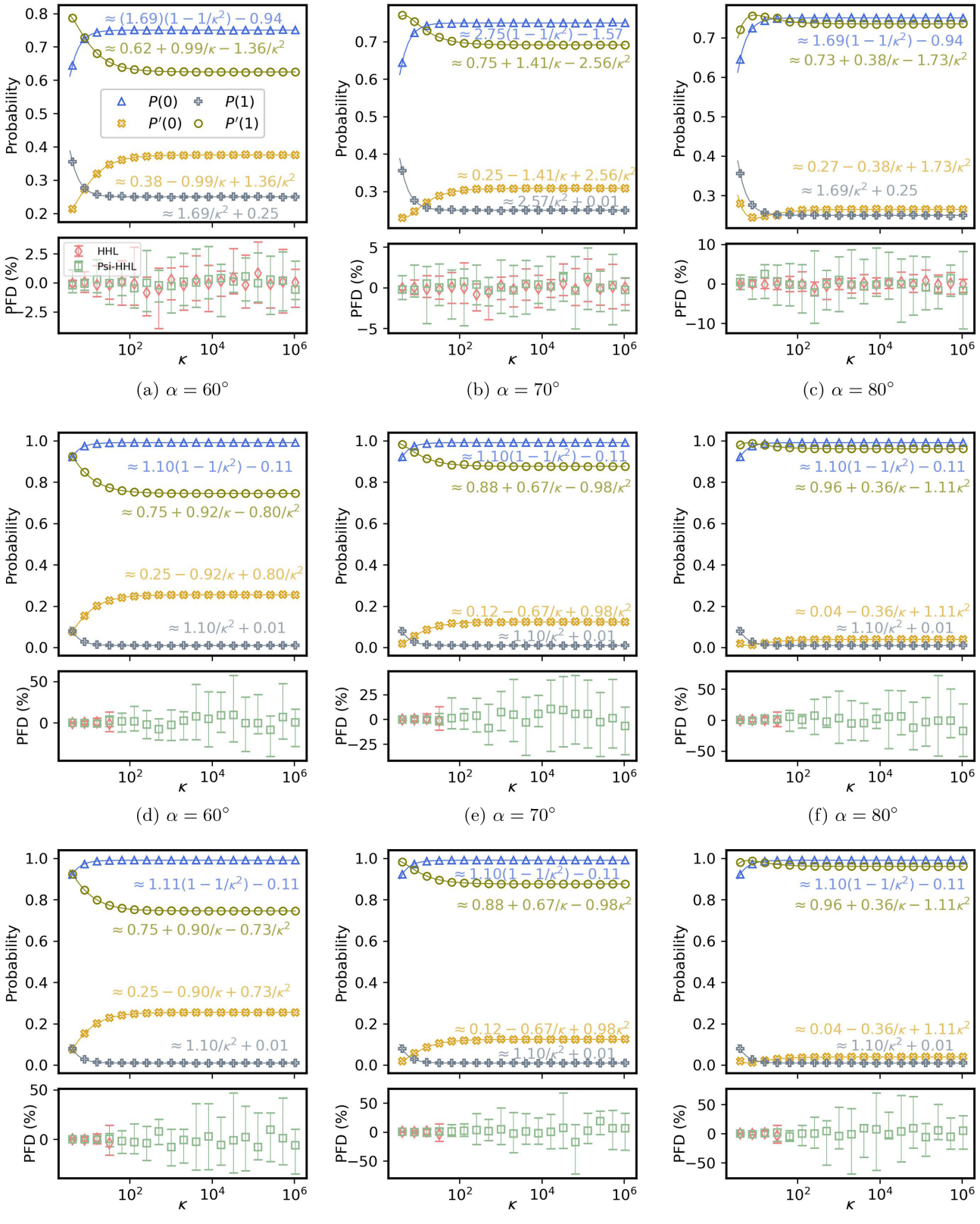


FIG. 14. Our choices for (a) 8×8, (b) 16×16, (c) 32×32, and (d) 64×64 toy A matrices and unnormalized $\vec{b}$ for comparing the performance of HHL and the Psi-HHL algorithms. The cell with a star symbol denotes the matrix element with variable n_r (the number of clock register qubits from the HHL circuit), which sets κ. A white cell denotes a zero matrix element.

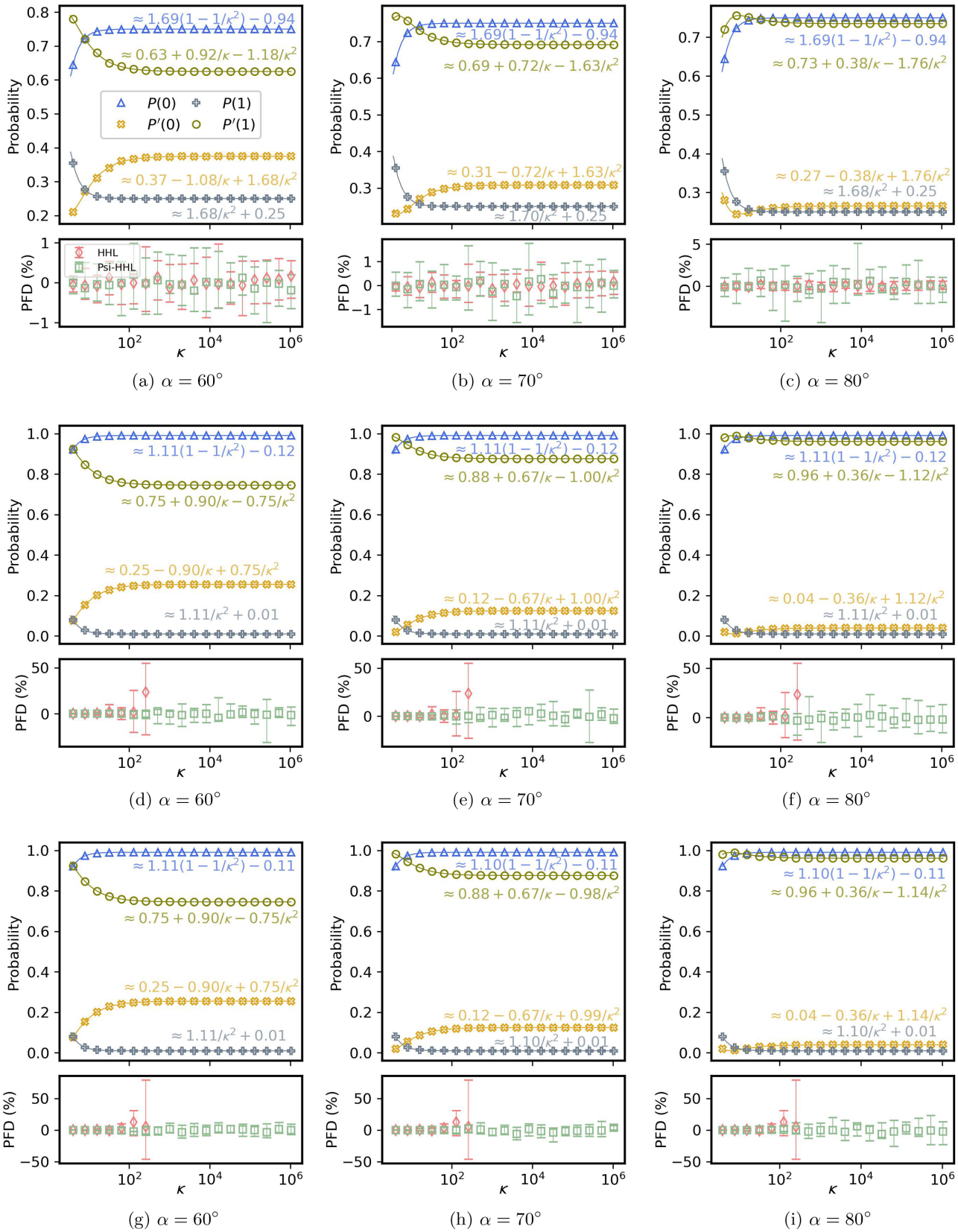


(a) $\alpha = 60°$ (b) $\alpha = 70°$ (c) $\alpha = 80°$

(d) $\alpha = 60°$ (e) $\alpha = 70°$ (f) $\alpha = 80°$

(g) $\alpha = 60°$ (h) $\alpha = 70°$ (i) $\alpha = 80°$

FIG. 15. Subfigures presenting the average probabilities of HHL and Psi-HHL with varying condition number κ of A, for 4×4 matrices and using 10^5 shots throughout. (a)–(c) Consider the case where A is diagonal and $\vec{b}$ is in equal superposition. (d)–(f) Consider the case where A is diagonal and $\vec{b}$ is in unequal superposition, and (g)–(i) consider the case where A is not diagonal, and $\vec{b}$ is in unequal superposition. Each data point is generated by taking the average over 10 repetitions.

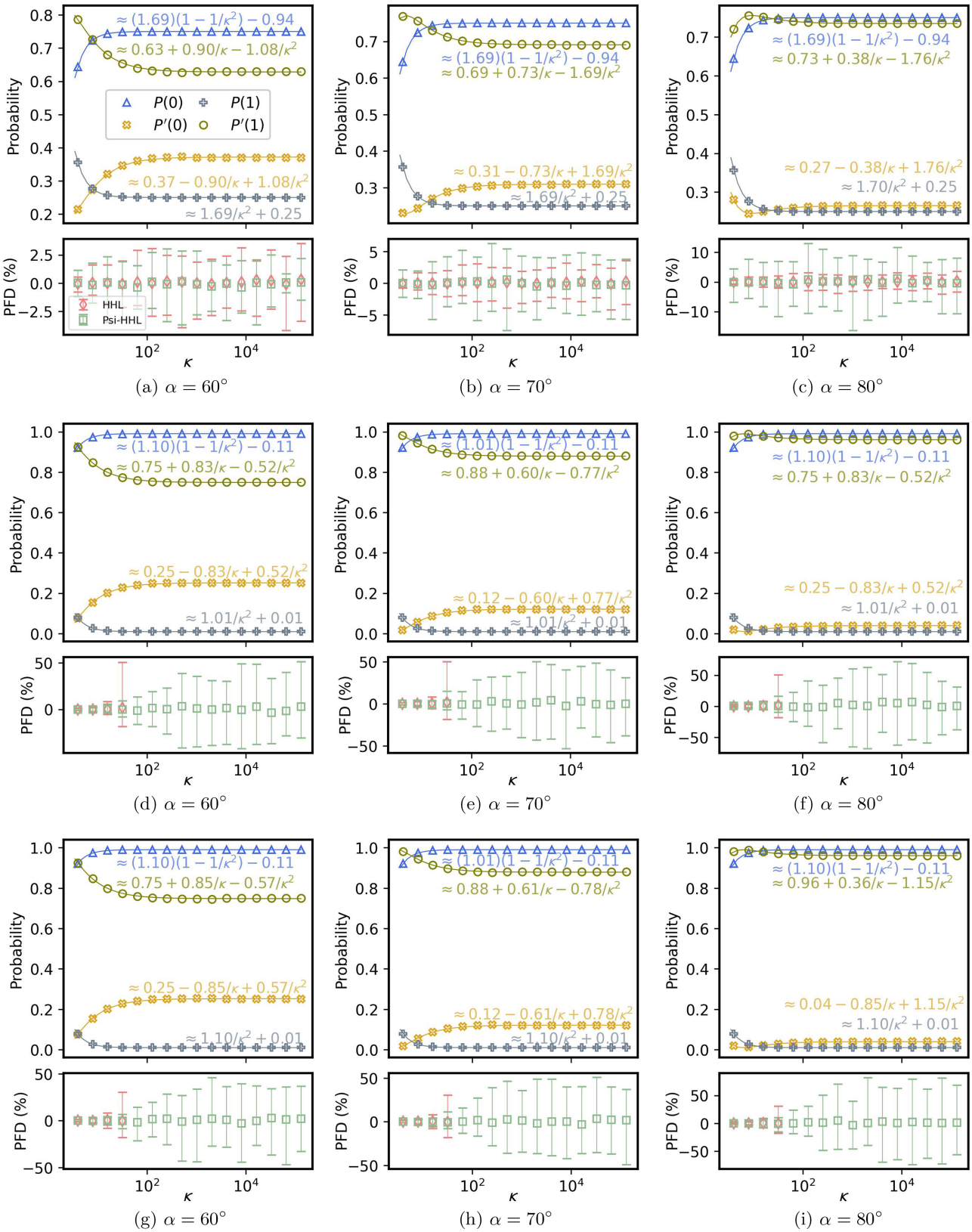


(a) $\alpha = 60°$ (b) $\alpha = 70°$ (c) $\alpha = 80°$

(d) $\alpha = 60°$ (e) $\alpha = 70°$ (f) $\alpha = 80°$

(g) $\alpha = 60°$ (h) $\alpha = 70°$ (i) $\alpha = 80°$

FIG. 16. Subfigures presenting the average probabilities of HHL and Psi-HHL with varying condition number κ of A, for 4×4 matrices and using 10^6 shots throughout. (a)–(c) Consider the case where A is diagonal and $\vec{b}$ is in equal superposition. (d)–(f) Consider the case where A is diagonal and $\vec{b}$ is in unequal superposition, and (g)–(i) consider the case where A is not diagonal, and $\vec{b}$ is in unequal superposition. Each data point is generated by taking the average over 10 repetitions.

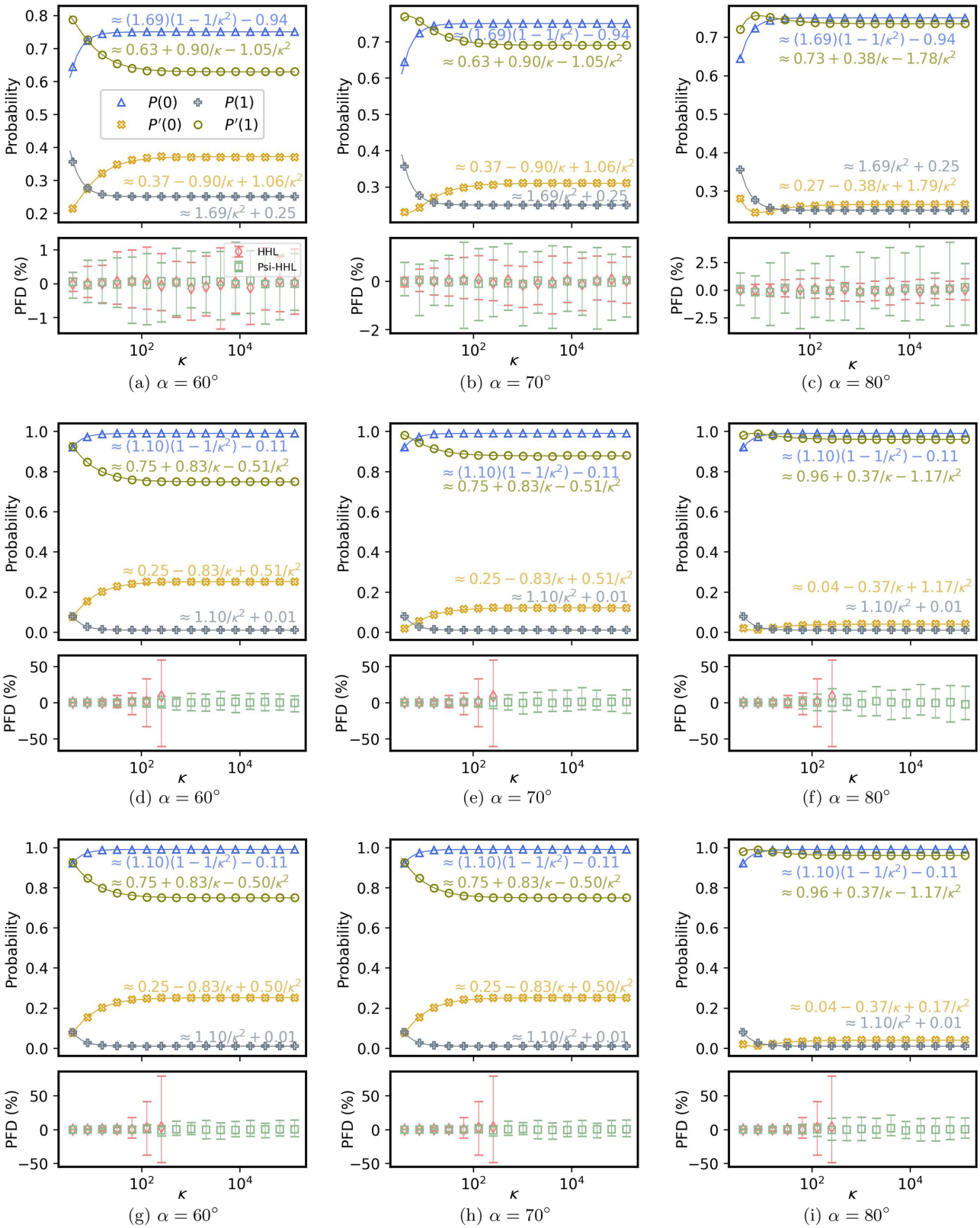


(a) $\alpha = 60°$ (b) $\alpha = 70°$ (c) $\alpha = 80°$

(d) $\alpha = 60°$ (e) $\alpha = 70°$ (f) $\alpha = 80°$

(g) $\alpha = 60°$ (h) $\alpha = 70°$ (i) $\alpha = 80°$

FIG. 17. Subfigures presenting the average probabilities of HHL and Psi-HHL with varying condition number κ of A, for 4×4 matrices and using 10^5 shots throughout. (a)–(c) Consider the case where A is diagonal and $\vec{b}$ is in equal superposition. (d)–(f) Consider the case where A is diagonal and $\vec{b}$ is in unequal superposition, and (g)–(i) consider the case where A is not diagonal and $\vec{b}$ is in unequal superposition. Each data point is generated by taking the average over 50 repetitions.

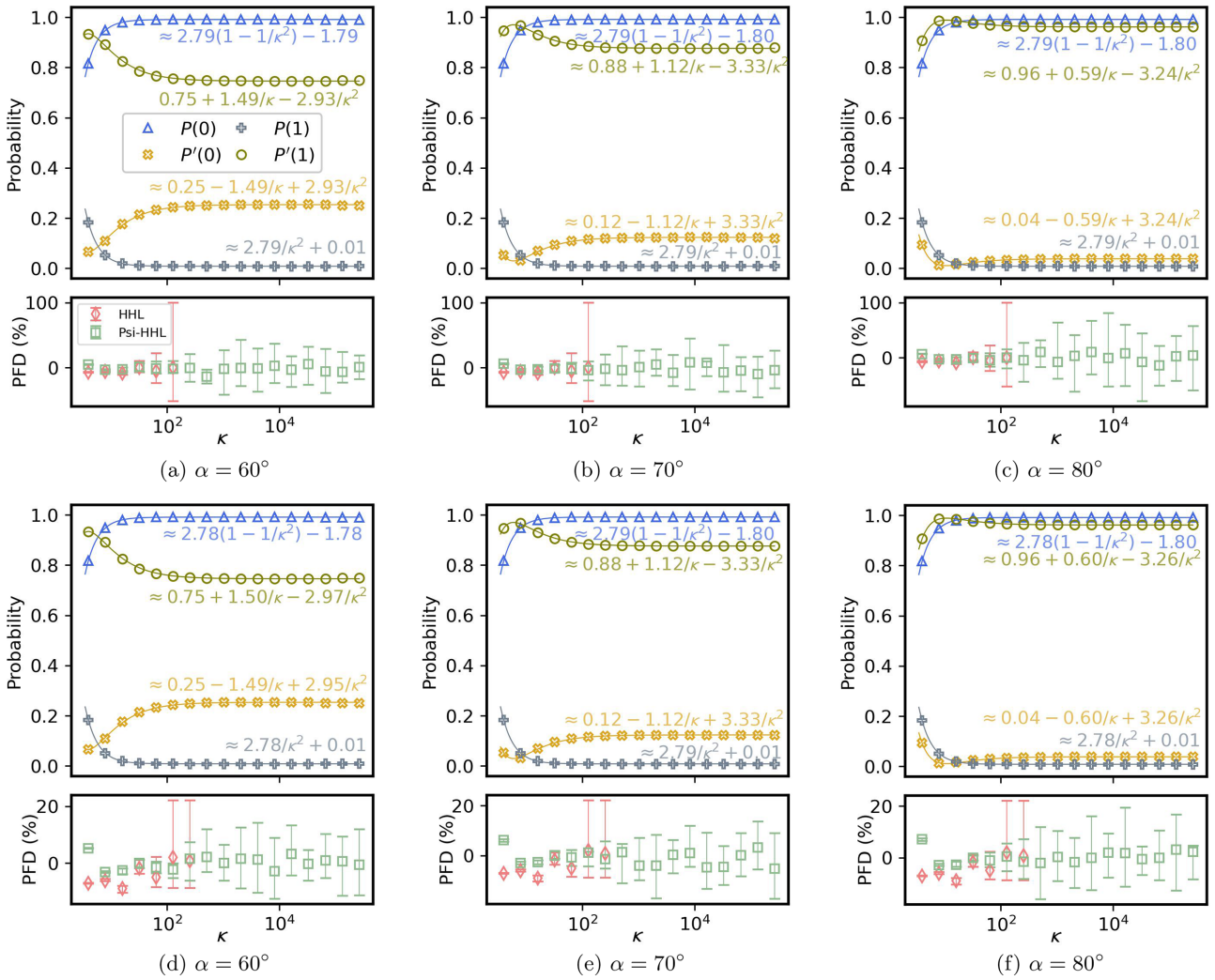


(a) $\alpha = 60°$ (b) $\alpha = 70°$ (c) $\alpha = 80°$

(d) $\alpha = 60°$ (e) $\alpha = 70°$ (f) $\alpha = 80°$

(g) $\alpha = 60°$ (h) $\alpha = 70°$ (i) $\alpha = 80°$

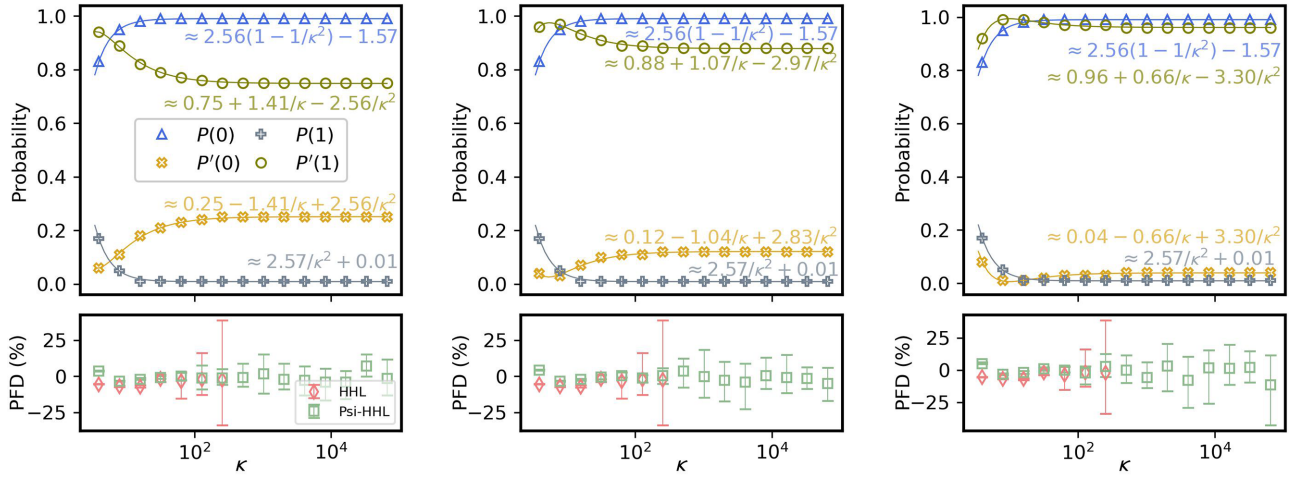
FIG. 18. Subfigures presenting the average probabilities of HHL and Psi-HHL with varying condition number κ of A, for 4×4 matrices and using 10^6 throughout. (a)–(c) Consider the case where A is diagonal, and $\vec{b}$ is in equal superposition. (d)–(f) Consider the case where A is diagonal and $\vec{b}$ is in unequal superposition, and (g)–(i) consider the case where A is not diagonal, and $\vec{b}$ is in unequal superposition. Each data point is generated by taking the average over 50 repetitions.



(a) $\alpha = 60°$ (b) $\alpha = 70°$ (c) $\alpha = 80°$

(d) $\alpha = 60°$ (e) $\alpha = 70°$ (f) $\alpha = 80°$

FIG. 19. Subfigures presenting the average probabilities, PFDs, and range of PFDs of HHL and Psi-HHL with varying condition number κ of A, for 8×8 matrices using 10^5 shots (a)–(c) and using 10^6 (d)–(f). In all of the examples, A is chosen to be a nondiagonal matrix and $\vec{b}$ is set in an unequal superposition. Each data point is an average over 10 repetitions.



(a) $\alpha = 60°$ (b) $\alpha = 70°$ (c) $\alpha = 80°$

FIG. 20. Subfigures presenting the average probabilities, PFDs, and range of PFDs of HHL and Psi-HHL with varying condition number κ of A, for 16×16 matrices and using 10^6 shots throughout. In all of the examples, A is chosen to be a nondiagonal matrix and $\vec{b}$ is set in an unequal superposition. Each data point is an average over 10 repetitions.

(4) Acting the resulting state upon by $H \otimes I^{\otimes(1+n_r+n_b)}$, we obtain

$$\frac{1}{2\sqrt{\mathfrak{b}}}[|0\rangle \otimes |0\rangle \otimes |0^{n_r}\rangle \otimes (|b\rangle + |x_{\rm w}\rangle) + |1\rangle \otimes |0\rangle \otimes |0^{n_r}\rangle \otimes (|b\rangle - |x_{\rm w}\rangle)].$$

(5) The probability of measuring 0 on the first qubit from the top is

$$\begin{aligned}\mathcal{P}_R(0) &= \left\| \frac{1}{2\sqrt{\mathfrak{b}}}(|b\rangle + |x_{\rm w}\rangle) \right\|^2 \\ &= \frac{1}{2}\left(1 + \frac{2\,\mathrm{Re}(\langle b\,|x_{\rm w}\rangle)}{1 + \|\,|x_{\rm w}\rangle\,\|^2}\right).\end{aligned}$$

Similarly, the introduction of $S^\dagger$ gate in the circuit in Fig. 4(a) helps us find

$$\begin{aligned}\mathcal{P}_I(0) &= \left\| \frac{1}{2\sqrt{\mathfrak{b}}}(|b\rangle - i\,|x_{\rm w}\rangle) \right\|^2 \\ &= \frac{1}{2}\left(1 + \frac{2\,\mathrm{Im}(\langle b\,|x_{\rm w}\rangle)}{1 + \|\,|x_{\rm w}\rangle\,\|^2}\right).\end{aligned}$$

Through the last these expressions, we find that

$$\langle b|x_{\rm w}\rangle = \{[2\mathcal{P}_R(0) - 1] + i[2\mathcal{P}_I(0) - 1]\}\mathfrak{b}. \tag{A1}$$

2. Extracting the mixed signal

Now we give the protocol which helps us to calculate $\mathrm{Re}(\langle b\,|x'_{\rm m}\rangle)$ and $\mathrm{Im}(\langle b\,|x'_{\rm m}\rangle)$ from Fig. 4(b).

(1) We begin with $|0\rangle \otimes |0\rangle \otimes |0^{n_r}\rangle \otimes |b\rangle$, and upon applying $H \otimes I^{\otimes(1+n_r+n_b)}$, we get $\frac{1}{\sqrt{2}}(|0\rangle + |1\rangle) \otimes |0\rangle \otimes |0^{n_r}\rangle \otimes |b\rangle$.

(2) This is followed by the operation $|0\rangle\langle 0| \otimes I + |1\rangle\langle 1| \otimes \mathrm{HHL}_2$(no measurement and postselection), which results in

$$\begin{aligned}&\frac{1}{\sqrt{2}}\,|0\rangle \otimes |0\rangle \otimes |0^{n_r}\rangle \otimes |b\rangle + \frac{1}{\sqrt{2}}\,|1\rangle \otimes \left[\left(\sum_i b_i\sqrt{1 - \frac{C^2}{\lambda_i^2}}\cos(\alpha) - b_i\frac{C}{\lambda_i}\sin(\alpha)\right)|0\rangle\right. \\ &\left.+\left(\sum_i b_i\sqrt{1 - \frac{C^2}{\lambda_i^2}}\sin(\alpha) + b_i\frac{C}{\lambda_i}\cos(\alpha)\right)|1\rangle\right] \otimes |0^{n_r}\rangle \otimes |\nu_i\rangle\,.\end{aligned}$$

(3) Then, we apply the operation $(|0\rangle\langle 0| \otimes X + |1\rangle\langle 1| \otimes I) \otimes I^{\otimes(n_r+n_b)}$ on the first and second qubits from the top and get

$$\begin{aligned}&\frac{1}{\sqrt{2}}\,|0\rangle \otimes |1\rangle \otimes |0^{n_r}\rangle \otimes |b\rangle + \frac{1}{\sqrt{2}}\,|1\rangle \otimes \left[\left(\sum_i b_i\sqrt{1 - \frac{C^2}{\lambda_i^2}}\cos(\alpha) - b_i\frac{C}{\lambda_i}\sin(\alpha)\right)|0\rangle\right. \\ &\left.+\left(\sum_i b_i\sqrt{1 - \frac{C^2}{\lambda_i^2}}\sin(\alpha) + b_i\frac{C}{\lambda_i}\cos(\alpha)\right)|1\rangle\right] \otimes |0^{n_r}\rangle \otimes |\nu_i\rangle\,.\end{aligned}$$

(4) Measuring the second qubit from the top and postselecting the outcome 1, we get the state vector

$$\frac{1}{\sqrt{2\beta}}(|0\rangle \otimes |1\rangle \otimes |0^{n_r}\rangle \otimes |b\rangle + |1\rangle \otimes |1\rangle \otimes |0^{n_r}\rangle \otimes |x'_{\rm m}\rangle),$$

where $1/\sqrt{\beta}$ is the normalization factor after measurement and $\beta = \frac{1}{2}(\|\,|b\rangle\,\|^2 + \|\,|x'_{\rm m}\rangle\,\|^2) = \frac{1}{2}(1 + \|\,|x'_{\rm m}\rangle\,\|^2)$.

(5) Acting the resulting state upon by $H \otimes I^{\otimes(1+n_r+n_b)}$, we obtain

$$\begin{aligned}&\frac{1}{2\sqrt{\beta}}[|0\rangle \otimes |1\rangle \otimes |0^{n_r}\rangle \otimes (|b\rangle + |x'_{\rm m}\rangle) \\ &+ |1\rangle \otimes |1\rangle \otimes |0^{n_r}\rangle \otimes (|b\rangle - |x'_{\rm m}\rangle)].\end{aligned}$$

(6) The probability of measuring 0 on the first qubit from the top is

$$\mathcal{P}'_R(0) = \left\| \frac{1}{2\sqrt{\beta}}(|b\rangle + |x'_{\rm m}\rangle) \right\|^2 = \frac{1}{2}\left(1 + \frac{2\,{\rm Re}(\langle b\,|x'_{\rm m}\rangle)}{1 + \|\,|x'_{\rm m}\rangle\,\|^2}\right).$$

Similarly, the introduction of $S^\dagger$ gate in the circuit in Fig. 4(b) helps us find

$$\mathcal{P}'_I(0) = \left\| \frac{1}{2\sqrt{\beta}}(|b\rangle - i\,|x'_{\rm m}\rangle) \right\|^2 = \frac{1}{2}\left(1 + \frac{2\,{\rm Im}(\langle b\,|x'_{\rm m}\rangle)}{1 + \|\,|x'_{\rm m}\rangle\,\|^2}\right).$$

Through the last two expressions, we can find that

$$\langle b|x'_{\rm m}\rangle = [(2\mathcal{P}'_R(0) - 1) + i(2\mathcal{P}'_I(0) - 1)]\beta. \tag{A2}$$

APPENDIX B: PSI-HHL FOR EXPECTATION VALUE CALCULATION: DETAILS

1. Extraction of wrong signal

We discuss below the protocol to extract the wrong signal as shown in Fig. 5(a).

(1) We begin with $|0\rangle \otimes |0\rangle \otimes |0^{n_r}\rangle \otimes |b\rangle$, and upon applying $H \otimes {\rm HHL}_1$, we get $\frac{1}{\sqrt{2}\|\,|x_{\rm w}\rangle\,\|}(|0\rangle + |1\rangle) \otimes |0\rangle \otimes |0^{n_r}\rangle \otimes |x_{\rm w}\rangle$, where $1/\|\,|x_{\rm w}\rangle\,\|$ is the normalization factor after measurement in ${\rm HHL}_1$.

(2) This is followed by the operation $|0\rangle\langle 0| \otimes I^{\otimes(1+n_r+n_b)} + |1\rangle\langle 1| \otimes I^{\otimes(1+n_r)} \otimes \mathcal{U}$, which results in

$$\frac{1}{\sqrt{2}\|\,|x_{\rm w}\rangle\,\|}[|0\rangle \otimes |0\rangle \otimes |0^{n_r}\rangle \otimes |x_{\rm w}\rangle + |1\rangle \otimes |0\rangle \otimes |0^{n_r}\rangle \otimes (\mathcal{U}\,|x_{\rm w}\rangle)].$$

(3) Acting the resulting state upon by $H \otimes I^{\otimes(1+n_r+n_b)}$, we obtain

$$\frac{1}{2\|\,|x_{\rm w}\rangle\,\|}[|0\rangle \otimes |0\rangle \otimes |0^{n_r}\rangle \otimes (|x_{\rm w}\rangle + \mathcal{U}\,|x_{\rm w}\rangle) + |1\rangle \otimes |0\rangle \otimes |0^{n_r}\rangle \otimes (|x_{\rm w}\rangle - \mathcal{U}\,|x_{\rm w}\rangle)].$$

(4) The probability of measuring 0 on the first qubit from the top is

$$\mathcal{P}_R(0) = \left\| \frac{1}{2\|\,|x_{\rm w}\rangle\,\|}(|x_{\rm w}\rangle + \mathcal{U}\,|x_{\rm w}\rangle) \right\|^2 = \frac{1}{2}\left(1 + \frac{{\rm Re}(\langle x_{\rm w}|\,\mathcal{U}\,|x_{\rm w}\rangle)}{\|\,|x_{\rm w}\rangle\,\|^2}\right).$$

Similarly, the introduction of $S^\dagger$ gate in the circuit in Fig. 5(a) helps us find

$$\mathcal{P}_I(0) = \left\| \frac{1}{2\|\,|x_{\rm w}\rangle\,\|}(|x_{\rm w}\rangle - i\mathcal{U}\,|x_{\rm w}\rangle) \right\|^2 = \frac{1}{2}\left(1 + \frac{{\rm Im}(\langle x_{\rm w}|\,\mathcal{U}\,|x_{\rm w}\rangle)}{\|\,|x_{\rm w}\rangle\,\|^2}\right).$$

Through the last two expressions, we can find that

$$\langle x_{\rm w}|\mathcal{U}|x_{\rm w}\rangle = [(2\mathcal{P}_R(0) - 1) + i(2\mathcal{P}_I(0) - 1)]\||x_{\rm w}\rangle\|^2.$$

2. Extraction of mixed signal

We discuss below the protocol for extracting the mixed signal as shown in Fig. 5(b). We note that the mixed signal has in it a cross term.

(1) We begin with $|0\rangle \otimes |0\rangle \otimes |0^{n_r}\rangle \otimes |b\rangle$, and upon applying $H \otimes \mathrm{HHL}_2$, we get $\frac{1}{\sqrt{2}\| |x'_{\mathrm{m}}\rangle \|}(|0\rangle + |1\rangle) \otimes |1\rangle \otimes |0^{n_r}\rangle \otimes |x'_{\mathrm{m}}\rangle$, where $1/\| |x'_{\mathrm{m}}\rangle \|$ is the normalization factor after measurement in HHL_2.

(2) This is followed by the operation $|0\rangle\langle 0| \otimes I^{\otimes(1+n_r+n_b)} + |1\rangle\langle 1| \otimes I^{\otimes(1+n_r)} \otimes \mathcal{U}$, which results in

$$\frac{1}{\sqrt{2}\| |x'_{\mathrm{m}}\rangle \|}(|0\rangle \otimes |1\rangle \otimes |0^{n_r}\rangle \otimes |x'_{\mathrm{m}}\rangle + |1\rangle \otimes |1\rangle \otimes |0^{n_r}\rangle \otimes [\mathcal{U}\,|x'_{\mathrm{m}}\rangle]).$$

(3) Acting the resulting state upon by $H \otimes I^{\otimes(1+n_r+n_b)}$, we obtain

$$\frac{1}{2\| |x'_{\mathrm{m}}\rangle \|}[|0\rangle \otimes |1\rangle \otimes |0^{n_r}\rangle \otimes (|x'_{\mathrm{m}}\rangle + \mathcal{U}\,|x'_{\mathrm{m}}\rangle) + |1\rangle \otimes |1\rangle \otimes |0^{n_r}\rangle \otimes (|x'_{\mathrm{m}}\rangle - \mathcal{U}\,|x'_{\mathrm{m}}\rangle)].$$

(4) The probability of measuring 0 on the first qubit from the top is

$$\begin{aligned}\mathcal{P}'_R(0) &= \left\| \frac{1}{2\| |x'_{\mathrm{m}}\rangle \|}(|x'_{\mathrm{m}}\rangle + \mathcal{U}\,|x'_{\mathrm{m}}\rangle) \right\|^2 \\ &= \frac{1}{2}\left(1 + \frac{\mathrm{Re}(\langle x'_{\mathrm{m}}|\,\mathcal{U}\,|x'_{\mathrm{m}}\rangle)}{\| |x'_{\mathrm{m}}\rangle \|^2}\right).\end{aligned}$$

Similarly, the introduction of $S^\dagger$ gate in the circuit in Fig. 5(a) helps us find

$$\begin{aligned}\mathcal{P}'_I(0) &= \left\| \frac{1}{2\| |x'_{\mathrm{m}}\rangle \|}(|x'_{\mathrm{m}}\rangle - i\mathcal{U}\,|x'_{\mathrm{m}}\rangle) \right\|^2 \\ &= \frac{1}{2}\left(1 + \frac{\mathrm{Im}(\langle x'_{\mathrm{m}}|\,\mathcal{U}\,|x'_{\mathrm{m}}\rangle)}{\| |x'_{\mathrm{m}}\rangle \|^2}\right).\end{aligned}$$

$$\langle x'_{\mathrm{m}}|\,\mathcal{U}\,|x'_{\mathrm{m}}\rangle = \{[2\mathcal{P}'_R(0) - 1] + i[2\mathcal{P}'_I(0) - 1]\}\| |x'_{\mathrm{m}}\rangle \|^2.$$

3. Extracting the cross term

We present below our protocol for the circuit given in Fig. 5(c), using which we obtain the cross term.

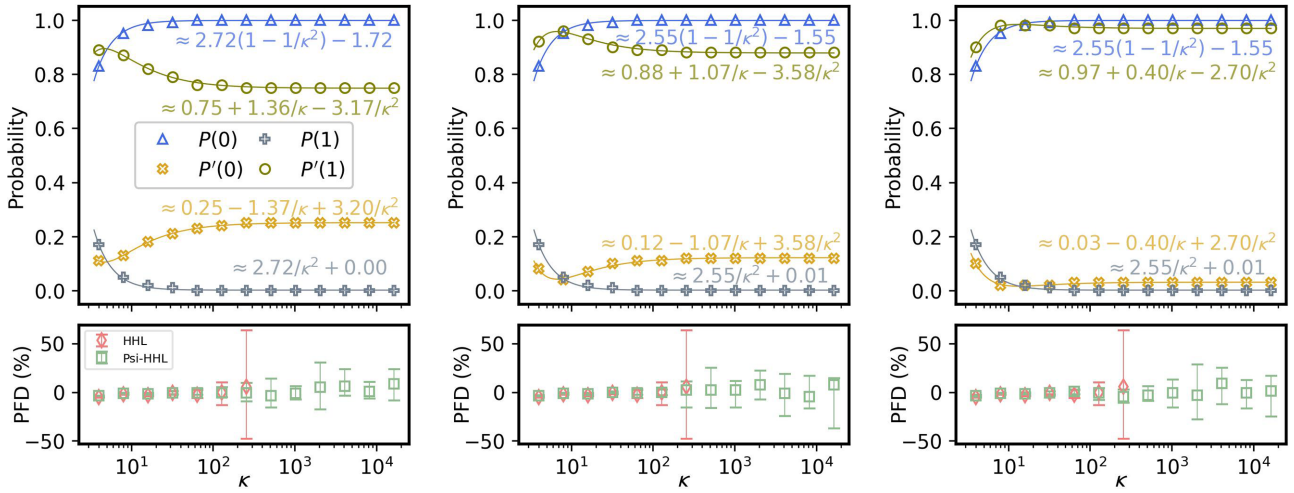
(1) We begin with $|0\rangle \otimes |0\rangle \otimes |0^{n_r}\rangle \otimes |b\rangle$, and upon applying $H \otimes \mathrm{HHL}$ (without postselection), we get $\frac{1}{\sqrt{2}}(|0\rangle + |1\rangle) \otimes (\sum_i b_i \sqrt{1 - \frac{C^2}{\lambda_i^2}}\,|0\rangle + \frac{C}{\lambda_i}\,|1\rangle) \otimes |0^{n_r}\rangle \otimes |v_i\rangle$.

(2) This is followed by the operation $[|0\rangle\langle 0| \otimes I + |1\rangle\langle 1| \otimes R_Y(2\alpha)] \otimes I^{\otimes(n_r+n_b)}$, which results in

$$\begin{aligned}&\frac{1}{\sqrt{2}}|0\rangle \otimes \left(\sum_i b_i \sqrt{1 - \frac{C^2}{\lambda_i^2}}\,|0\rangle + b_i \frac{C}{\lambda_i}\,|1\rangle\right) \otimes |0^{n_r}\rangle\,|v_i\rangle + \frac{1}{\sqrt{2}}|1\rangle \otimes \left[\left(\sum_i b_i \sqrt{1 - \frac{C^2}{\lambda_i^2}}\cos(\alpha) - b_i \frac{C}{\lambda_i}\sin(\alpha)\right)|0\rangle\right. \\ &\left. + \left(\sum_i b_i \sqrt{1 - \frac{C^2}{\lambda_i^2}}\sin(\alpha) + b_i \frac{C}{\lambda_i}\cos(\alpha)\right)|1\rangle\right] \otimes |0^{n_r}\rangle \otimes |v_i\rangle\,.\end{aligned}$$

(3) Then, we apply the operation $(|0\rangle\langle 0| \otimes X + |1\rangle\langle 1| \otimes I) \otimes I^{\otimes(n_r+n_b)}$ on the first and second qubits from the top and get

$$\begin{aligned}&\frac{1}{\sqrt{2}}|0\rangle \otimes \left(\sum_i b_i \sqrt{1 - \frac{C^2}{\lambda_i^2}}\,|1\rangle + b_i \frac{C}{\lambda_i}\,|0\rangle\right) \otimes |0^{n_r}\rangle \otimes |v_i\rangle + \frac{1}{\sqrt{2}}|1\rangle \otimes \left[\left(\sum_i b_i \sqrt{1 - \frac{C^2}{\lambda_i^2}}\cos(\alpha) - b_i \frac{C}{\lambda_i}\sin(\alpha)\right)|0\rangle\right. \\ &\left. + \left(\sum_i b_i \sqrt{1 - \frac{C^2}{\lambda_i^2}}\sin(\alpha) + b_i \frac{C}{\lambda_i}\cos(\alpha)\right)|1\rangle\right] \otimes |0^{n_r}\rangle \otimes |v_i\rangle\,.\end{aligned}$$



(a) $\alpha = 60°$ (b) $\alpha = 70°$ (c) $\alpha = 80°$

FIG. 21. Data for 32×32 matrices: sub-figure (a) presents the data for α of 60 degrees, whereas (b) and (c) show the results for α of 70 and 80 degrees respectively. Note that we have again reproduced here (a) with 1×10^6 shots (which are already present in the main text). In all of the examples, A is chosen to be a nondiagonal matrix and $\vec{b}$ is set in an unequal superposition. Each data point is an average over 10 repetitions.

(4) Measuring the second qubit from the top and postselecting the outcome 1, we get the state vector

$$\frac{1}{\sqrt{\delta}}\left(\frac{1}{\sqrt{2}}|0\rangle \otimes |1\rangle \otimes |0^{n_r}\rangle \otimes |x_{\rm w}\rangle + \frac{1}{\sqrt{2}}|1\rangle \otimes |1\rangle \otimes |0^{n_r}\rangle \otimes |x'_{\rm m}\rangle\right),$$

where $1/\sqrt{\delta}$ is the normalization factor after measurement and $\delta = \frac{1}{2}(\| |x_{\rm w}\rangle \|^2 + \| |x'_{\rm m}\rangle \|^2)$.

(5) Applying $|0\rangle\langle 0| \otimes I^{\otimes(1+n_r+n_b)} + |1\rangle\langle 1| \otimes I^{\otimes(1+n_r)} \otimes \mathcal{U}$, we obtain

$$\frac{1}{\sqrt{\delta}}\left(\frac{1}{\sqrt{2}}|0\rangle \otimes |1\rangle \otimes |0^{n_r}\rangle \otimes |x_{\rm w}\rangle + \frac{1}{\sqrt{2}}|1\rangle \otimes |1\rangle \otimes |0^{n_r}\rangle \otimes (\mathcal{U}|x'_{\rm m}\rangle)\right).$$

(6) Acting the resulting state upon by $H \otimes I^{\otimes(1+n_r+n_b)}$, we obtain

$$\frac{1}{\sqrt{\delta}}\left(\frac{1}{2}|0\rangle \otimes |1\rangle \otimes |0^{n_r}\rangle \otimes (|x_{\rm w}\rangle + \mathcal{U}|x'_{\rm m}\rangle) + \frac{1}{2}|1\rangle \otimes |1\rangle \otimes |0^{n_r}\rangle \otimes (|x_{\rm w}\rangle - \mathcal{U}|x'_{\rm m}\rangle)\right).$$

(7) The probability of measuring 0 on the first qubit from the top is

$$\begin{aligned}\bar{P}(0) &= \left\| \frac{1}{2\sqrt{\delta}}(|x_{\rm w}\rangle + \mathcal{U}|x'_{\rm m}\rangle)\right\|^2 \\ &= \frac{1}{2}\left(1 + \frac{2\,{\rm Re}(\langle x_{\rm w}|\mathcal{U}|x'_{\rm m}\rangle)}{\| |x_{\rm w}\rangle \|^2 + \| |x'_{\rm m}\rangle \|^2}\right).\end{aligned}$$

Through the last equation and the expression of $\langle x_{\rm w}|\mathcal{U}|x_{\rm w}\rangle$ computed earlier, we can find that

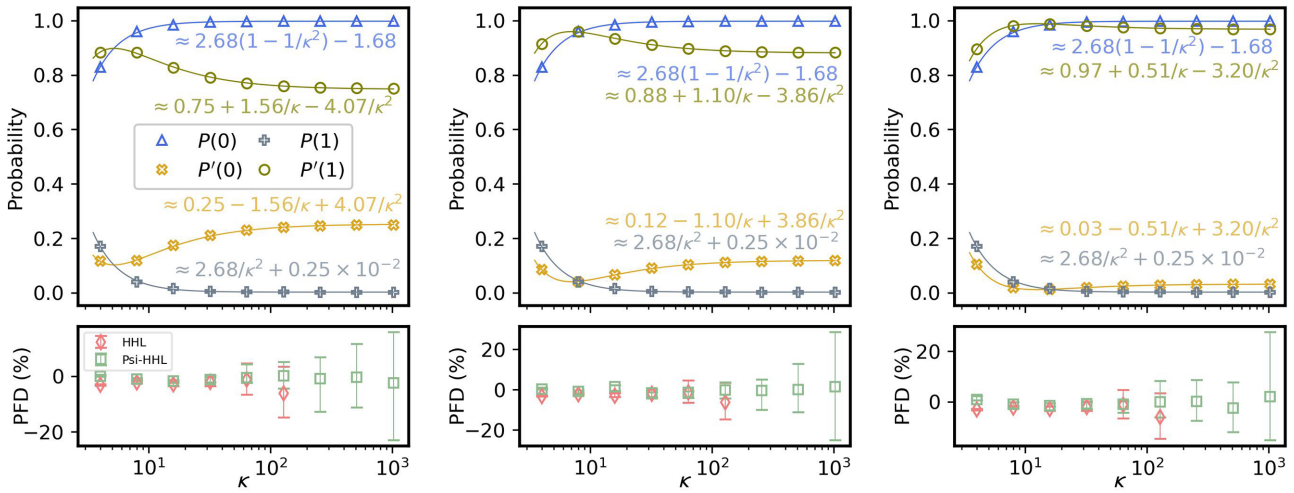
$${\rm Re}(\langle x_{\rm w}|\mathcal{U}|x_{\rm r}\rangle) = \frac{\delta}{\cos(\alpha)}[2\bar{P}(0) - 1] - \frac{\sin(\alpha)}{\cos(\alpha)}[2\mathcal{P}_R(0) - 1]\| |x_{\rm w}\rangle \|^2.$$

APPENDIX C: DETAILS ON CALCULATIONS INVOLVING TOY MATRICES FROM SIZE 4 × 4 THROUGH 64 × 64

In our Results section in the main text, we discussed the case of A not diagonal and the amplitude encoded state corresponding to $\vec{b}$ in an unequal superposition. We also provide our 4×4 through 64×64 matrices that we considered in the main text in Fig. 14.

We now provide additional data on two more choices for our 4×4 A matrices:

(1) A is diagonal and the amplitude encoded state corresponding to $\vec{b}$ is in an equal superposition. In particular,



(a) $\alpha = 60°$ (b) $\alpha = 70°$ (c) $\alpha = 80°$

FIG. 22. Data for 64×64 matrices: sub-figure (a) presents the data for α of 60 degrees, whereas (b) and (c) show the results for α of 70 and 80 degrees respectively. Note that we have again reproduced here (a) with 1×10^6 shots (which are already present in the main text). In all of the examples, A is chosen to be a nondiagonal matrix and $\vec{b}$ is set in an unequal superposition. Each data point is an average over 10 repetitions.

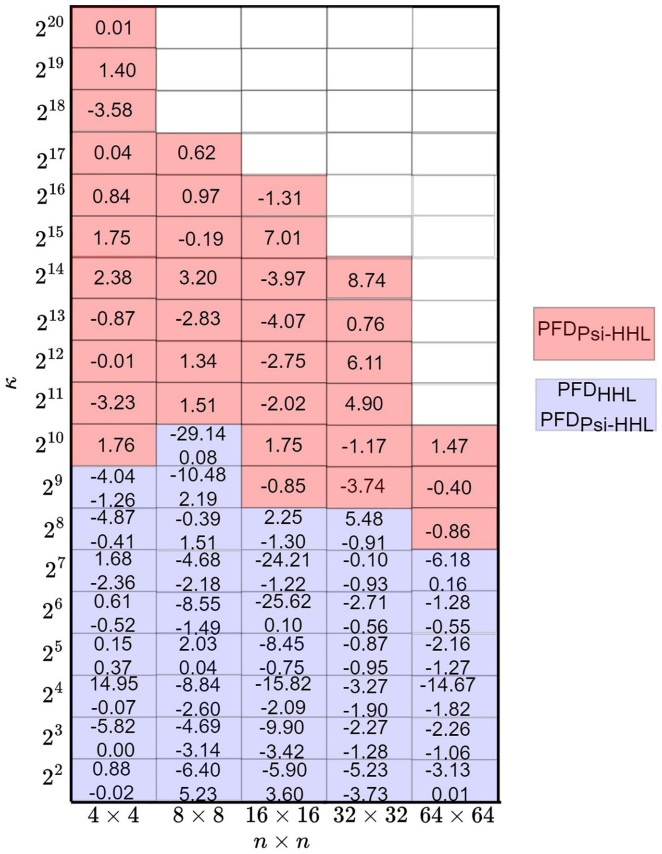


FIG. 23. Figure showing average (over 10 repetitions) values of percentage fraction difference (PFD) obtained from HHL and Psi-HHL, as the condition number κ grows from 2^2 to 2^{20}, for fixed A matrix sizes going from 4×4 to 64×64. Only the case where $\alpha = 60°$, A not diagonal, $\vec{b}$ in an unequal superposition, and number of shots $= 10^6$ is considered. The blue cells indicate cases where HHL gives outputs, and red denotes cases where HHL fails. The white cells denote those cases for which we did not carry out a calculation, due to computational cost.

$A = \begin{pmatrix} 2^{-(n_r-1)} & 0.00 & 0.00 & 0.00 \\ 0.00 & 0.75 & 0.00 & 0.00 \\ 0.00 & 0.00 & 0.50 & 0.00 \\ 0.00 & 0.00 & 0.00 & 1.00 \end{pmatrix}$, and the unnormalized $\vec{b} = \begin{pmatrix} 1.00 \\ 1.00 \\ 1.00 \\ 1.00 \end{pmatrix}$. The sparsity s of A is 1.

(2) A is diagonal and the amplitude encoded state associated with $\vec{b}$ is in an unequal superposition. In particular, A is the same as in case 1 given above, and $\vec{b} = \begin{pmatrix} 0.10 \\ 0.01 \\ 0.20 \\ 1.00 \end{pmatrix}$.

We also present these results for α set to $60°$, $70°$, and$80°$ (the main text only discusses the first case). Furthermore, while the main text considers 1×10^6 shots, we also perform the same analyses for 10^5 shots. All of these results are presented in Figs. 17 and 18 for the cases considering 10^5 and 10^6 shots, respectively. The accompanying data are provided in Tables IV–VI, for $60°$, $70°$, and$80°$ examples, respectively.

APPENDIX D: DETAILS ON CALCULATIONS INVOLVING QUANTUM CHEMISTRY MATRICES

1. A matrix and $\vec{b}$ generation

We begin by explaining the procedure for generating an A matrix of size $n \times n$. We use the configuration state function-based graphical unitary group approach–configuration interaction singles and oubles (GUGA-CISD) method available in the GAMESS program [26] to construct the Hamiltonian for a given molecule in a specified single particle basis. GUGA-CI ensures that the Hamiltonian is constructed in an orthogonal basis; hence, it is Hermitian. Also, because it is a spin-adapted

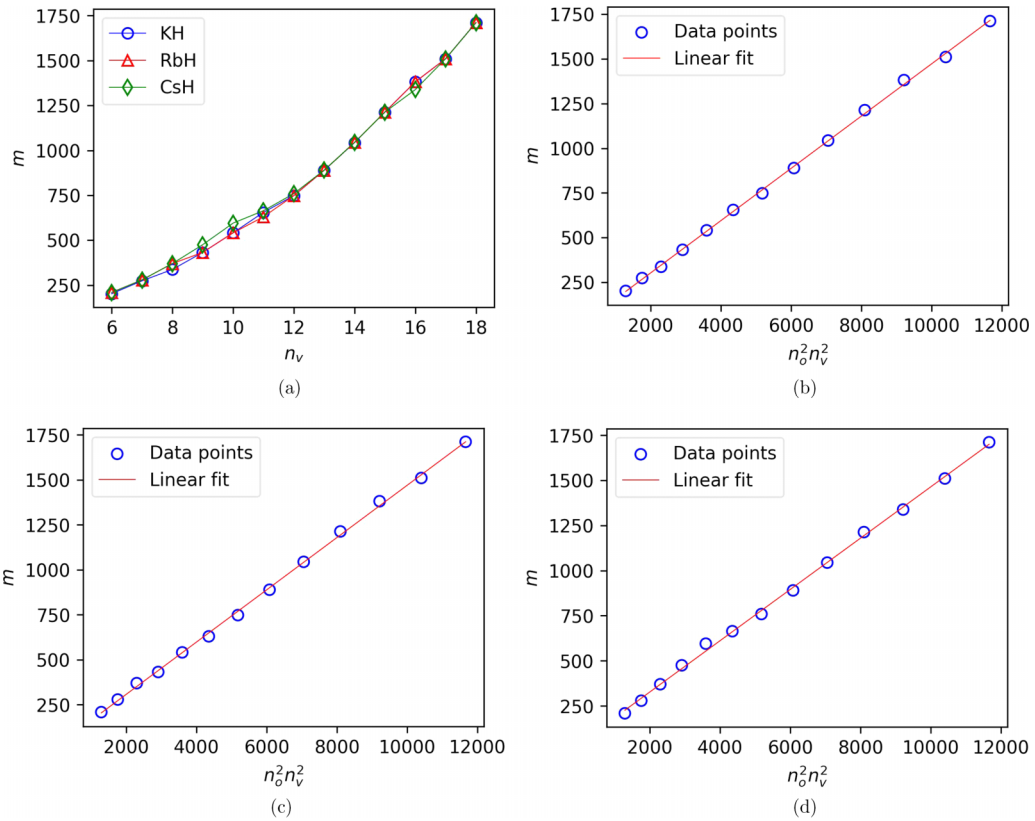


FIG. 24. (a) Shows the increase in system size (m) with the number of virtuals n_v for KH, RbH, and CsH molecules in the LCCSD approximation, while (b)–(d) show that m increases as $n_o^2 n_v^2$ for the three molecules, as one would expect.

CI method, it avoids spin contamination of the wave function, thereby giving accurate results. In order to generate the A matrix, we remove the first row and the first column of the GUGA-CISD Hamiltonian matrix and subtract the diagonal entries of the resulting matrix with the energy obtained from Møller-Plesset theory to second order in perturbation (also called MP2 in literature). The latter step is carried out for the purpose of normal ordering, which in turn ensures that HHL would output the correlation part of the ground-state energy directly instead of the total ground-state energy (which can be written as a sum of the HF energy and the correlation energy, with the latter being much smaller than the former). This is desirable when one executes HHL-LCC calculations on NISQ/late-NISQ era quantum hardware, as the error in the total ground-state energy can be much greater than the correlation energy itself. We also note that unlike the traditional approach where the HF energy is subtracted from the diagonal entries, we take away the MP2 energy, in order to make sure that A is positive definite. In a sense, subtracting MP2 energy could be thought of as a level shift over and beyond subtracting the HF energy.

We now focus our attention on the elements of the A matrix. The size of an A matrix, $m \times m$, generated from a quantum-chemical calculation, which we can denote as A_{mol}, is not necessarily of the dimension $n \times n$. In such cases, we embed the A_{mol} matrix of dimension $m \times m$ as a diagonal block in a larger matrix of dimension $n \times n$, with the other diagonal block being an identity matrix of size $(n-m) \times (n-m)$, denoted as $\mathcal{I}$. In such a case, we solve a system of linear equations given by

$$\begin{pmatrix} A_{\text{mol}} & 0 \\ 0 & \mathcal{I} \end{pmatrix} \begin{pmatrix} \vec{x} \\ \vec{0} \end{pmatrix} = \begin{pmatrix} \vec{b} \\ \vec{0} \end{pmatrix}. \tag{D1}$$

This approach ensures that the eigenvalues of A_{mol} remain unaffected, as long as its maximum eigenvalue of the scaled matrix is ≈ 1. We choose our matrices carefully so that this condition is satisfied. In the event that the maximum diagonal entry of A is less than 1, it is recommended to pad with the largest (or the smallest) diagonal entry of A so that the number of shots expended is reduced. As an example, we picked a 3×3 sparse matrix such that the largest diagonal entry is 0.70: $\begin{pmatrix} 0.25 & 0.10 & 0.00 \\ 0.10 & 0.45 & 0.20 \\ 0.00 & 0.20 & 0.70 \end{pmatrix}$, and considered two cases: padding with 1 and with 0.70. We found that the condition number κ is larger in the latter (5.16) than in the former (4.21).

Since for the problems we consider, κ increases with system size monotonically, and further, going from an unpadded to a padded matrix always right shifts a data point, it is sufficient to carry out κ versus m analysis for the unpadded case, as it upper bounds the complexity of the padded scenario of κ versus n.

2. Orbital character analysis

We now explain the procedure that we adopted for selecting orbitals, based on orbital character. We begin with RbH,

and then proceed to explain our procedure for CsH (with accompanying data provided in Table XII).

We fix the number of occupied orbitals to 6, 8, and 10. We now describe the method adopted in choosing virtual molecular orbitals (MOs). Instead of taking the approach of ordering the virtual MOs by energy in ascending order and then imposing an energy cutoff to define our active space, we pick those MOs that are dominated by important atomic orbitals (AOs). We select the important AOs, and for the purposes of this work, we pick those AOs in the order of the principal quantum numbers. For example, in the case of RbH, we can decide the important AOs from the set that arises from our choice of basis, namely, the Sapporo double-zeta basis: $5s$ through $7p$. For the purposes of our analysis on condition number versus system size, we pick all the AOs that the basis allows in order to obtain more data points for fitting (details given in Table XII). We now move to some specifics for RbH: for the smallest system size considered (1 virtual MO), we pick the first virtual from our sorted MO list, which is the MO dominated by the Rb $5s$-$5p_z$ hybrid, and thus our active space that is built out of 6 occupied MOs and 1 virtual one has a system size $m \times m$ of 209×209, and subsequently upon padding, an A matrix size $n \times n$ of 256×256. For the next system size, we add the next MO in the sorted list, which is dominated by Rb $5s$, leading to a 279×279 matrix, which, after padding, becomes a matrix of size 512×512. We continue to construct A matrices in this fashion until we reach $m = 2296$, for which κ is about 211.94.

We do the same for KH and CsH molecules: we fix the number of occupied orbitals to 6, 8, and 10 occupied oritals while progressively increasing the number of valence orbitals. The order in which we add virtual MOs as well as each such virtual MO's details are mentioned in Table XII.

[1] A. W. Harrow, A. Hassidim, and S. Lloyd, Quantum algorithm for linear systems of equations, Phys. Rev. Lett. **103**, 150502 (2009).

[2] N. Baskaran, A. S. Rawat, A. Jayashankar, D. Chakravarti, K. Sugisaki, S. Roy, S. B. Mandal, D. Mukherjee, and V. S. Prasannaa, Adapting the Harrow-Hassidim-Lloyd algorithm to quantum many-body theory, Phys. Rev. Res. **5**, 043113 (2023).

[3] J. Golden, D. J. O'Malley, and V. Hari, Quantum computing and preconditioners for hydrological linear systems, Sci. Rep. **12**, 22285 (2022).

[4] G. Brassard, P. Hoyer, M. Mosca, and A. Tapp, Quantum amplitude amplification and estimation, AMS Contemporary Mathematics **305**, 74 (2002).

[5] A. Ambainis, Variable time amplitude amplification and a faster quantum algorithm for solving systems of linear equations, arXiv:1010.4458.

[6] B. D. Clader, B. C. Jacobs, and C. R. Sprouse, Preconditioned quantum linear system algorithm, Phys. Rev. Lett. **110**, 250504 (2013).

[7] C. Shao and H. Xiang, Quantum circulant preconditioner for a linear system of equations, Phys. Rev. A **98**, 062321 (2018).

[8] Y. Tong, D. An, N. Wiebe, and L. Lin, Fast inversion, preconditioned quantum linear system solvers, fast Green's-function computation, and fast evaluation of matrix functions, Phys. Rev. A **104**, 032422 (2021).

[9] D. V. Babukhin, Harrow-Hassidim-Lloyd algorithm without ancilla postselection, Phys. Rev. A **107**, 042408 (2023).

[10] D. Orsucci and V. Dunjko, On solving classes of positive-definite quantum linear systems with quadratically improved runtime in the condition number, Quantum **5**, 573 (2021).

[11] A. M. Childs, R. Kothari, and R. D. Somma, Quantum algorithm for systems of linear equations with exponentially improved dependence on precision, SIAM J. Comput. **46**, 1920 (2017).

[12] P. C. S. Costa, D. An, Y. R. Sanders, Y. Su, R. Babbush, and D. W. Berry, Optimal scaling quantum linear-systems solver via discrete adiabatic theorem, PRX Quantum **3**, 040303 (2022).

[13] J. R. Shewchuk, An introduction to the conjugate gradient method without the agonizing pain, Technical report, School of Computer Science Carnegie Mellon University, Pittsburgh (1994), https://dl.acm.org/doi/10.5555/865018.

[14] D. Dervovic, M. Herbster, P. Mountney, S. Severini, N. Usher, and L. Wossnig, Quantum linear systems algorithms: a primer, arXiv:1802.08227.

[15] H. J. Morrell, A. Zaman, and H. Y. Wong, A step-by-step HHL algorithm walkthrough to enhance understanding of critical quantum computing concepts, IEEE Access **11**, 77117 (2023).

[16] X. Liu, H. Xie, Z. Liu, and C. Zhao, Survey on the improvement and application of HHL algorithm, J. Phys.: Conf. Ser. **2333**, 012023 (2022).

[17] B. Duan, J. Yuana, C.-H. Yub, J. Huanga, and C.-Y. Hsie, A survey on HHL algorithm: From theory to application in quantum machine learning, Phys. Lett. A **384**, 126595 (2020).

[18] J. C. Garcia-Escartin and P. Chamorro-Posada, SWAP test and Hong-Ou-Mandel effect are equivalent, Phys. Rev. A **87**, 052330 (2013).

[19] L. Lin, Lecture notes on quantum algorithms for scientific computation, arXiv:2201.08309.

[20] M. Treinish *et al.*, Qiskit: An open-source framework for quantum computing, GitHub, IBM QISKIT repository (2022), https://github.com/Qiskit/qiskit.

[21] K. Bourzac, Chemistry is quantum computing's killer app, C&EN **95**, 27 (2017).

[22] N. Geum, G.-H. Jeung, A. Derevianko, R. Cõté, and A. Dalgarno, Interaction potentials of LiH, NaH, KH, RbH, and CsH, J. Chem. Phys. **115**, 5984 (2001).

[23] R. A. Brooks, C. H. Anderson, and N. F. Ramsey, Rotational magnetic moments of diatomic alkalis, Phys. Rev. Lett. **10**, 441 (1963).

[24] T. Noro, M. Sekiya, and T. Koga, Segmented contracted basis sets for atoms H through Xe: Sapporo-(DK)-nZP sets (n = D, T, Q), Theor. Chem. Acc. **131**, 1124 (2012).

[25] B. P. Pritchard, D. Altarawy, B. Didier, T. D. Gibson, and T. L. Windus, A new basis set exchange: An open, up-to-date resource for the molecular sciences community, J. Chem. Inf. Model. **59**, 4814 (2019).

[26] G. M. J. Barca *et al.*, Recent developments in the general atomic and molecular electronic structure system, J. Chem. Phys. **152**, 154102 (2020).